3D Printing-Assisted Nanoparticle Assembly for Multifunctional Applications

by

Sayli Jambhulkar

A Dissertation Presented in Partial Fulfillment
of the Requirements for the Degree
Doctor of Philosophy

Approved February 2023 by the
Graduate Supervisory Committee:

Kenan Song, Chair
Arunachala Mada Kannan
Heather Emady

ARIZONA STATE UNIVERSITY

May 2023

ABSTRACT

Nanoparticle (NP) assembly is critical where NPs are organized into complex superstructures through direct and indirect interactions. Long-range NP orders have nanoscale locational selectivity, orientational alignment, and scalable micropatterning, which are indispensable for enabling multiple functionalities and improving the performances of different systems. Though nanoparticles can self-assemble into organized nanostructures via simple drying thermodynamics, scalability has been a primary issue. Thus, this research focuses on more scalable manufacturing for directed NP assembly. First, 3D printing was used for template fabrications with varying topology features. Next, nanoparticle engineering with colloidal and surface studies leads to desirable NP packing on template surfaces. Finally, the processed devices will also demonstrate a few applications of surface micropatterning with nanoscale particle orders. Specifically, a few manufacturing procedures involve (i) stereolithography (SLA)/layer-by-layer dip coating, (ii) continuous liquid interface projection (μCLIP)/ink writing, (iii) fused deposition melting (FDM)/direct ink writing, and (iv) multiphase direct ink writing (MDIW)/wet etching. To demonstrate the applicability of hybrid manufacturing, a broad range of nanoparticles, including carbon nanofibers (CNFs), MXene nanoflakes, and boron nitride nanoplatelets (BNNPs) were studied in this research. With well-managed template physics and NP dispersion control, nanoparticle orientational alignment and positional preferences are driven by short- and long-range intermolecular interactions (e.g., convective, van der Waals, capillarity, shear, and other secondary bonding). The printed devices displayed multifunctional properties, *i.e.*, anisotropic conductivity, piezoresistive and chemical sensitivity, mechanical durability, and heat dissipation capabilities, for microelectronic applications. This fabrication technique shows enormous potential for rapid, scalable, and low-cost manufacturing of hierarchical structures, especially for micropatterning of nanoparticles not easily accessible through conventional processing methods.

DEDICATION

I want to dedicate this thesis to all my family members – my parent Dr. Chhaya Jambhulkar, Dr. Siddharth Jambhulkar, my brother Sahil Jambhulkar, and my parent-in-laws Mrs. Mamata Biswal and Lect. Chandan Kumar Beura, for support throughout my academic career. Last but not least, my husband Vikrant Beura for his unwavering support, guidance, encouragement, and constant belief in me throughout the Ph.D. journey

ACKNOWLEDGMENTS

I would like to express my sincere gratitude to my Ph.D. supervisor, Dr. Kenan Song, for his continuous guidance, motivation, and for providing me with numerous opportunities throughout this research work. Dr. Song's insightful comments and constructive feedback were invaluable in shaping my research project and improving my research skills. His unwavering support, encouragement, and patience were instrumental in helping me overcome the challenges I encountered during the course of this work. I am deeply grateful for his mentorship and the opportunities he provided me to grow as a researcher. I am also grateful to my Ph.D. dissertation committee members Dr. Arunachala Mada Kannan and Dr. Heather Emady for their valuable time, discussions, and feedback. Furthermore, I want to acknowledge the collaborating research groups, such as laboratories of Fuel Cell Research (*PI Dr. Arunachala Mada Kannan*), Advanced Manufacturing Functional Devices (*PI Dr. Xiangfan Chen*), 3DX Research (*PI Dr. Dhruv Bhate*), and Multiscale Manufacturing Materials Processing (*PI Dr. Qiong (Eric) Nian*), at Arizona State University. Further, my sincere thanks to the alumni and current lab members of the Advanced Materials and Advanced Manufacturing Laboratory group for their help and support during my research work so far. I would like to extend my sincere thanks to the alumni and current lab members of the Advanced Materials and Advanced Manufacturing Laboratory group for their help and support during my research work so far. Their contributions were instrumental in shaping my research project and improving my research skills. Their constructive feedback, insightful discussions, and technical expertise were invaluable in solving the challenges I encountered during the course of this work. Lastly, I want to thank my husband, Vikrant Beura along with my family members, for their constant support and motivation during the Ph.D. journey.

TABLE OF CONTENTS

Page

LIST OF TABLES xi

LIST OF FIGURES xii

CHAPTER

1 INTRODUCTION 1

- 1.1 Research Objective 5

2 SCALABLE ALIGNMENT AND SELECTIVE DEPOSITION OF NANOPARTICLES FOR MULTIFUNCTIONAL SENSOR APPLICATIONS 7

- Abstract 7
- 2.1 Introduction 7
- 2.2 Experimentation and Characterization 10
  - 2.2.1 Carbon Nanofiber Dispersion Preparation 10
  - 2.2.2 SLA 3D Printing 11
  - 2.2.3 Anisotropic Alignment of Carbon Nanofibers 11
  - 2.2.4 Electrical/Sensing Measurements of Epoxy/CNF Electrodes 12
- 2.3 Results and Discussion 14
  - 2.3.1 SLA 3D Printing 14
  - 2.3.2 Anisotropic Assembly of CNFs 14
  - 2.3.3 Electronic Properties 16
  - 2.3.4 Piezoresistive Properties 19

2.3.5 Volatile Organic Compounds (VOC) Sensing of Patterned Substrate with Horizontal Dipping 21

2.4 Conclusion 23

REFERENCES 25

3 ALIGNED $TI_3C_2T_X$ MXENE FOR 3D MICROPATTERNING VIA ADDITIVE MANUFACTURING 27

Abstract 27

3.1 Introduction 28

3.2 Experimentation and Characterization 31

3.2.1 MXene Synthesis and Dispersion Preparation 31

3.2.2 Micro-continuous Liquid Interface Projection 3D Printing 32

3.2.3 Layer-by-Layer MXene Assembly via Direct Ink Writing of Low-Viscosity Colloids 33

3.2.4 Rheology Measurements 33

3.2.5 Material Characterizations 34

3.3 Results and Discussion 34

3.3.1 MXene Synthesis and Characteristics Properties 34

3.3.2 µCLIP for 3D Printed Surface Patterns 36

3.3.3 Theoretical Framework for the Capillary-Driven 2D MXene Assembly 39

3.3.4 Rheological Characterization of MXene Printing Inks 41

3.3.5 Structural and Morphological Characteristics of Printed MXene Multilayers ... 46

3.3.6 Electrical, Sensing, and Piezoresistive Properties ... 50

3.4 Conclusion ... 58

REFERENCES ... 60

4 A HYBRID 3D PRINTING FOR HIGHLY-EFFICIENT NANOPARTICLE MICROPATTERNING ... 62

Abstract ... 62

4.1 Introduction ... 62

4.2 Experimental Section ... 66

4.2.1 Materials ... 66

4.2.2 FDM 3D Printing ... 66

4.2.3 MXene Nanoparticle Deposition ... 67

4.2.4 Characterization ... 67

4.3 Results and Discussion ... 68

4.3.1 3D printing surface templates for directed nanoparticle assembly ... 68

4.3.2 MXene synthesis with tunable particle dimensions and physics ... 73

4.3.3 Directed 2D MXene Assembly ... 76

4.4 Conclusion ... 81

REFERENCES ... 83

5 A MULTI-MATERIAL 3D PRINTING-ASSISTED MICROPATTERNING ... 85

Abstract 85

5.1 Introduction 86

5.2 Experimentation and Material Characterization 89

5.2.1 Materials 89

5.2.2 3D Printing Ink Preparations 90

5.2.3 MDIW 3D Printing 91

5.2.4 Wet Etching 92

5.2.5 Material Characterizations 92

5.3 Results and Discussion 94

5.3.1 Overview of the Micropatterning Mechanism. 94

5.3.2 Ink Rheology and 3D Printing Processibility 98

5.3.3 Multiphase Sublayer Formability 102

5.3.4 Etching Kinetics for Surface Micropatterning 105

5.3.5 Thermal Dissipation Demonstration 110

5.4 Conclusion 114

REFERENCES 116

SUMMARY AND FUTURE OUTLOOK 120

REFERENCES 123

APPENDIX

SUPPORTING INFORMATION FOR CHAPTER 2 136

SUPPORTING INFORMATION FOR CHAPTER 3 138

APPENDIX Page

SUPPORTING INFORMATION FOR CHAPTER 4 140

SUPPORTING INFORMATION FOR CHAPTER 5 144

STATEMENT OF COAUTHORS' PERMISSIONS 148

LIST OF TABLES

Table Page

Table 1. Nomenclature of Assembled Samples 12

Table 2. MXene Film Thickness for Different Concentrations (10, 20, and 50 mg/ml) and Layer Number <n>... 50

Table 3. Ink compositions and Sample Nomenclature. 90

Table 4. The Approximate Values of Capillary Force (F_c) and Reynold's Number (Re) of MXene Ink Within Microchannels of Different LH 145

LIST OF FIGURES

Figure Page

Figure 1. (a) As Received CNFs from Sigma-Aldrich (Scale Bar 2 µm), (b) the CNF Dispersion with Different Organic Solvents (e.g., DMSO, THF, DMF, and DMA) with 1 mg of CNF in 10 ml Solvent Prepared by 24 hr of Ultrasonication. 11

Figure 2. The Self-assembled Setup Used to Perform Organic Chemical Vapor Sensing Measurements. 14

Figure 3. (a) Schematic Diagram of the Fabrication Process Combining the Stereolithography (SLA)-based Patterning and Coating-based Assembly Technology for Aligned Nanoparticle Composites. (a_1) 3D Printed Substrate Surfaces. (a_2) Schematic of the Aligning Mechanism During Dip Coating with Front and Side Views. SEM Images of (b) Flat Substrate after Dip-coating, (c) Surface Patterned Substrate with Vertical Dipping, and (c) Patterned Substrate with Horizontal Dipping (Inserted Images in Are the Magnified SEM Images). 16

Figure 4. (a) The Anisotropic Electrical Conductivity of Epoxy/CNF Composite with Light Bulb Demonstration, (b) Resistance Values of Samples along with the Longitudinal and Transverse Directions as Compared to Samples with Random CNF Distributions. (c) Optical Micrograph of the Dip-coated Substrate in the Dispersion of Different Concentrations (i.e., 1, .5, 1.0, and 10 mg/ml), (d) Change in Electric Resistance after Scratching CNF Patterned Surface with Different Materials. 18

Figure 5. SEM Micrographs Show Morphologies of CNF Bands Assembled on 3D Printed Substrates by Horizontal Dipping of Different Concentrations (a_1, a_2) E/CNF$_{0.1\text{-h}}$, (b_1, b_2) E/ CNF$_{0.5\text{-h}}$ and, (c_1, c_2) CNF$_{10.0\text{-h.}}$ 19

Figure Page

Figure 6. (a) Relative Changes in Resistance Versus Strain from 0 to 10%, (b) Relative Change in Resistance for Loading-unloading Cycles of Different Strains, and (c) Relative Change in Resistance for Multiple Cycles at 3.0% Strain. 20

Figure 7. Changes in Resistance of Chemical Sensors Demonstrated the High Sensitivity Due to Exposure to Volatile Organic Chemicals (VOCs) of Low Concentrations for (a) Methanol, (b) Ethanol, (d) Acetone, and (e) Dichloromethane (DCM). (c) Different Responses of Random and Horizontal Nanoparticles to Ethanol at 25 ppm. (f) High Selectivity of Horizontal Patterns to Different VOCs. 22

Figure 8. Raman Spectra of Pure CNF and CNF after Being Immersed in VOC. 23

Figure 9. Experimental Steps Required for MXene Flake Synthesis: a) Ball Milling, b) Vacuum Heat Treatment, c) Chemical Etching, d) Washing, e) Sonication, and f) Filtration. 32

Figure 10. Characteristic of MXene Nanosheets. SEM Imaging of a) the Stacked MAX Phase, b) Delaminated MXene Nanoparticles, c) a Single Flake MXene, d) EDS Images of MXene Film after Filtration, e) XRD Patterns of MAX and MXene, f) AFM Image of an Individual MXene Nanosheet, g) Tyndall Effect Showing Uniform Dispersion Quality, and h) MXene Nanoparticle Size Distribution. 36

Figure 11. Schematic of the Hybrid 3D Printing Combining (a) the Surface Patterning via µclip (CCD: Charge-coupled Device, BS: Birefringence System, UV: Ultraviolet) with the (b) Surface Topography of Micro Features like Microchannels and Reservoir on the Substrate and (c) DIW of MXene/Ethanol Ink for Directed MXene Assembly with Anisotropic Deposition and Preferential Alignment. (d) Schematic for the Alignment Mechanism with Micro Force Balances Between the Shear from the Ink Flow (F_{c1}), Gravity

(F_g), Drag Force (F_d), Capillarity (F_{c2}), and Van Der Waals (F_{vdw}) Between Adjacent Layers (L_n). 38

Figure 12. The Contact Angle Between PEGDA Flat Substrate and Ethanol is ~18°, Showing Good Wetting Properties. 40

Figure 13. Rheological Properties of $Ti_3C_2T_x$ with a) Different Dispersion Concentrations, b) the Viscosity as a Function of Shear Rates, c) the Storage Modulus (G') and Loss Modulus (G") Vs. Frequency, d) a Photograph Showing the Hybrid 3D Printing Approach with the DIW of Droplets on the µclip-printed Surface Patterns, e) the Optical Images for the Patterned Surface of Linear Grooves e_1) Before and e_2) after Droplet Deposition with e_3) a Zoomed-in Image Showing Homogeneous MXene Distribution, f) Optical Images of Complex Surface Patterning (from Left to Right – Wavy Grooves, Antenna-shaped Circles, Cross-linked Triangle Channels, and Interdigitated Structure) (Scale Bars are 2 mm in e_1 and e_2, 300 µm in e_3 and 1 mm in f). 44

Figure 14. a-c) Simulated Nanoparticle Position Field Within Microchannels Showing the Capillary Driven MXene Transport, Scale Bar Represents the Particle Density Distribution (mg/m^3). 45

Figure 15. a) Optical Images Showing Top Views of Deposited MXene Films on Patterned Substrates for Different <N> (Scale Bar 300 µm), b-d) Cross-sectional 3D Optical Profilometry Images Demonstrating the Microchannel Inner Surface Roughness at <40>, Patterned Surface e) Before and f-h) after Printing 40 Layered MXene for f) 10 mg/ml <40>, g) 20 mg/ml <40>, h) 50 mg/ml <40> (Scale Bar 2 µm and Dashed Lines Show the Interface Between the Substrate and MXene Film). 47

Figure 16. 3D Optical Profilometer-characterized a) Height Profile Across Micro Channeled Surface Patterning, b) Surface Roughness Versus <N>, and c) Thickness Growth and Area Coverage of Multilayered MXene with Concentration-varied Inks (i.e., 10, 20, and 50 mg/ml). 48

Figure 17. SEM Images Showing MXene Film Topography for 10 mg/ml <40> Showing Continuous and Uniform Deposition of MXene Flakes into Microchannels. 50

Figure 18. Electrical and Piezoresistive Properties with a) the Digital Photograph of the Substrate Showing Mechanical Flexibility, b) Sheet Resistance (R_s) as a Function of Printing Cycles <N> For Various Inks, c) the Electrical Conductivity of Pure MXene Film via Vacuum Filtration and Printed Composites of Different MXene Content, d) the Normalized Resistance Vs. Bending/ Flexural Strain, e) Cyclic Performance under Bending and Unloading Cycles from 1% to 50% Flexural Strains, f) the Cyclic Fatigue with Bending and Loading Release Cycles at a 22% Flexural Strain, g) the Printed Device Responding to Finger Motions at Different Bending Angles, h) the Anisotropic Resistance Change as a Function of the Flexural Strain along the Longitudinal (ϕ=0°) and Transverse Directions (ϕ=90°), and i) the Electrical Responses along with the Longitudinal and Transverse Directions in Response to Delicate Wrist Movement. (Note: Figure 18(d,e,f,h)-inward Bending and Figure 18(g,i)-outward Bending Figure 19).. 52

Figure 19. Schematic Showing Bending Sequences for a) Inward Bending Showing Neutral Position, Bending Inward, Releasing, and Stretching of the Film (Figure 18 d, e, f, and h); b) Outward Bending Where the MXene Film Experiences Tensile Stretch. (The Experimental Demonstrations of Finger and Wrist Bending Were Performed with Outward Bending as Shown in Figures g and i).. 54

Figure 20. The Response of MXene-based Sensor to Pressure on Piezoresistive Sensors with the a) Sensing Responses under Pressure Loading and Unloading from 2.34 to 25.95 kPa, b) the Sensitivity as a Function of Pressure, c) the Response Time and Recovery Time of the Sensor to 4 kPa, d) the Mechanical Durability Test under the Pressure of 15 kPa, e) Anisotropic Motion Sensing in a Longitudinal and Transverse Direction, and f) Signature and Handwriting Sensing 56

Figure 21. Finger Tapping and Releasing Response of the PDMS-coated MXene Sensor. 58

Figure 22. a-b) The Schematic Shows the Working Principle of Hybrid Processing Combining FDM and DIW 3D Printing for Directed Assembly of NPs. a) 3D Printing of Templates from FDM-heated and -extruded Thermoplastic Filaments of ABS with Staircase Effect Shown in Optical (Scale Bar 300 µm) and SEM (Scale Bar 100 µm) Images and (b) Showing the Template Effects from DIW-deposited MXene Inks. Specifically, a_1) a Designed CAD Model of a Substrate Consisting of a Reservoir for Ink Deposition, a_2) the FDM-fabricated Template with Stair-stepping Effects Leading to the Formation of Microchannels on Top of the Templated Surface, b) Deposited MXene Inks Were Driven Primarily by the Capillarity Forces Within Microchannels, and b_1) Effects of Template Topology (e.g., Cross-section Shapes of the Substrate Tuned by Different FDM Printing Parameters) on MXene Nanoparticle Assembly Efficiency (e.g., Particle Layer Morphologies and Layer Thicknesses Programmable via DIW Parameters)……............... 70

Figure 23. Surface Template Morphologies. a_1-a_4) Optical Images of FDM 3D-printed Substrates Having Different Layer LH Values (i.e., 20, 100, 150, and 300 µm) with the White Region as the FDM-printed Layer and the Black Region as Microchannels (Scale

Bar 1200 µm), b) Measured Dimensions of Microchannels (i.e., D and W) Depending on the LH Control, Showing the Layer Diffusion and Inconsistency below 50 µm and Layer Debonding above 300 µm and Defining Our Printing Window to Be [50 µm, 300 µm]. Furthermore, the Surface Profile Characterizations Validated This Surface Template Printability in the Confocal Optical Microscope (COM) and SEM Imaging in c_1-c_3), with the Com Showing the Printing Roughness (i.e., an Average Roughness Values of ≈3.6 µm, 11.6 µm, and 38.6 µm as a Result of the Staircase Effect for LH ≈20, 100, and 300 µm) and Zoomed-in SEM Images Showing the Different Interfacial Behaviors, Namely, the Diffused, Clear, and Debonded Interfaces (Scale Bars of 2 µm in SEM Images)........... 72

Figure 24. a) The Schematic Showing the Chemical Etching and Exfoliation Process of Ti_3AlC_2 During the Syntheses of MAX Powders and MXene Nanoparticles, b) SEM Image Showing the MXene Surface Flatness, and c) SEM Image and EDS Scanning of MXene Cross-section Showing the Layered Morphology in Nanoflakes, d) XRD Spectra of MAX Phase and MXene Nanoflakes, e) Viscosity of MXene/Ethanol Inks as a Function of Shear Rates (1-100 1/sec), and f) Viscoelastic Properties (G' and G") of MXene/Ethanol Inks as a Function of Frequency (rad/sec). 74

Figure 25. Optical Imaging of the MXene Ink Transport Distances along Microchannels from the DIW-deposited 5 ml Size Droplets for a) 5 mg/ml and B) 10 mg/ml MXene/Ethanol Colloids with Varying Surface LH (i.e., 50, 100, 150, and 180 µm) (Scale Bar 1200 µm), C) Distance Traveled from the MXene Inks Driven via the Capillary Action Showed Consistent Increases as a Function of LH but Decreased as a Nanoparticle Concentration, D) ANSYS Fluent Simulation Results of MXene Ink (5 mg/ml) Transported

Within Microchannels of Different LH via the Capillary Effect (Scale Bar Represents the Volume Fraction of MXene Ink). 79

Figure 26. a_1-a_4) Optical, SEM, and EDS Maps Showing the Surface Topography and Parallel Stacking of MXene NPs Deposited into Microchannels with 100 μm LH for 5 mg/ml MXene Inks, and b) Schematics Describing the Mechanism of MXene NPs Deposition and Assembly. 81

Figure 27. Fabrication Strategy for Micropatterns with MDIW 3D Printing and Wet Etching. a) Multilayer 3D Printing with MDIW Demonstrating a_1) the Sublayer Formation Mechanism Enabled by Printhead Components Consisting of a Spinneret, a Minimizer, Multipliers, and a Reducer, b) the Distinct Microstructural Change in the Patterning Layer (Pl) and Sacrificial Layer (Sl) at Different Manufacturing Stages, Such as b_1) 3D Printing, b_2) UV Curing, b_3) Wet Etching Followed by Drying to Form Permanent Patterns, b_4) Demonstrating Micropatterned Surfaces for Heat Dissipation Applications in Semiconductor Packaging, and c) Selective Wet Etching of Sl upon Exposure to Etchant and Its Microstructural Evolution as a Function of Time, Showing Intermediate Etching Stages Between the Etchant Solvent and Sl Polymer. 95

Figure 28. Rheological Properties of Feedstock Inks Used for MDIW 3D Printing. a) the Apparent Viscosity of the Epoxy Ink with and Without BNs Fillers as a Function of the Shear Rates, b) Tan Delta (δ) and Dimensional Change (i.e., Printing Line Width) of E-BN Composite Inks Containing Varying BNs Concentrations, c) the Apparent Viscosity of PEI Measured at Different Temperatures, d) Photo-rheology Measurements of the Evolution of Storage Modulus (G') and Loss Modulus (G") During UV Light Irradiation (Light

Wavelength ≈365 nm and Switched off after 10 sec) for Both Patterning Layer (i.e., E-BN25) and Sacrificial Layer (i.e., PEI-50) Samples.. 100

Figure 29. Microstructure of the 3D Printed Multilayer Structures. a_1-a_3) E-BN25 and PEI-50 with Different Layer Numbers <32>, <64>, and <128> (Scale Bar 1200 µm). a_4-a_6) Inset Optical Images Show the Cross-sectional Morphology of the Printed Microlayers (Scale Bar 500 µm), b) Computational Fluidic Dynamic (CFD) Simulations of E-BN25 and PEI-50 Inks for <32> as an Example to Show the Layer Multiplying Mechanism (i.e., Green Sublayer as E-BN25 and Blue Sublayer as PEI-50).. 103

Figure 30. a) Dimensions of the E-BN25 and PEI Sublayers Exhibit Consistent Layer Size Evolutions (i.e., Width Values Decrease Vs. Higher Layer Numbers), and b) XRD Patterns of the E-BN25 Multilayer Composites with Improved BNs Orientations as Layers Multiply.. 105

Figure 31. Etching Kinetics of E-BN25/PEI-50 Multilayer Structures. a) PEI Sublayer Dissolution (%) for <32> By Different Etchants (i.e., IPA, Ethanol, and Water) as a Function of Etching Time (min), b) PEI Dissolution by IPA Etchant at Room Temperature (RT ≈25°C) for Different Layer Numbers, c) Etching Rate (µg/s) of PEI Sublayer as a Function of <N> For Different Etchants (i.e., IPA, Ethanol, and Water) and Bath Temperatures at RT... 106

Figure 32. Microstructure Evolution of MDIW Micropatterns. a) Width and Depth Plot of Micropatterns Depending on the Etching Time for Different Layer Numbers, b) Surface EDS Mapping of the <32> Before and after Etching (Boron Tracing), c) EDS Line Profile of Boron Across the Patterned Surfaces Before and after Etching, d) Optical and SEM Images Show the Cross-sectional View of Micropatterns (i.e., Microgrooves) Fabricated

via Different Multiplying/Layering after IPA Etching at RT (Scale Bar 500 and 100 µm for Optical and SEM, Respectively), and the Corresponding 3D Surface Topography of Etched Samples Showing the Formation of Microgrooves after IPA Etching at RT for e_1) <32>, e_2) <64>, and e_3) <128> Layers. 110

Figure 33. Thermal Capability Demonstrations. a) The Schematic Illustration of Microgrooves as Channeled Microfluidic Cooling Systems, b) Measured Thermal Property (i.e., Conductivity, Diffusivity) Values of the Composite as a Function of BN Concentrations, c) Theoretical and Experimental Thermal Conductivity Values of E-BN25 for as a Function of Measured Surface Area (i.e., <32> Layer Number Exposed the Highest Surface Area Due to the Shape Distortion, as Shown in Figure 32d), d) Average Surface Temperature and Average Heat Flux of E-BN25 <32> With Air (No Coolant) and Coolant Liquids (i.e., Oil, Water, and Liquid Metal) Confined Between Microchannels (as Shown in Schematic 6a) for <32> Samples, e) IR Images of Composite Microchannel Surfaces for E-BN20, E-BN25, and E-BN25C, f) Comparison of the Surface Temperature of E-BN25 and E-BN25c for <32>, and g) Simulation Results Showing the Temperature Distribution Profile for E-BN25P, E-BN25, and E-BN25C Without/With the Cooling Liquids. 112

Figure 34. Contact Angle Measurement from the Shape of the THF Droplet wrt (a) Glass (b) 3D Printed Substrate with Gratings (c) Resin Film (Contact Angle Measurements of Substrate Were Performed Using the Rame-Hart Automatic Goniometer).................... 137

Figure 35. Raman Spectra of Pure CNF and CNF after Immersed in VOC. For Raman Measurements, Confocal Raman Equipment (Alpha500 Ra, Witec) with a Laser Frequency of 532 nm (Second Harmonic Generation) Was Used. An Area Scan with an Integration Time of 1 S with 50 Points per Line and 50 Lines per Image Were Taken with a

Measurement Time of 39 min in Total. The Laser Beam Was Directly Focused on the Sample Surface Using a 20/.4 Zeiss Objective. 137

Figure 36. SEM Images of the Cross-section of the Complex Substrate after Coating with 10 mg/ml <15> Showing a Thin Film of MXene Deposited at Intricate Channels Shapes a) Wavy Grooves, b) Antenna-shaped Circles, c) Cross-linked Triangle Channels, and d) Interdigitated Structure. The Zoomed-in Images (a_1-d_1) Showing Layer-by-layer Deposition of MXene Flakes. 139

Figure 37. Contact Angle Measurements for Printing Materials of a) PEG, b) E-BN25, and c) PEI ($\theta_{PEG\text{-}glass}$= 35.89°, $\theta_{E\text{-}BN25\text{-}glass}$=44.17°, $\theta_{PEI\text{-}glass}$=63.43°) on Glass Substrates 141

Figure 38. Storage Modulus (G’) and Loss Modulus (G") as a Function of Shear Stress for a) E-BN Inks at a Varying Concentration of BNs and B) PEI at Room Temperature (RT) and 50°C 141

Figure 39. Thixotropic Properties of E-BN25 Ink, Simulating the Printing Condition with Alternating High and Low Shear Rates 142

Figure 40. The Optical Image Showing the Interfacial Phenomena at the Polymer/Polymer Interface Between a) E/PEG30-H (Diffusion) and B) E/PEI (No Diffusion) (Scale Bars 500 µm). 142

Figure 41. The Average Surface Roughness (S_a) of the MDIW Micropatterns was Measured Using an Optical Profilometer after Etching in IPA (RT) as a Function of Etching Periods (min).. 143

Figure 42. SEM and Optical Images of a Cross-sectional View of 3D Printed Templates Demonstrating Stairstep Topology for a) LH 20 µm, B) LH 100 µm, C) LH 150 µm, D) LH 300 µm.. 145

Figure 43. a) Ti_3AlC_2 MAX Particle Morphology with the Characteristic Layered Structure (Scale Bar 2 µm), b) MXene Particles after Etching Show Accordion Structure (Scale Bar 1 µm). 146

Figure 44. The Measured Static Contact Angle Between Ethanol and Flat ABS Surface 146

Figure 45. SEM Images of the a) Top View of the Patterned MXene Film at Microchannel with Continuous Morphology and b) Parallelly Stacked MXene Flakes for 5 mg/ml #5. 147

CHAPTER 1

INTRODUCTION

Nanoparticles (NPs) are ideal building blocks for a variety of functional materials due to their unique properties and functions which are not achievable at the macroscale due to their high structural defect density and manufacturing limitations.[1] To fully exploit the potential of NPs, and their functional properties such as mechanical strength, thermal dissipation, electrical conductivity, and optical properties, precise control over the orientation and spatial arrangements are requisite which depend on NP size, shape, patterns, and surface functionalities.[2–6] For instance, zero-dimensional (0D) NPs, such as nanospheres and nanodots, one-dimensional (1D) NPs including nanorods (NRs), nanowires (NWs), and nanotubes (NTs), as well as two-dimensional (2D) NPs like nanoflakes and nanosheets display intriguing functional properties.[2–6] As a result, these nanomaterials can be used to develop unique nanodevices and nanosystems suitable for various applications in fields such as structural protection,[7,8] thermal energy management,[9,10] microelectronics,[11,12] quantum science,[13,14] nanorobotics,[15,16] and pharmaceutical engineering[17–19]. However, during practical applications, the discontinuous and disordered nature of powder-like NPs does not allow them to exhibit their theoretical properties.[2,20] Therefore, the creation of long-range ordered structures is necessary to harness the full potential of functional NPs in practical products and systems.

To address these challenges and opportunities, various strategies have been developed for self-assembly and directed self-assembly to achieve ordered structures. Strategies like exploiting molecular interactions, NPs surface functionalization, application of external fields, and utilization of physically and chemically patterned templates can produce complex and functional architectures from smaller subunits, with dimensions ranging from as small as 10 nanometers to several centimeters.[20–23] Template-based directed assembly is a promising approach to impose the ordering of NPs more precisely than a flat surface. With templates of specific shapes (e.g., trenches, microwell, gratings), the interactions between the NPs and the template can be harnessed to precisely control the arrangement of NPs and produce highly ordered structures with a desired geometry.[24–27] Various nanomanufacturing techniques can be employed for the fabrication of templates. Some of the most used lithography-based methods are electron beam lithography (EBL),[28,29] ion beam lithography (IBL),[53] optical lithography (OL),[30,31] soft lithography (SL),[32,33] direct write lithography (DWL),[34] and nanoimprint lithography (NIL)[35]. In addition to these, vapor deposition-based protocols such as physical vapor deposition (PVD),[36] chemical vapor deposition (CVD),[37] atomic layer deposition (ALD),[38] and plasma-enhanced CVD (PECVD)[61] are also widely used. These methods enable the generation of high-resolution features down to less than 10 nm with either high precision or structural diversity. However, these techniques require molds, dies, and masks with complex manufacturing and delicate polymer chemistry to control processing precisions, leading to a reduction in development time and high cost.[39–41] Other techniques, such as three-dimensional (3D) printing,[42] micro-molding,[43] polymer grafting,[44] and wrinkling,[65] are also being investigated for template fabrication and NP assembly by coupling with evaporative-driven assembly.

Additive manufacturing, commonly referred to as 3D printing, is a technology that enables the creation of 3D objects using a layer-upon-layer approach, which is not achievable via conventional subtractive manufacturing techniques. 3D printing is broadly classified into seven primary categories based on the printing mechanisms employed, including extrusion-based methods like fused deposition modeling (FDM) and direct ink writing (DIW); vat polymerization-based methods like stereolithography (SLA), micro-continuous liquid interface production (μCLIP), and digital light polymerization (DLP); material jetting-based methods like PolyJet, MultiJet, electrohydrodynamic (EHD), and aerosol jet; powder bed fusion (PBF)-based methods like selective laser melting (SLM) and selective laser sintering (SLS); directed energy deposition (DED)-based methods like electron beam melting (EBM) and laser engineering net shape (LENS); and sheet lamination-based methods like laminated object manufacturing (LOM).[45–48] 3D printing materials include polymers, metals, and ceramics in the form of powders, colloids, solutions, gels, and filaments. To incorporate NPs into 3D printing, nanomaterials are mixed either with solvent, polymer, or photocurable resins depending on the type of 3D printing methods.[49,50]

Recent development in 3D printing has led to the integration of functional NPs into highly complex, heterogeneous, and functional architectures to achieve NP assembly and surface micropatterning. The NPs deposition and assembly with 3D printing materials is driven and assisted with physical phenomena such as evaporative,[51] mechanical,[52] electrical,[53] magnetic,[54] optical,[55] and thermal[56] phenomena. NPs in 3D printed structures can impart tunable, functional properties for various applications in areas such as thermal packaging,[57,58] microelectronics,[59,60] optoelectronics,[61,62] structural composites,[63,64] and biomedicine[54,65]. The nanomaterial patterning and assembly can modulate the nanoscale effects such as NPs deposition, concentration, and orientation during 3D printing. As a result, the use of 3D printing displayed the potential to revolutionize nanomanufacturing by enabling the fabrication of scalable, complex, and intricate structures with high accuracy and precision.[66–68]

The integration of high-performance nanoscale materials onto non-native templates enables new kinds of heterogeneously integrated systems with desirable architectures and functionalities that are not readily accessible by conventional means. 3D printing combined with colloidal and template controls can enable the precise positioning and orientation of the NPs within the microstructure, resulting in a high degree of control over the microstructure's properties and functionality. As mentioned, 3D printing is capable of intricate microstructure design and rapid prototyping, including surface topology management for template-influenced nanoparticle assembly.[69–71] On the other hand, NP suspension-based deposition and evaporative-driven assembly have shown success in manipulating nanoscale morphologies of small molecules and nanoparticles. For example, during evaporation-based assembly, nanoparticles get dragged onto the substrate surface, experiencing long-range and short-range forces, facilitating positional and orientational orders of 1D nanofibers and 2D nanoflakes. In addition to a well-aligned morphology, the high-resolution and high-aspect ratio patterning of nanoparticles over a macroscale area is essential for tuning the composite structures' functional properties. Thus, approaches that enable anisotropic micropatterning and ordered assembly with face-to-face and edge-to-edge contact between nanoparticles (e.g., 1D nanofibers and 2D nanoflakes) on complex 3D substrates are required. The technique should possess the potential for fast, scalable, large-volume, and low-cost patterning and assembly of general nanoparticles for broad applications. Therefore, this research will demonstrate new manufacturing techniques demonstrating nanoparticle assembly effectiveness and efficiency with a few functional devices as examples.

1.1 Research Objective

This research presents facile and efficient layer-by-layer-based processing that combines 3D printing and NP colloidal science for assembling and micropatterning 1D and 2D NPs.

- Developed a new approach combining SLA 3D printing and dip coating for a regulated deposition and uniaxial orientation of 1D CNF. The synergistic effect of both engineered surface roughness through SLA and nanoparticle interactions at the substrate-dispersion interface during dip-coating facilitated the ordered assembly of CNF. Furthermore, the investigation of the electrical conductivity, sensitivity, and selectivity to chemical vapors or low-strain deformations validated the assembled CNF bands with enhanced properties due to long-range orders.
- Utilized a versatile approach combining advanced μCLIP and DIW 3D printing techniques for the assembly of 2D MXene flakes. The hybrid manufacturing of μCLIP/DIW fabricated high-resolution micropatterns with parallelly deposited and anisotropically aligned 2D MXene flakes on 3D printed flexible substrates. The examination of the structural, electrical, and piezo-sensing properties of patterned MXene films demonstrated the improved packing factor and orientations for multifunctional devices.
- Leveraged an in-house printhead for polymer co-extrusion of multilayer and multiphase lamellar film via multiphase direct ink writing (MDIW), which showed a few advantages over conventional single-phase printing. The multilayered film with alternate layers of epoxy (retaining layer) and polyethyleneimine (PEI)

(sacrificial layer) was fabricated followed. Followed by wet etching of the sacrificial layer, the surface patterning contained features ranging from ~10-100 μm. The etching kinetics (i.e., controlled by the etchant type, soak time, the intensity of etching, and temperature) for selective removal of sacrificial polymeric layers generated large-scale micropatterns of epoxy with submicron features. Also, the fabricated epoxy-boron nitride micropattern generated a two-phase cooling system with liquid coolant confined at the patterned region for heat dissipation applications.

- A hybrid 3D printing approach combining FDM and DIW 3D printing for the anisotropic deposition of 2D NPs was studied. The staircase defects were generated on FDM printed surfaces by controlling printing parameters (i.e., layer height and print orientation). The staircase surface morphology was utilized as the confined environment to form a directed assembly of 2D MXene NPs into long-range patterned microstructures with parallelly stacked morphology. The ordered surface patterning can form by combining the confinement effect from surface microchannels, MXene ink quantity control, and NP-substrate interactions.

CHAPTER 2

SCALABLE ALIGNMENT AND SELECTIVE DEPOSITION OF NANOPARTICLES FOR MULTIFUNCTIONAL SENSOR APPLICATIONS

Abstract: Here reported is the layer-by-layer-based advanced manufacturing that yields a simple, novel, and cost-effective technique for generating selective nanoparticle deposition and orientation in the form of well-controlled patterns. The surface roughness of the 3D-printed patterns and the solid-liquid-air contact line, as well as the nanoparticle interactions in dipped suspensions, determine the carbon nanofiber (CNF) alignment while the presence of triangular grooves support the pinning of the meniscus, resulting in a configuration consisting alternating CNF and polymer channels. The polymer/nanoparticle composites show ten times lower resistance along with the particle alignment direction than the randomly distributed CNF networks and six orders of magnitude lower than that along the transverse direction. The unidirectional alignment of the CNF also demonstrates linear piezoresistivity behavior under small strain deformation along with high sensitivity and selectivity towards volatile organic compounds (VOCs). The reported advanced manufacturing shows broad applications in microelectronics, energy transport, light composites, and multi-functional sensors.

2.1 Introduction

The interest in the area of nanoscience is transitioning from the design and synthesis of nanomaterials with attractive morphologies to their assembly into larger systems. There are numerous ways of assembling nanomaterials using appropriate interactions, such as interparticle interactions, external fields, and templating agents. Chapter 1 introduces the

3D printing and dispersion-mediated nanoparticles template-based self-assembly of 1D nanomaterials. 1D nanomaterials possess unique and anisotropic properties and thus are highly desired in areas, such as energy storage,[72,73] sensors, [53,74] drug delivery,[75,76] tissue engineering,[77] and composite manufacturing.[78] These nanomaterials only succeeded in rare cases in translating their theoretically predicted properties into practical applications due to their poor dispersion and lack of alignment. Therefore, achieving optimum assembly of 1D nanoparticles with controlled deposition morphology is highly desired to increase their functional properties, such as to obtain superior material utilization with a reduced scattering of electrons and phonons at matrix nanoparticle interfaces.[79] However, the preferential alignment and desirable site placement of 1D nanomaterials are challenging due to their high surface area and large aspect ratios, resulting in a high degree of nanoparticle aggregation and extra rotational momentum at the nanoscale, respectively.[80] To date, several techniques have been reported to control the alignment of 1D nanomaterials, including the use of in-situ gas or solution synthesis,[81–83] electric or magnetic fields,[84,85] shear force,[52] fluidic flow,[86] liquid crystals,[87,88] and block copolymers.[89,90] However, these approaches require complex manufacturing procedures and have a rather low fabrication rate to achieve large-area or large-volume nanoparticle morphologies, especially for selective alignment and complex 3D architectures. Thus, there is much need to innovate a manufacturable and scalable fabrication process that can gain precise orientational and positional control of nanoparticles.

The integration of the above-mentioned high-performance nanoscale materials onto non-native substrates enables new kinds of heterogeneously integrated systems with desirable architectures and functionalities that are inaccessible by conventional means.

Recently, the 3D printing technique is used as a key technology for nanoparticle deposition or alignment to obtain high-performance nanocomposites. It is capable of designing and fabricating complex, multifunctional structures with higher precision than traditional top-down approaches.[91] In previous studies, 3D printing technology coupled with external fields like shear forces in DIW,[92] electric or magnetic field in SLA,[93] acoustic and flow forces in FDM,[64,94,95] and electric field in EHD[96] has been used to enhance the control of filler orientations. Although powerful, most of these 3D printing mechanisms, especially those involving electrical or magnetic fields, are sensitive to filler concentrations and field-filler interactions. The use of micro-scale fillers such as carbon fibers or glass rods also limits the printing resolution due to the formation of aggregated chunks instead of loosely packed or individualized nanoelements. Chemically and physically modified micro/nano surface patterning techniques have also been used for nanostructure alignment on large and small scales. However, these techniques pose challenges, such as distortion of elastic materials, poor adhesion to the substrate, and time-consuming experimental steps, not to mention their poor scalability above micron levels.[97] As a result, an alternative approach for the microfeature surface patterning technique with an acceptable degree of scalability and repeatability is highly desired.

In this chapter, we present a facile and efficient layer-upon-layer-based processing method that combines 3D printing and dip-coating for nanoparticle assembly. 3D printing is capable of intricate microstructure design and rapid prototyping, including surface pattern fabrication for template-influenced nanoparticle assembly.[69–71] Dip-coating, on the other hand, can manipulate nanoscale morphologies of both small molecules and nanoparticles.[98,99] Through the combination of both methods, it is observed that a regulated deposition and uniaxial orientation of the highly anisotropic carbon nanofiber (CNF) is well controlled by the synergistic effect of both engineered surface roughness through SLA and nanoparticle interactions at the substrate-solvent interface during dip-coating. The fabricated composites display directional electronic conductivity, demonstrating high sensitivity and selectivity to chemical vapors as well as low strain deformations. Additionally, the selective coverage of CNF on substrates was consistent between micro- and centimeter-sized polymer patterns, showing the highly efficient pick-and-place operations with sub-micrometer accuracy in manipulating mesoscale components (ranging from hundreds of nanometers to micrometers) containing assemblies of some of the down-to-nanoscale particles. The merits of our manufacturing encompass scalable assembly with high precision and high throughput and enhanced interfacial properties between heterogeneous materials to ensure desirable electrical contact.

2.2 Experimentation and Characterization

2.2.1 Carbon Nanofiber Dispersion Preparation

To obtain a uniform suspension, 10 mg of CNF (length 20 - 200 μm and a diameter of 100 nm, Sigma-Aldrich (Figure 1a)) was added to 10 ml of tetrahydrofuran (THF, anhydrous, ≥99.9%, inhibitor-free, Sigma-Aldrich), dimethyl sulfoxide (DMSO, ACS reagent 99.9%, 472301, Sigma-Aldrich), N, N-dimethylacetamide (DMAc, anhydrous, ≥99.8%, Sigma-Aldrich) and, dimethylformamide (DMF, ACS reagent, 99.8%, 319937, Sigma-Aldrich) (anhydrous, ≥99.9%, inhibitor-free, Sigma-Aldrich) as received (i.e., 1 mg ml^{-1}) and was mixed by a vortex mixer for 5 minutes and was sonicated for 24 hr. The 1 mg ml^{-1} CNF dispersion quality is shown in Figure 1b.

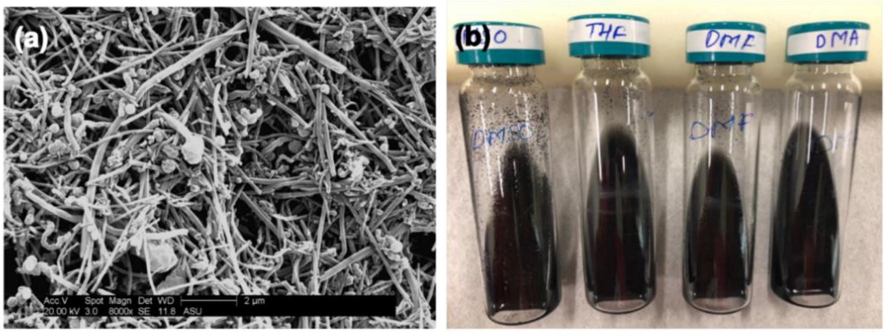

Figure 1. (a) As received CNFs from Sigma-Aldrich (scale bar 2 µm), (b) the CNF dispersion with different organic solvents (e.g., DMSO, THF, DMF, and DMA) with 1 mg of CNF in 10 ml solvent prepared by 24 hr of ultrasonication.

2.2.2 SLA 3D Printing

Formlabs 2 stereolithographic printer was used to 3D print the substrate patterns through layer-by-layer curing of photosensitive resin, a mixture of the methyl acrylate oligomer/monomer, and the photoinitiator ordered from Formlabs and used as-obtained. The design consisted of a triangular grating of approximately ~75 µm height and a channel width of ~50 µm with a periodicity of 200 µm over a 1×1 cm^2 sample area. After printing, patterns were thoroughly cleaned and cured at 55°C for 40 minutes in a Form UV curing chamber to achieve a robust substrate.

2.2.3 Anisotropic Alignment of Carbon Nanofibers

CNF/THF suspension was observed with minimum sedimentation over 24 hours, demonstrating better stability as compared to other organic solvents. The printed epoxy substrate with controlled surface topology features was dipped in a 1.0 mg/ml CNF/THF suspension where the channels were kept parallel to the solvent-air interface in a vacuum heated at 50 °C for dry samples ($E/CNF_{1.0\text{-}h}$). To compare with the (i) horizontal dipping samples ($E/CNF_{1.0\text{-}h}$), two substrates with (ii) the flat surface preferring no dipping directions ($E/CNF_{1.0}$) and (iii) the patterned surface for vertical dipping where the channels were perpendicular to the solvent-air interface ($E/CNF_{1.0\text{-}v}$) were also performed with same CNF/THF suspensions. The details regarding the sample preparation of assembled CNF are provided in Table 1.

Table 1. Nomenclature of Assembled Samples

Sample	Manufacturing process	CNF/ THF concentration (mg/ml)
E	As-obtained surface patterns from 3D printing of epoxy	0
$E/CNF_{0.1\text{-}v}$	Vertical dipping (3D printed substrates having channels perpendicular to the solvent-air interface)	0.1
$E/CNF_{0.5\text{-}v}$		0.5
$E/CNF_{1.0\text{-}v}$		1.0
$E/CNF_{10.0\text{-}v}$		10.0
$E/CNF_{0.1\text{-}h}$	Horizontal dipping (3D printed substrates having channels parallel to the solvent-air interface)	0.1
$E/CNF_{0.5\text{-}h}$		0.5
$E/CNF_{1.0\text{-}h}$		1.0
$E/CNF_{10.0\text{-}h}$		10.0
$E/CNF_{0.1}$	Flat substrate dipping (Dipping of the 3D printed substrate without any surface features in any direction)	0.1
$E/CNF_{0.5}$		0.5
$E/CNF_{1.0}$		1.0
$E/CNF_{10.0}$		10.0

2.2.4 Electrical/Sensing Measurements of Epoxy/CNF Electrodes

The electrode was prepared by attaching conductive aluminum wires to the nanoparticles-coated sample surfaces via silver paste adhesive. The electrical conductivity of the composite was studied using a PARSTAT-2273 potentiostat from Princeton Applied Research. The CNFs prepared on top of polymer patterns were then embedded inside polydimethylsiloxane (PDMS) (SYLGARD™ 184, Dow Chemical) as a fabricated device. The sensitivity of the fabricated devices to mechanical strain (with PDMS) and chemicals (without PDMS) was measured by a Keithley DMM7510 7 1/2 digital multimeter. All sensing responses were analyzed by measuring the resistance change across the two contacts when exposed to strains and analytes. For axial strain sensing measurements, the samples were mechanically deformed by Discovery HR-2, TA Instruments at 0.25 Hz frequency. The chemical sensing measurements were conducted using an in-house designed experimental set-up as shown in Figure 2. Before the injection of the target gas, the E/CNF sensor was exposed to pure air to stabilize the baseline. Then, the sensor was exposed to the target VOC for 30 sec, followed by a purging of air for recovery of the baseline. Volatile organic compound vapors were generated by blowing controlled flows of dry clean air into a bubbler filled with 20 ml of selected solvent. The VOC generation rate was calculated by measuring the mass change over certain periods. The generated vapors were then diluted with another controlled dry clean air to the desired concentration and are together blown into a cube containing the sensor. The overall flow rate was controlled at 200 ml min^{-1} and the calculated concentration is in a weight-to-volume ratio in parts per million (ppm). The VOC bubbling rate was lowered from 200 to 10 ml.min^{-1} to lower VOC concentration. All sensing responses were analyzed by measuring the resistance change across the two contacts when exposed to analytes. The response is measured as $((R_{gas}-R_0/R_0)*100)$. R_{gas} is the device resistance with the presence of analyte gas and R_0 is the film resistance in clean air. The in-house designed set-up was connected with a Keithley DMM7510 7 1/2 digital multimeter to record the electrical resistance.

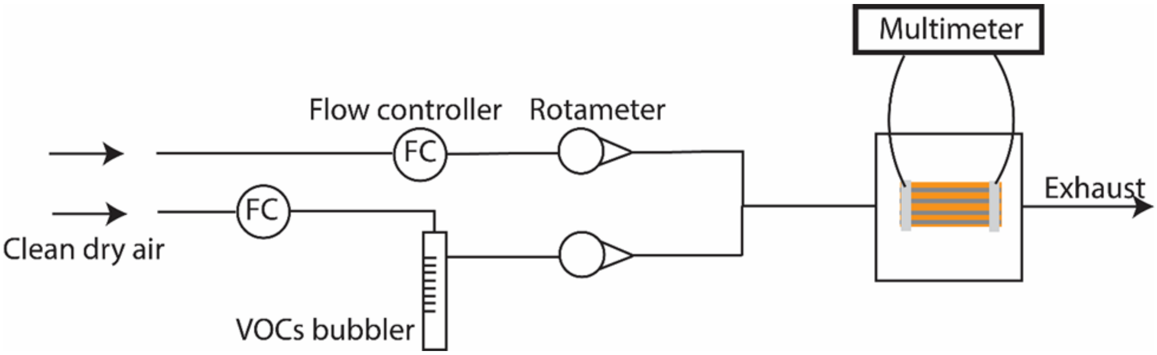

Figure 2. The self-assembled setup is used to perform organic chemical vapor sensing measurements.

2.3 Results and Discussion

2.3.1 SLA 3D Printing

A commercially available SLA was selected for the 3D printing of templates, with the working principle depicted in Figure 3. As a laser beam is projected onto a piezo stage to control the x and y directional movement, it initiates the photopolymerization process in the epoxy-based resin to commence 3D printing (Figure 3a$_1$). A simple alternating pattern of triangular grating with ~100 µm base and ~200 µm spacing is constructed as shown in the zoomed image (Figure 3a$_1$), with true surface topography confirming the height of ~75 µm.

2.3.2 Anisotropic Assembly of CNFs

The CNFs are assembled into straight, wavy, and random orientation morphology depending on the interaction between the CNF dispersion and template surface (i.e., dipping methodology as described in section 2.2.3). Scanning electron microscopy (SEM) images of the flat substrate after dipping show a randomly oriented CNF network with neither preferential deposition nor any preferential alignment of CNF (Figure 3b). In comparison, both vertical dipping and horizontal dipping showed a substantial amount of deposited CNF with alignment along with the solvent−air interface and having different patterning morphologies (Figure 3c,d). The contact angles of both flat and patterned substrates were studied with THF, and an improved hydrophilic surface was observed with the addition of triangular gratings (Figure 34), which is consistent with the "Wenzel model" of wettability.[100] The convective flow of suspension induced by the evaporation of the solvent at meniscus drags CNF toward the contact line (f1). The pinned CNF at the meniscus experiences the van der Waal torque (f2) and the pulling force (f2) is possibly caused by nanoparticle migration and subsequent surface tension gradient that direct nanoparticles to the highest interface curvature molded by gratings of the substrate.[98] As a result, the CNF will be aligned parallel to the interface to minimize the surface energy due to more stable thermostatic states. The first CNF is anchored along with the meniscus, acting as a director for the layer-by-layer assembly of subsequent CNF due to capillary force (f4) between them (Figure 3a$_2$).[99] The friction between the substrate and CNF dispersion due to grating existence helps to anchor the contact line for a long time until gravitational force exceeds the pinning force, which gives rise to the formation of closely packed patterns of aligned CNF.[101] Nevertheless, during vertical dipping (Figure 3c), the microscale morphology of the CNF band changes from straight to wavy shapes due to the pattern resemblance of a sinusoidal wave, resulting in a non-uniform CNF deposition with varying band spacing from ~10-400 μm and demonstrating the potential to further modify the bandwidth and pattern spacing via thermodynamic parameter controls. In comparison, a more precise nanoparticle deposition is observed for horizontal dipping where the solvent-air contact line is parallel to the triangular gratings, enabling more efficient anchoring of the aligned CNF with a uniform spacing of ~200 μm (Figure 3d).

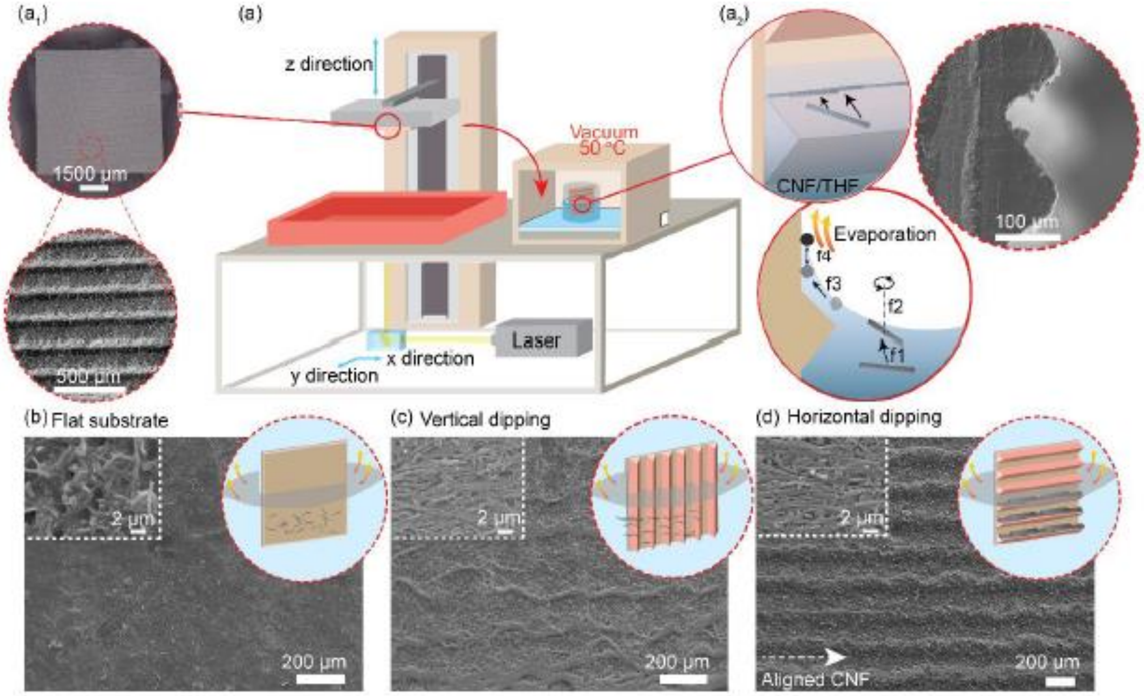

Figure 3. (a) Schematic diagram of the fabrication process combining the stereolithography (SLA)-based patterning and coating-based assembly technology for aligned nanoparticle composites. (a_1) 3D printed substrate surfaces. (a_2) Schematic of the aligning mechanism during dip coating with front and side views. SEM images of (b) flat substrate after dip-coating, (c) surface patterned substrate with vertical dipping, and (d) patterned substrate with horizontal dipping (Inserted images in are the magnified SEM images).

2.3.3 Electronic Properties

To investigate the compatibility of our assembling approach for nano-electronic device fabrication, electronic transport measurements were carried out for 0.1, 0.5, and 1 mg/ml samples, as shown in Figure 4 in both directions parallel and perpendicular to the CNF alignment, namely longitudinal and transverse direction, respectively. To visualize the anisotropic conductivity of the substrate, a 5V light bulb is connected between a voltage source and a 5 mm E/CNF$_{1.0\text{-h}}$ substrate. When the substrate is connected in the longitudinal direction with the circuit, the light bulb is turned on, and while the substrate is connected in the transverse direction, the light bulb is turned off (Figure 4a). The linearity of the current-voltage (I-V) curves implies the ohmic behavior of the CNF films from -2.0 to 2.0 V for different concentrations of CNF (i.e., E/CNF$_{0.1\text{-h}}$, E/CNF$_{0.5\text{-h}}$, E/CNF$_{1.0\text{-h}}$) in both longitudinal and transverse directions. The current responses show a proportional increase with CNF concentration, and are likely due to highly dense bundle formation, resulting in lowered resistance. The morphology of aligned CNF bands (E/CNF$_{0.1\text{-h}}$, E/CNF$_{0.5\text{-h}}$) and randomly oriented CNF NPs film (E/CNF$_{10.0\text{-h}}$) on the 3D printed substrate is shown in Figure 5. Figure 4b compares the anisotropic behavior of the substrate with varying CNF concentrations. For all three concentrations, longitudinal resistance is consistent ~10 times lower compared to samples with random CNF nanoparticles, with E/CNF$_{1.0\text{-h}}$ having the lowest sheet resistivity of 0.27 kΩ sqr^{-1}. The electrical conductivity along the transverse direction is in the order of 10^7 kΩ, six orders of magnitude higher than that along the longitudinal direction.

The anisotropic electrical property is attributed to fast electron transport parallel to the alignment direction between adjacent CNF due to better positional continuity and orientational alignment but is blocked by an insulating polymer matrix in the direction perpendicular to alignment (Figure 4c). Additionally, the deposited CNF between the 3D-printed grooves shows high stability due to their unique anchoring deposition mechanism. Scratch tests with different materials having various surface roughness were conducted under 1 MPa axial pressure with moderate rotational speed for 5 seconds. The resulted resistance shows a maximum change of 0.8% for tissue paper and a minimum variation of 0.01% for brush, demonstrating the effectiveness of micro-scale surface roughness in protecting nanoparticles from peeling off upon contact (Figure 4d).

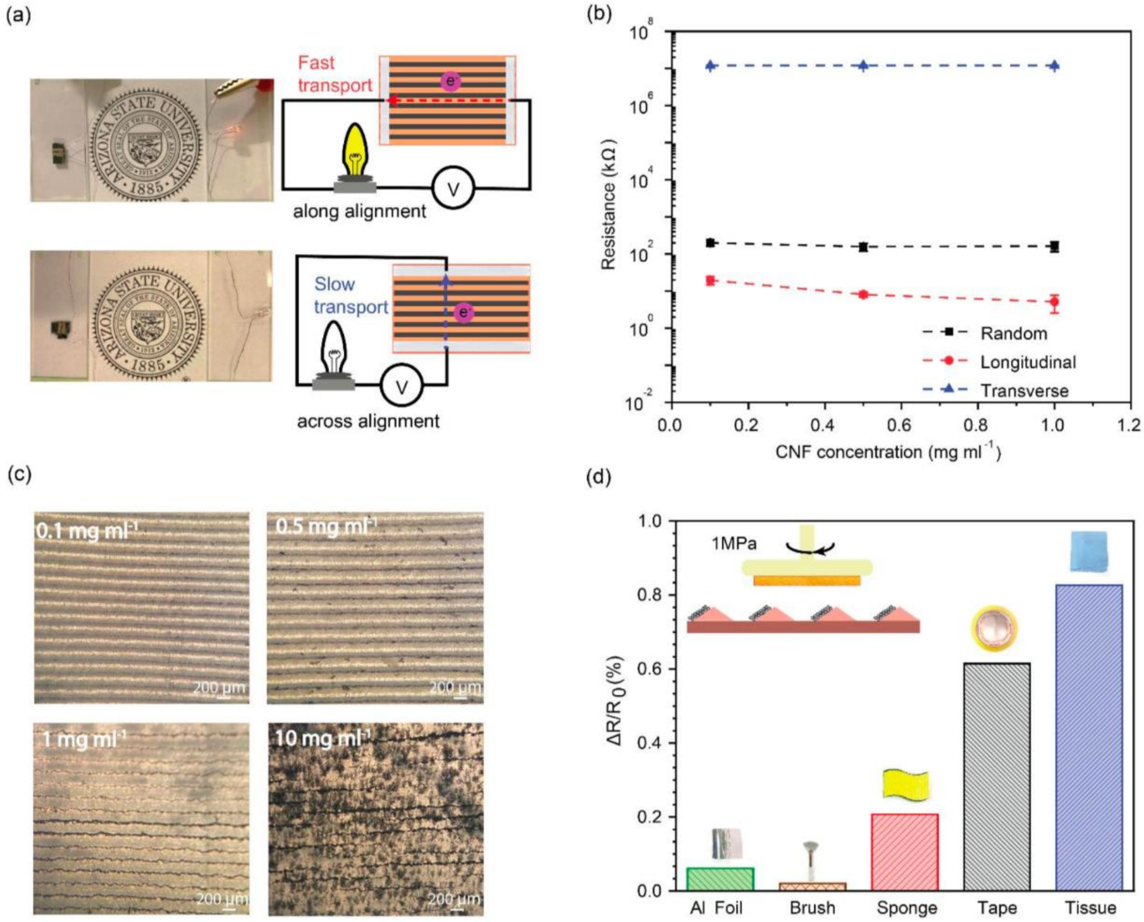

Figure 4. (a) The anisotropic electrical conductivity of epoxy/CNF composite with light bulb demonstration, (b) Resistance values of samples along with the longitudinal and transverse directions as compared to samples with random CNF distributions. (c) Optical micrograph of the dip-coated substrate in the dispersion of different concentrations (i.e., 0.1, 0.5, 1.0, and 10 mg/ml), (d) Change in electric resistance after scratching CNF patterned surface with different materials.

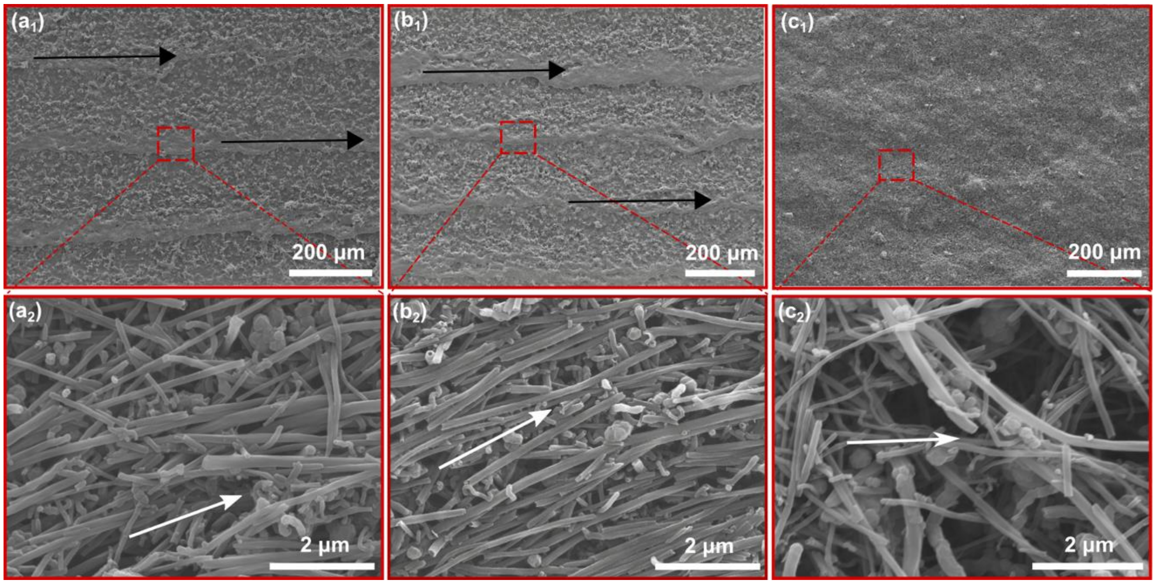

Figure 5. SEM micrographs show morphologies of CNF bands assembled on 3D printed substrates by horizontal dipping of different concentrations (a_1, a_2) E/$CNF_{0.1\text{-}h}$, (b_1, b_2) E/$CNF_{0.5\text{-}h}$ and, (c_1, c_2) E/$CNF_{10.0\text{-}h.}$

2.3.4 Piezoresistive Properties

The functionality of the CNF-aligned composite, E/$CNF_{1.0\text{-}h}$ substrate was further investigated for its piezoresistivity and VOC sensing capability, results are shown in Figure 6. Figure 6a characterizes the resistance response of E/$CNF_{1.0\text{-}h}$ under a tensile strain of 10%. From the slope of the curve, the gauge factor was calculated to be 7.75. The continuous deposition of the CNF was also shown to illuminate a light bulb at 0% strain, but as the substrate stretched beyond 10%, the light bulb goes off due to cracks and gaps generated between the particles, which prohibit electron transport between the particles,[100] suggesting an application as switchers. The high linear response is believed to be contributed by the highly ohmic conduction mechanism and uniform CNF deposition. To examine the mechanical stability and sensing repeatability, E/$CNF_{1.0\text{-}h}$ was subjected to multiple loading/unloading cycles for different tensile strains (Figure 6b). The variation in relative resistance upon stretching and releasing at a maximum strain of 1.0%, 3.0%, 5.0%, 7.0%, and 10.0% was measured to be 7.32%, 16.08%, 17.43%, 27.27%, and 36.95%, respectively. The resin-based composites are mechanically robust, and no PDMS-polymer/nanoparticle interfacial debonding was observed even when the PDMS was stretched up to 50%. To test the cyclic stability of the sensor devices, a new substrate was stretched at 3.0% for 22 cycles (Figure 6c). For the first five cycles, the resistivity response gradually decreased from 10% to 5% and remained constant for the remaining cycles. This is likely due to the disruption of the epoxy crossing link bonds, which resulted in weakened mechanical properties, leading to less continuous CNF intercrossing.[96] After the substrate was stabilized under a fixed 3.0% strain, the electrical response was also stabilized. These results demonstrate that the sensitivity of the fabricated devices is both consistent and repeatable for low-strain monitoring systems.

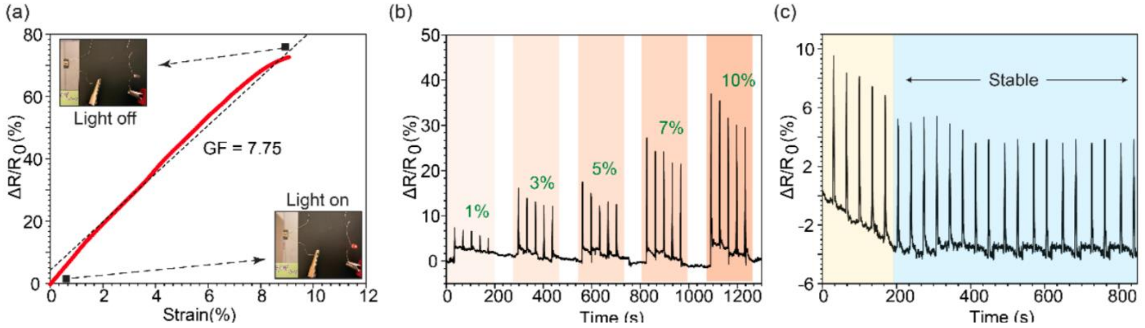

Figure 6. (a) Relative changes in resistance versus strain from 0 to 10%, (b) relative change in resistance for loading-unloading cycles of different strains, and (c) relative change in resistance for multiple cycles at 3.0% strain.

2.3.5 Volatile Organic Compounds (VOC) Sensing of Patterned Substrate with Horizontal Dipping

The sensitivity and selectivity of a horizontally dipped substrate (E/CNF$_{1.0\text{-h})}$ to VOC at low concentrations were characterized due to their high health and environmental-related risks. To do so, the fabricated device was tested for its sensing capability of several organic solvents, including methanol, ethanol, acetone, and dichloromethane (DCM) in vapor forms. Figure 7a-e show the sensitivity of the sensors to (d) methanol, (e) ethanol, (f) acetone, and (g) dichloromethane (DCM), with the lowest concentration of 15 ppm (d-f) and the high signal-to-noise ratio at high concentrations (>30 ppm). The sensitivity is attributed to the high conductivity enabled by the nanofiber alignment without organic solvent adsorption, as well as the high resistivity when organic solvent served as a barrier to the device’s charge transport capabilities. The mechanism for sensing hydrocarbon and hydro-chlorocarbon solvents can be expressed as a cumulative effect of dielectric constant, wettability of particles, and electrical conductivity of solvents.[102,103] Moreover, adsorption of reactive chemicals would lead to the physical separation between the CNF through swelling of the epoxy matrix, which increased the electric resistance. Raman results (Figure 35) also reveal uplift in G band position and changes in I_D/I_G integrated ratios (i.e., 0.083, 0.23, 0.20, 0.17, and 0.15 for pure CNF, DCM, methanol, ethanol, and acetone, respectively) before and after exposing to these organic solvents as shown in Figure 8. This difference is attributed due to the generation of defects when particles are exposed to chemical solvents (e.g., from liquid to residue in the air). Compared to sensors with aligned nanoparticles, randomly distributed CNF showed much lower responses to VOC exposures (i.e., ~1.5% for random CNF vs. ~7% for horizontal CNF) with a demonstration at 25 ppm (Figure 7f).

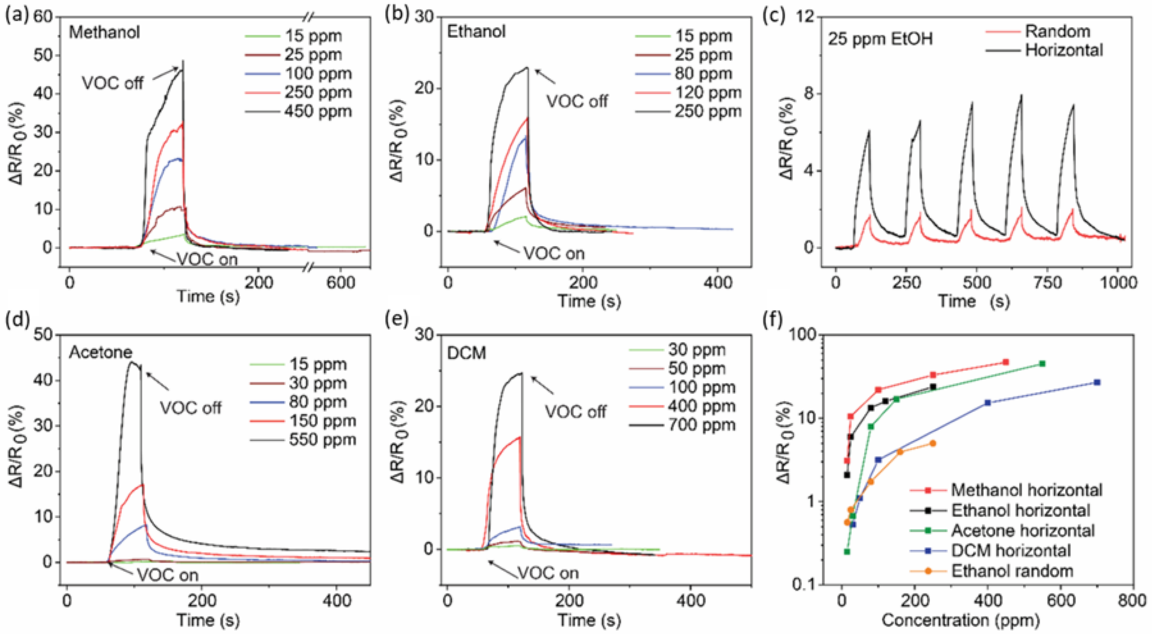

Figure 7. Changes in resistance of chemical sensors demonstrated the high sensitivity due to exposure to volatile organic chemicals (VOCs) of low concentrations for (a) methanol, (b) ethanol, (d) acetone, and (e) dichloromethane (DCM). (c) Different responses of random and horizontal nanoparticles to ethanol at 25 ppm. (f) High selectivity of horizontal patterns to different VOCs.

The sensor shows detectable resistivity change to the above-mentioned VOC molecules with fast response time (<10s), good reversibility, and high selectivity even for a low concentration of 15 ppm. The rapid response of CNF bundles to the vapors (seconds) is most likely caused by the direct adsorption of gas analytes, which results in direct charge transfer between an individual CNF and a donor- or acceptor-type molecule, leading to intra-nanotube modulation of the CNF's Fermi level.[103] Additionally, inter-tube electron hopping is influenced by analyte molecules and the dipole interaction mechanism based on the molecular binding of active sites, which is the main VOC-sensing mechanism for carbon-based nanomaterials.[104] The sensors with horizontal and random nanoparticle alignment also exhibited distinct responses at all VOC concentrations. In sum, we achieved the fabrication of a CNF-based chemiresistive sensor with high sensitivity and selectivity for different gases at low concentrations.

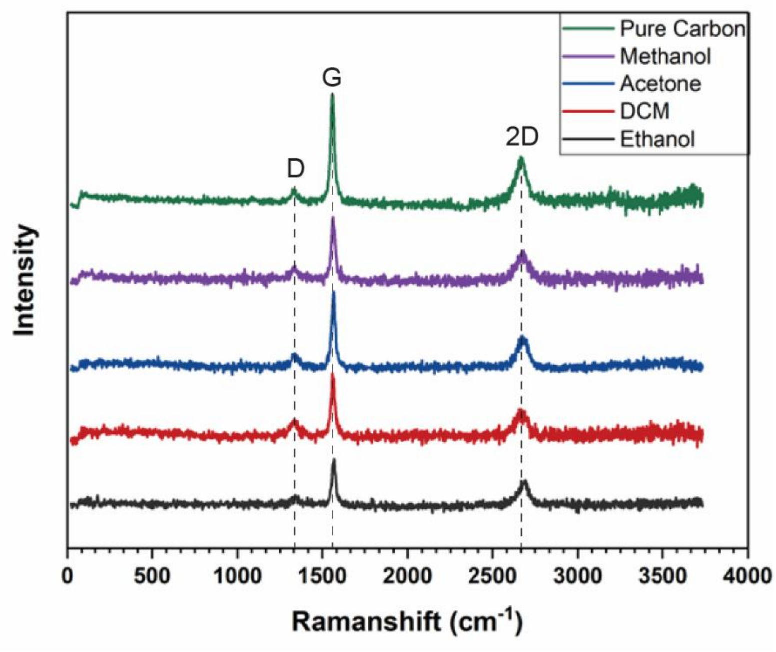

Figure 8. Raman spectra of pure CNF and CNF after being immersed in VOC.

2.4 Conclusion

In this chapter, by combining the SLA-based 3D printing technique and the dip-coating method, a scalable manufacturing process is investigated for controllable nanoparticle patterning and selective self-assembling of one-dimensional nanoparticles (i.e., CNF). Specifically, this technique employs the triangular surface features formed by 3D printing of the substrate for the layer-by-layer deposition of nanoparticles dependent on the dipping methodology, suspension quality, and nanoparticle-substrate interactions. The self-aligned

CNF-based substrates show promising performances regarding directional electrical conductivity, small strain piezoresistivity, and low concentration VOC sensitivities, making them suitable for microelectronics and multi-functional sensors. Together, the fast electron transport along the direction of particle alignment and the trapping of VOCs in micro-features for both horizontally and vertically dipped substrates enhanced the sensing response of the CNF-epoxy sensor. The high sensitivity, low theoretical limit of detection (sub-ppm), high signal-to-noise ratio (in thousands), fast response (<30 sec) and recovery (<10 min), and wide sensing range (tens to hundreds of ppm) at room temperature without any assistance are the main features of CNF-epoxy sensor. Ultimately, this 3D printing/dip-coating technique exhibits high potential for manufacturing repeatability, robustness, ease of production, and application in cost-efficient electronic and sensing devices.

REFERENCES

[72] H. Lin, L. Li, J. Ren, Z. Cai, L. Qiu, Z. Yang, H. Peng, *Sci Rep* **2013**, *3*, 1353.

[73] M. A. Meitl, Y. Zhou, A. Gaur, S. Jeon, M. L. Usrey, M. S. Strano, J. A. Rogers, *Nano Lett.* **2004**, *4*, 1643.

[74] Y. Joo, J. Byun, N. Seong, J. Ha, H. Kim, S. Kim, T. Kim, H. Im, D. Kim, Y. Hong, *Nanoscale* **2015**, *7*, 6208.

[75] R. Tietze, J. Zaloga, H. Unterweger, S. Lyer, R. P. Friedrich, C. Janko, M. Pöttler, S. Dürr, C. Alexiou, *Biochemical and Biophysical Research Communications* **2015**, *468*, 463.

[76] Yongtao Yang, Yun Chen, Fan Leng, Li Huang, Zijian Wang, Weiqun Tian, *Applied Sciences* **2017**, *7*, 1215.

[77] X. Zhao, C. Zhou, Y. Lvov, M. Liu, *Small* **2019**, *15*, 1900357.

[78] J. P. Lewicki, J. N. Rodriguez, C. Zhu, M. A. Worsley, A. S. Wu, Y. Kanarska, J. D. Horn, E. B. Duoss, J. M. Ortega, W. Elmer, R. Hensleigh, R. A. Fellini, M. J. King, *Sci Rep* **2017**, *7*, 43401.

[79] S. Wu, S. Peng, C. Wang, *Polymers* **2018**, *10*, 542.

[80] B. Su, Y. Wu, L. Jiang, *Chem. Soc. Rev.* **2012**, *41*, 7832.

[81] X. Zhang, J. Xie, F. Shi, D. Lin, Y. Liu, W. Liu, A. Pei, Y. Gong, H. Wang, K. Liu, Y. Xiang, Y. Cui, *Nano Lett.* **2018**, *18*, 3829.

[82] H. Li, B. C.-K. Tee, J. J. Cha, Y. Cui, J. W. Chung, S. Y. Lee, Z. Bao, *J. Am. Chem. Soc.* **2012**, *134*, 2760.

[83] W. Liu, S. W. Lee, D. Lin, F. Shi, S. Wang, A. D. Sendek, Y. Cui, *Nat Energy* **2017**, *2*, 17035.

[84] P. C. Millett, *The Journal of Chemical Physics* **2014**, *140*, 144903.

[85] J. J. Martin, B. E. Fiore, R. M. Erb, *Nat Commun* **2015**, *6*, 8641.

[86] H. Xin, A. T. Woolley, *Nano Lett.* **2004**, *4*, 1481.

[87] K. Thorkelsson, P. Bai, T. Xu, *Nano Today* **2015**, *10*, 48.

[88] M. Grzelczak, J. Vermant, E. M. Furst, L. M. Liz-Marzán, *ACS Nano* **2010**, *4*, 3591.

[89] Q. Liu, Y. Cui, D. Gardner, X. Li, S. He, I. I. Smalyukh, *Nano Lett.* **2010**, *10*, 1347.

[90] H. Yoshida, K. Kawamoto, H. Kubo, T. Tsuda, A. Fujii, S. Kuwabata, M. Ozaki, *Adv. Mater.* **2010**, *22*, 622.

[91] Y. Yang, X. Song, X. Li, Z. Chen, C. Zhou, Q. Zhou, Y. Chen, *Adv. Mater.* **2018**, *30*, 1706539.

[92] M. A. S. R. Saadi, A. Maguire, N. T. Pottackal, M. S. H. Thakur, M. Md. Ikram, A. J. Hart, P. M. Ajayan, M. M. Rahman, *Advanced Materials* **2022**, *34*, 2108855.

[93] Y. Yang, Z. Chen, X. Song, Z. Zhang, J. Zhang, K. K. Shung, Q. Zhou, Y. Chen, *Adv. Mater.* **2017**, *29*, 1605750.

[94] R. R. Collino, T. R. Ray, R. C. Fleming, J. D. Cornell, B. G. Compton, M. R. Begley, *Extreme Mechanics Letters* **2016**, *8*, 96.

[95] T. M. Llewellyn-Jones, B. W. Drinkwater, R. S. Trask, *Smart Mater. Struct.* **2016**, *25*, 02LT01.

[96] H. Lee, B. Seong, J. Kim, Y. Jang, D. Byun, *Small* **2014**, *10*, 3918.

[97] D. Friedmann, A. F. Lee, K. Wilson, R. Jalili, R. A. Caruso, *J. Mater. Chem. A* **2019**, *7*, 10858.

[98] J. Huang, F. Kim, A. R. Tao, S. Connor, P. Yang, *Nature Mater* **2005**, *4*, 896.

[99] P. Maury, M. Escalante, D. N. Reinhoudt, J. Huskens, *Adv. Mater.* **2005**, *17*, 2718.

[100] R. Jafari, C. Cloutier, A. Allahdini, G. Momen, *Int J Adv Manuf Technol* **2019**, *103*, 1225.

[101] N. K. Mandsberg, O. Hansen, R. Taboryski, *Sci Rep* **2017**, *7*, 12794.

[102] M. Cavallaro, L. Botto, E. P. Lewandowski, M. Wang, K. J. Stebe, *Proceedings of the National Academy of Sciences* **2011**, *108*, 20923.

[103] M. Abkarian, J. Nunes, H. A. Stone, *J. Am. Chem. Soc.* **2004**, *126*, 5978.

CHAPTER 3

ALIGNED $TI_3C_2T_X$ MXENE FOR 3D MICROPATTERNING VIA ADDITIVE MANUFACTURING

Abstract: Selective deposition and preferential alignment of 2D nanoparticles on complex and flexible 3D substrates can tune material properties and enrich structural versatility for broad applications in wearable health monitoring, soft robotics, and human-machine interface. However, achieving precise and scalable control of the morphology of layer-structured nanomaterials is challenging, especially constructing hierarchical architectures consistent from nanoscale alignment to microscale patterning to complex macroscale landscapes. This work demonstrated a scalable and straightforward hybrid 3D printing method for orientational alignment and positional patterning of 2D MXene nanoparticles. This process involved (i) surface topology design via μCLIP and (ii) directed assembly of MXene flakes via capillarity-driven DIW. With well-managed surface patterning geometry and printing ink quality control, the surface microchannels constrained MXene suspensions and leveraged micro forces to facilitate preferential alignment of MXene sheets via layer-by-layer additive depositions. The printed devices displayed multifunctional properties, i.e., anisotropic conductivity and piezoresistive sensing with a wide sensing range, high sensitivity, fast response time, and mechanical durability. Our fabrication technique shows enormous potential for rapid, digital, scalable, and low-cost manufacturing of hierarchical structures, especially for micropatterning and aligning 2D nanoparticles not easily accessible through conventional processing methods.

3.1 Introduction

In chapter 2, the SLA 3D printing for template manufacturing and dip coating for nanoparticles organization was studied for 1D nanoparticles (i.e., CNFs), resulting in anisotropic patterning and alignment of CNFs. Chapter 3 implements a similar dispersion-mediated template-based NP assembly approach consisting of μCLIP for template 3D printing and microfluidics for self-assembly of 2D MXene nanoparticles on the patterned surface with improved microscale patterning resolution and nanoscale stacking.

Nanoparticles achieve their full potential only when assembled as continuous lines, stacked in multilayers or van der Waals heterostructures that are significantly valuable for microelectronics, energy storage, optoelectronics, sensors, and catalysis.[105,106] However, it is difficult for most nano-processing methods to effectively manipulate nanoparticles on a nanoscale size to achieve manufacturing scalability and production repeatability. For example, conventional nanomanufacturing uses nanomaterials as building blocks for constructing complex microstructures, including chemical vapor deposition (CVD), self-assembly, coating, UV lithography, and stamping.[107–110] Nonetheless, CVD is notorious for its slow deposition and the surface patterning requires the delicate design of catalysis. Self-assembly uses mainly nanoparticles of spherical shapes or rigid wires due to their symmetry and easy control of crystallography. Molecular-thick patterning mandates tedious surface functionalization. Coating techniques are simple but limited to a planar and particulate substrate. Besides, the cross-substrate deposition in the coating is not selective and cannot differentiate nanoparticles from their mixtures (*e.g.*, polymers) due to their rheology requirements.

3D printing technology, as a layer-by-layer additive manufacturing, is of considerable interest due to its flexibility in terms of rapid prototyping, complex designing, material choices, and minimized waste for sustainability. 3D printing-based assembly and patterning techniques are divided into digital printing (*e.g.*, direct inkjet, fused deposition modeling (FDM), stereolithography (SLA)), and nondigital printing (*i.e.*, screen, transfer printing). So far, direct inkjet, screen printing, FDM, and SLA 3D printing are used primarily for nanoparticle patterning and assembly, but these techniques suffer technical difficulties.[111] For inkjet printing, the formulation of printable ink with suitable rheological and fluidic properties is problematic since clogging will greatly slow down manufacturing speed. For screen printing of highly viscous inks, the main drawbacks are low resolutions and high surface roughness. In FDM, the high-volume requirement of printable feedstock and the limited choice of printing materials (*i.e.*, filaments) are the main barriers. SLA 3D printing works in combination with external forces (*i.e.*, shear, electric, magnetic, and acoustic field) to build reinforced composites with aligned fillers.[53,112] The externally-coupled electrophoresis and magnetophoresis can locally design nanoparticle orientation but have limitations of low nanoparticle concentrations (<20 vol%), slow printing speed (*i.e.*, mostly stereolithography), and a lack of depositional selectivity. Besides, none of these 3D printing techniques can achieve nanoscale feature control (*e.g.*, at best tens of microns) and have acceptable scalability up to only micro or macrostructures.

Moreover, 1D nanotubes or 0D nanospheres are nanomaterials used in conventional and 3D printing-based nanomanufacturing methods for morphology and hierarchy management. 2D nanomaterials with planar surfaces are thermodynamically nonstable and have a high intention to form clusters composed of rippled sheets without long-range orders. Therefore, scalable nanomanufacturing of 2D materials (*e.g.*, layers, platelets, stacks, chips) is the most challenging task. Compared to other 2D nanoparticles (*e.g.*, graphene or boron nitride platelets), MXene possesses a unique set of properties, including customizable dimensions, tunable surface charges, and excellent dispersity suitable for assembling hierarchical architectures.[113] The surface-rich hydrogen groups render hydrophilicity and excellent dispersity in colloidal inks, making MXene flakes the conductive ceramics, ideal candidates for wet-processable assembling and patterning applications.[114]

In this chapter, we describe a versatile approach for fabricating high-resolution micropatterns with parallelly deposited and anisotropically aligned MXene flakes on 3D printed flexible substrates. The advanced μCLIP 3D printing technique was used to produce substrates with microscopic topographical features on which the MXene ink was directly and selectively deposited *via* DIW. The multilayered MXene film was formed in a layer-by-layer fashion through flowing, confining, and stacking MXene ink into surface microchannels *via* capillary action. The MXene ink gets dragged onto the substrate surface, experiencing long-range and short-range forces, facilitating positional and orientational alignment of MXene flakes. In addition to a well-aligned assembly, the high-resolution and high-aspect-ratio patterning of MXene over a macroscale area is essential for tuning the composite structures' functional properties. This technique enabled anisotropic micropatterning and ordered assembly with face-to-face and edge-to-edge contact between 2D flakes on complex 3D printed substrates. Our hybrid 3D printing shows enormous potential for fast, scalable, large-volume, and low-cost patterning and assembly of general nanoparticles for broad applications with manufacturability and device functionality demonstrations.

3.2 Experimentation and Characterization

3.2.1 MXene Synthesis and Dispersion Preparation

The MAX powders are made by mixing TiC (Alfa Aesar, 99.5%, 2 mm), Al (Alfa Aesar, 99.5%, -325 mesh), and Ti (Alfa Aesar, 99.5%, -325 mesh) powders in the molar ratio of 2:1.1:1. The mixed powder was heated under the flow of Ar filled alumina tube furnace at 1350°C for 2 hr followed by furnace cooling at the rate of 5°C/min. The resulting loosely sintered powders were ground using gritstone. The milled powders were passed through a 400-mesh sieve to obtain fine powders of 38 μm particle size. The fabricated MAX powder was subjected to different experimental steps to manufacture the 2D MXene flakes (Figure 9). 2 gm of LiF powder was dissolved in 20 ml 9M HCl solution. The solution was stirred for 10 min up to LiF salt completely dissolve in the acidic solution. Then, 2 gm of MAX was slowly added to the etchant mixture (*i.e.*, HCl + LiF) to avoid a violent exothermic reaction. The mixture was stirred continuously at 500 rpm for 24 hr at 35°C. After etching was complete, the exfoliated mixture was repeatedly washed with DI water *via* centrifugation (3500 rpm 10 mins for each cycle) until the pH of the supernatant reached about 6. The sediment slurry was dispersed in deaerated water and delaminated by sonication under flowing Ar for 1 hr, followed by centrifugation at 3500 rpm for 1 hr. The stable MXene colloidal solution (supernatant) was collected, and vacuum filtered through a PVDF membrane. MXene nanoparticles were suspended in ethanol to form varying suspension concentrations (*i.e.*, 10, 20, and 50 mg/ml), out of which 10 and 20 mg/ml showed excellent stability, whereas 50 mg/ml showed sedimentation after ≈24 hr because the stronger nanoparticle interactions lead to the formation of agglomerates.

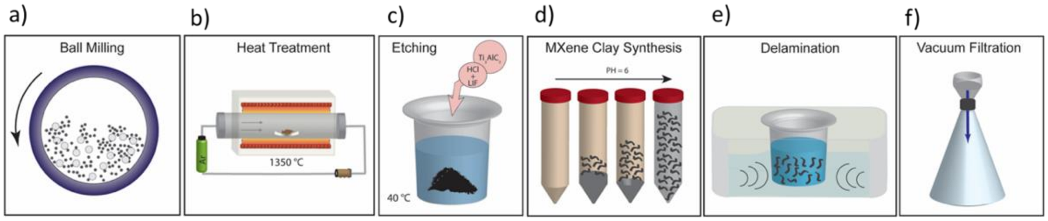

Figure 9. Experimental steps required for MXene flake synthesis: a) ball milling, b) vacuum heat treatment, c) chemical etching, d) washing, e) sonication, and f) filtration.

3.2.2 Micro-continuous Liquid Interface Projection 3D Printing

3D printed substrates with a micro grating of dimension 100 μm width, height, and spacing were manufactured through the μCLIP technique. The Poly(ethylene glycol) diacrylate (PEGDA, average M_n 700, Sigma - Aldrich) resin was mixed with photoinitiator Phenylbis(2,4,6-trimethylbenzoyl)phosphine oxide (Irgacure 819, 97%, Sigma – Aldrich, 2 wt%) and photo absorber 2-(2H-Benzotriazol-2-yl)-6-dodecyl-4-methylphenol (Tinuvin 171, Sigma – Aldrich, 0.2 wt%). The μCLIP uses a Wintech Pro4500 light engine comprising a 385 nm light source as well as a Digital Mirror Device (DMD) consisting of 912 x 1140 pixels to generate the designed patterns. The CAD model was sliced into a sequence of 2D patterns with specific thicknesses along the *Z*-direction, which were then sequentially projected by the light engine. A UV lens (UV8040BK2, Universe Optics) was used to focus the projected patterns onto the printing platform with a CMOS (MU2003-BI, AmScope) used to monitor the focusing status of projected patterns. A Z-axis motorized stage (X-LSM200A-KX13A, Zaber) was used to generate the continuous movement of the printing stage with controlled speeds, an oxygen-permeable thin film (Teflon AF2400, 70 μm nominal thickness) was embedded in a customized resin bath, into which resin was dispensed and sequentially solidified upon the projected patterns. Printed samples were thoroughly cleaned with IPA and blow-dried with clean, dry air.

3.2.3 Layer-by-Layer MXene Assembly via Direct Ink Writing of Low-Viscosity Colloids

The stable dispersion of MXene/ethanol having 10, 20, and 50 mg/ml concentrations was prepared by dispersing dried MXene powders into ethanol *via* sonication for 15 minutes. A solution of 3 μL of each concentration was deposited into the reservoir on the substrate patterns by a DIW syringe. The dispersion gets sucked into the microchannels *via* the capillary action followed by ethanol evaporation at RT (*i.e.*, total time ≈2 sec for the deposition and drying over a length of 10 mm microchannel). After evaporation, the monolayer of self-assembled MXene flakes is formed on the inner surface of microchannels. After drying of the previous MXene layer, an additive droplet is applied *via* the same process and the effect of several layer deposition <n> on the morphology and electrical properties was investigated. After the deposition, the substrates were kept in a vacuum desiccator until use.

3.2.4 Rheology Measurements

The rheology test of MXene dispersion was conducted using TA instruments (Discovery HR2) rheometer with 40 mm 2° cone Peltier plate (amount ≈2 ml). The viscoelastic properties of the MXene dispersion were studied by measuring the viscosity, viscous, and elastic modulus of the sample as a function of frequency 0.1 to 100 Hz at a constant stress of 0.015 Pa at RT.

3.2.5 Material Characterizations

The SEM images and EDS mapping were taken by vacuum field emission scanning electron microscope with XL 30 at an accelerated voltage of 10kV. Samples were coated with Au-Pd for 80 sec to improve conductivity. AFM images were captured by Witech Alpha 300 RA. XRD spectra were obtained from a PAN analytical X'Pert PRO powder diffractometer in the range of 5–70° (2θ). The interlayer spacing of multilayered MXene was calculated according to the following brags law equation (Equation 1).

$$d = \frac{n\lambda}{2 \sin \theta} \qquad \text{Equation 1}$$

Here, λ is the wavelength of the X-ray source is 1.54 Angstrom, and θ is the scattering angle of (002) peak. The thickness of the MXene film was obtained from the cross-sectional SEM images and measured by ImageJ software by averaging values at 10 different sites. The optical image, 3D surface imaging, and film surface roughness of the substrate/MXene film were taken from the Keyence optical scanning microscope.

3.3 Results and Discussion

3.3.1 MXene Synthesis and Characteristics Properties

The Ti_3AlC_2 powder prepared *via* a ball milling and heat treatment procedure was used as a MAX precursor (Figure 10a) for the preparation of MXene flakes that can be seen as compact layers stacked by individual 2D MXene. The selective etching of Al layers from Ti_3AlC_2 showed a multilayered accordion-like structure (Figure 10b). The successful exfoliation of single/multilayered MXene flakes (Figure 10c) was formed through washing and sonication. After the etching of Al, the filtered MXene film contained a terminal surface of oxygen and fluorine, which is shown in EDS mapping (Figure 10d). The cross-sectional view also showed individual $Ti_3C_2T_x$ flakes and uniform distribution of Ti, Al, O, C, and F on the MXene flake surfaces. Figure 10e shows XRD patterns of the parent Ti_3AlC_2 MAX phase and $Ti_3C_2T_x$ nanosheets. The successful delamination of $Ti_3C_2T_x$ MXene was reflected by the shift in typical (002) diffraction peak for 2θ from 9.58° to 6.45° due to increased interlayer spacing from Angstrom to nm, accompanied by the disappearance of (101), (104), (103), and (105) crystalline peaks. AFM image shows pristine MXene flake with a lateral dimension of around ≈2.5 μm (Figure 10f). The MXene nanosheets in the aqueous suspension exhibited good stability due to the polar and hydrophilic functional groups (-O, -OH, -F) on its surface, which was demonstrated by the Tyndall effect (Figure 10g).[115] For the deposition of nanoflakes, $Ti_3C_2T_x$ ink was made of predominantly single flakes with a thickness of ≈6 nm and the mean lateral dimension is ≈2.5 μm (Figure 10h).

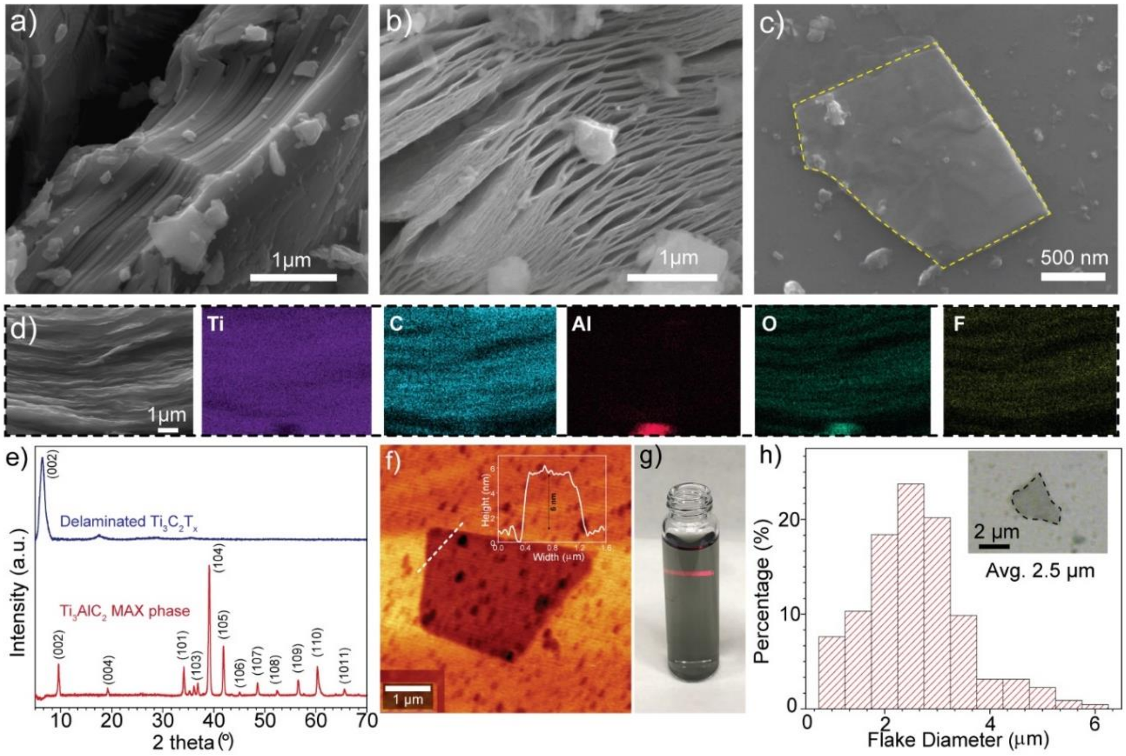

Figure 10. Characteristic of MXene nanosheets. SEM imaging of a) the stacked MAX phase, b) delaminated MXene nanoparticles, c) a single flake MXene, d) EDS images of MXene film after filtration, e) XRD patterns of MAX and MXene, f) AFM image of an individual MXene nanosheet, g) Tyndall effect showing uniform dispersion quality, and h) MXene nanoparticle size distribution.

3.3.2 μCLIP for 3D Printed Surface Patterns

Figure 11 illustrates our printing procedure design for nanoscale deposition of 2D nanoparticles (*i.e.*, MXene layers) and microscale stacking with closely packed orders. To achieve desirable MXene deposition sites, we printed surface patterns to regulate nanoparticle localization. The patterned substrate was printed *via* the μCLIP method (Figure 11a), which utilized an oxygen-permeable window between photosensitive resins and printing platforms as the 'dead zone' for continuous resin deposition.[116] PEGDA was used as a photosensitive hydrogel along with photo absorbers and photoinitiators, displaying the hydrophilic surface tension required for MXene deposition. The SEM micrograph in Figure 11b shows the 3D printed substrates' surface topography with fixed cross-section dimensions (i.e., a height and bottom gap of ~100 μm, and a top gap of ~200 μm). μCLIP 3D printing method enabled faster manufacturing and layer-less microstructures with lower surface roughness than general vat polymerization-based 3D printing. In this way, the subsequently dropped inks would not form turbulent flows that might disrupt ordered nanoparticle morphologies. The desirable nanoparticle orders will be preferentially positional with orientational alignment along specific printing paths and well-manipulated stacking density or packing factor.

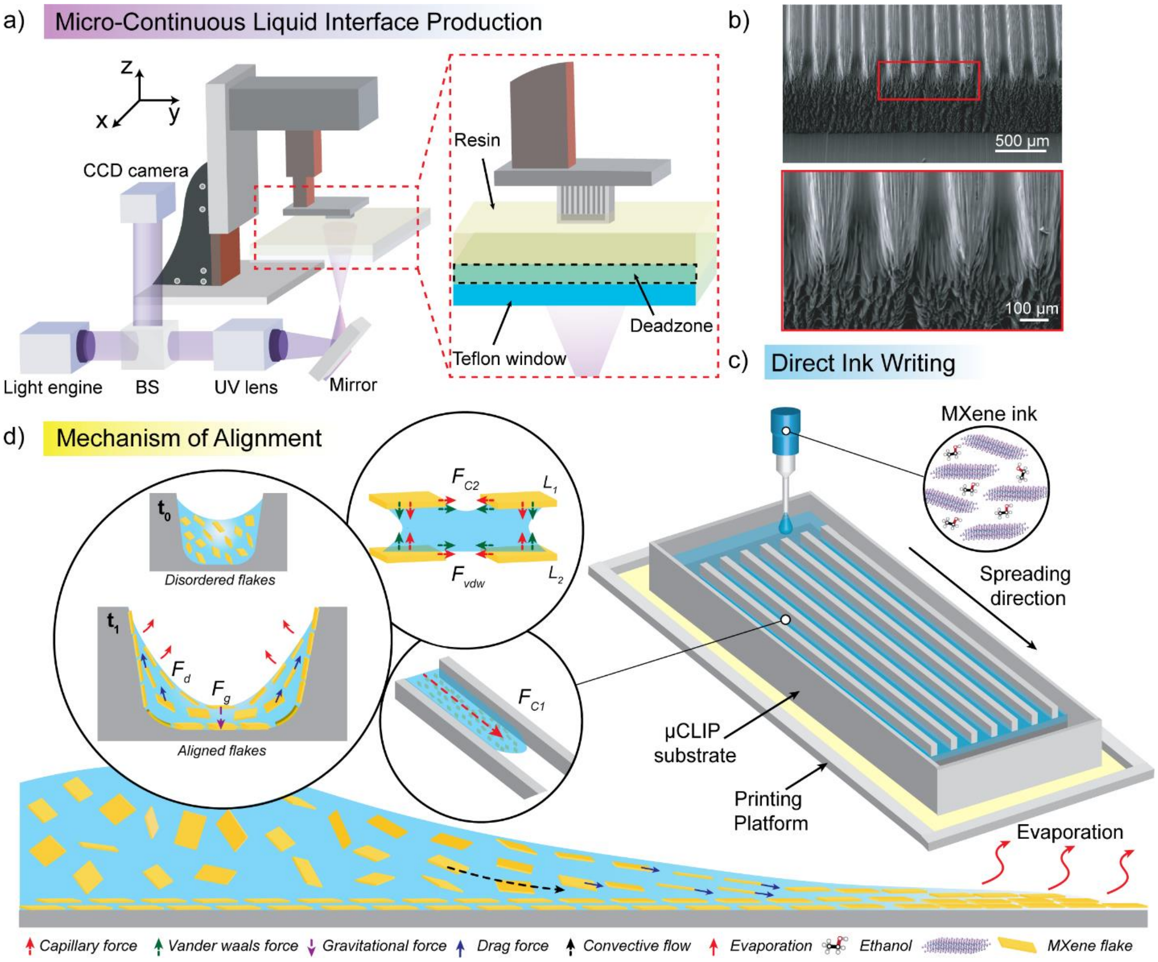

Figure 11. Schematic of the hybrid 3D printing combining (a) the surface patterning via μCLIP (CCD: Charge-coupled device, BS: Birefringence system, UV: Ultraviolet) with the (b) surface topography of micro features like microchannels and reservoir on the substrate and (c) DIW of MXene/ethanol ink for directed MXene assembly with anisotropic deposition and preferential alignment. (d) Schematic for the alignment mechanism with micro force balances between the shear from the ink flow (F_{c1}), gravity (F_g), drag force (F_d), capillarity (F_{c2}), and van der Waals (F_{vdw}) between adjacent layers (L_n).

3.3.3 Theoretical Framework for the Capillary-Driven 2D MXene Assembly

The MXene assembly followed two-step dynamic processes. The initial step was the capillary-driven MXene patterning along surface microchannels, and the second procedure involved the evaporation thermodynamics-regulated nanoparticle assembly for orientational hierarchies.

The capillary effect is a liquid's capability to flow in a narrow channel due to intermolecular forces and surface tension between the liquid and surrounding surfaces, propelling the flow against viscous and/or gravitational forces. Here, the MXene/ethanol suspension droplets immediately spread into the microchannels (*i.e.*, a flow rate of 10 mm/s) within a channel at the size scale of ~100-200 µm (Figure 11c). The surface tension for the PEGDA substrate and ethanol is 36.66 and 21.55 mJ/m^2, respectively, promoting a better spreading of MXene/ethanol than with the MXene/water suspension ($\gamma_{water} = 72.8$ mJ/m^2).[117,118] According to Jurin's law (Equation 2) and an observation of a wetting angle (*i.e.*, 18°, Figure 12), the capillary force (F_{c1}) was a few orders of magnitude higher than gravity, validating its dominant role in driving the liquid flow and MXene dispersions along surface-patterned microchannels.[119]

$$p_c = 2\gamma\cos\theta/r_c \qquad \text{Equation 2}$$

Here p_c is the capillary pressure, γ is the liquid-air surface tension, θ is the wetting angle of the liquid on the surface of the capillary, and r_c is the interface radius. Also, the Reynolds number for the suspension fluids is as small as ~0.078 (Equation 3), representing a laminar flow within the channel.[120] This laminar flow is critical in forming orientation-aligned particle morphologies, a phenomenon reported in different particle systems.[121,122]

$$Re = \rho vL/\mu \qquad \text{Equation 3}$$

Here, Re is the Reynolds number, ρ is the density of suspension fluids, v is the velocity of the fluid, L is the characteristic length, and μ is the fluid's viscosity. The low Re (Re <<1) of fluid implies a laminar Stoke's flow in microchannels enabling uniform dispersion of MXene. Followed this dispersion, the evaporation thermodynamics would lead to organized stacking and close packing of 2D layers.

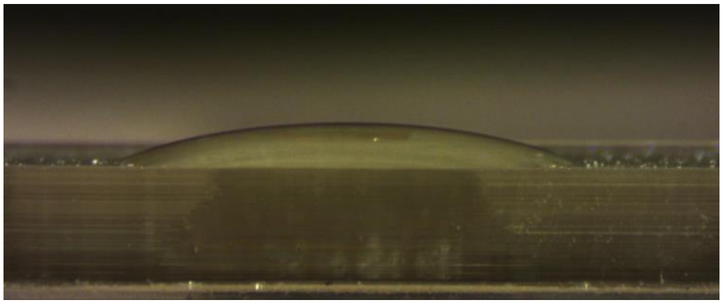

Figure 12. The contact angle between PEGDA flat substrate and ethanol is ~18°, showing good wetting properties.

Directed nanoparticle assembly *via* evaporation thermodynamics-based deposition on the patterned substrate is a complex phenomenon combining short-range and long-range driving forces (Figure 11d).[123] The micromechanics analysis considering all micro forces, including gravity (F_g), drag force (F_d), van der Waals force (F_{vdW}), and capillary forces (F_{c1} & F_{c2}) were studied. The F_{c1}, F_g, and F_d are universally long-range, disregarding the nanoparticle positions or relative spacing. The F_{vdW} and F_{c2} are short-range attractions, with the typical working spacing of nanometers among MXene. The capillary force here for attracting the nanoparticles together (F_{c2}) is different from the capillarity driving the liquid into the microchannels (F_{c1}) mentioned before. The convective flow of the liquid *via* capillary action confines the droplet between the microchannels. The MXene suspension was pinned at the edge of the channels and formed a "U" shape substrate-solvent-air triple contact line that moves down the horizontal channel by externally applied convective force (Figure 11d). The constant solvent evaporation from the substrate-solvent-air interface drives the MXene from the liquid body to the meniscus front *via* convection.[124] Nanoparticles experience a drag force (F_d) consistent during the suspension transport from the droplet reservoir to the microchannel and the colloidal diffusion from the microchannel interior towards the meniscus during evaporation. The nanoparticles closest to the solvent-air interface orient with the primary axis parallel to the contact line experiencing downward gravitational force (F_g), leading to layer-by-layer sedimentation.[102] Once long-range order forces bring nanoparticles to proximity, F_{vdW} (*i.e.*, a weak attraction force between particles) and F_{c2} (*i.e.*, Laplace pressure difference generated due to curved meniscus between the adjacent particles) facilitate the in-plane and out-of-plane MXene assembly along the microchannel bottoms and walls, respectively (Figure 11d).[123]-[125] Micro forces and the local confinement by the micro-channeled substrate are responsible for mesoscale nanoparticle hierarchies.

3.3.4 Rheological Characterization of MXene Printing Inks

Achieving stable dispersion quality with nanoparticle homogeneity and controlled rheological properties plays a critical role in the uniform deposition of MXene films. MXene nanoparticles were suspended in ethanol (Figure 13a). Figure 13b shows the measured viscosity as a function of shear rates (*i.e.*, MXene/ethanol of 10, 20, and 50 mg/ml). The viscosity increased as a function of MXene/ethanol concentration. The viscosity-shear rate plots showed a non-Newtonian and shear-thinning (pseudoplastic) behavior for MXene/ethanol suspensions of 20 and 50 mg/ml, ideal for most 3D printing techniques due to the facilitation of flow through thin-diameter printing nozzles. Extreme high and low viscosity values should be prohibited due to the following reasons. (i) Highly viscous printing materials would clog the print head and cause manufacturing inconsistency, and (ii) low viscosity feedstock would behave as liquids and cannot retain their dimensional features upon exiting the printhead, leading to reduced printing resolutions or structural collapse. However, we leveraged the surface patterning in this study to constrain the liquid transport across the channel-normal directions. Therefore, the 10 mg/ml MXene/ethanol showing Newtonian flow behavior would also work for our printing systems due to the MXene confinement within the 3D printed microchannels, providing the extra benefit of more precise control of assembly thickness.

The magnitude of viscoelastic properties provides valuable information on the processing, fabrication, and integration of MXene into complex architectures. The elastic (G') and viscous (G") moduli of the MXene dispersion have been determined as a function of frequency (rad/s) at fixed stress 0.015 Pa (Figure 13c). For dilute concentrations 10 and 20 mg/ml, the dominance of G" over G' had a direct impact on ink processability. For example, the MXene dispersion was suitable for high-rate processing methods where it was required to spread this colloid on the substrate surface on contact.[126] The presence of G' for such low concentrations enabled the processing of a very dilute $Ti_3C_2T_x$ solution that facilitated fabricating a nanometer-thick MXene thin film with ease.[127] On the other hand, for 50 mg/ml, G' is higher than G", suggesting particle crowding that exhibits gel-like behavior of the material system as a result of increased nanoparticle interactions. This more elastic than viscous ink is more suitable for use in filamentary extrusion-based 3D printing (instead of our ink writing) due to its shape-retention that may cause voids in our confined microchannel geometry. Thus, we will demonstrate in our hybrid 3D printing the use of low-concentration inks for their deposition selectivity, flowability, and nano manufacturability for well-manipulated MXene layers.

This hybrid 3D printing combines DIW with μCLIP to achieve multi-material and multiscale additive manufacturing. The photograph of the setup (Figure 13d) shows this DIW/μCLIP integration to drop inks on patterned substrates with precise management of droplet sizes, sites, rates, and ink compositions. The μCLIP enabled the quick fabrication of substrate with micron-size features while DIW dispensed MXene inks on selective substrate sites, followed by the inks being transported into the microchannels *via* capillary action. The MXene/ethanol ink (*i.e.*, 10 mg/ml), with good flowability, was used to deposit MXene on substrate surface patterns consisting of various microchannel lengths (*i.e.*, 5, 10, 20, and 30 mm in Figure 13e_1). Our technique enables high-throughput deposition of MXene film using limited material quantities, as only a droplet is required to fill up microchannels (*i.e.*, 10 mm/s Figure 13e_2). The zoomed-in image shows the uniform deposition of MXene within microchannels (Figure 13e_3). Figure 13f shows successful region-specific deposition of multilayered MXene into intricate structures, including micro-supercapacitors, antennas, and other configurations that could not be achieved through dip-coating or vacuum-assisted filtration. The MXene assembly shows along-channel aligned morphology and stacked layers, separated by printed polymeric walls that prevent cross-contamination or short circuit of two electrodes during electrochemical applications (Figure 36). Our technique provides a versatile strategy for high-resolution and large-scale production of anisotropic MXene thin films with complex geometries compared to conventional nanoparticle assembly methods.

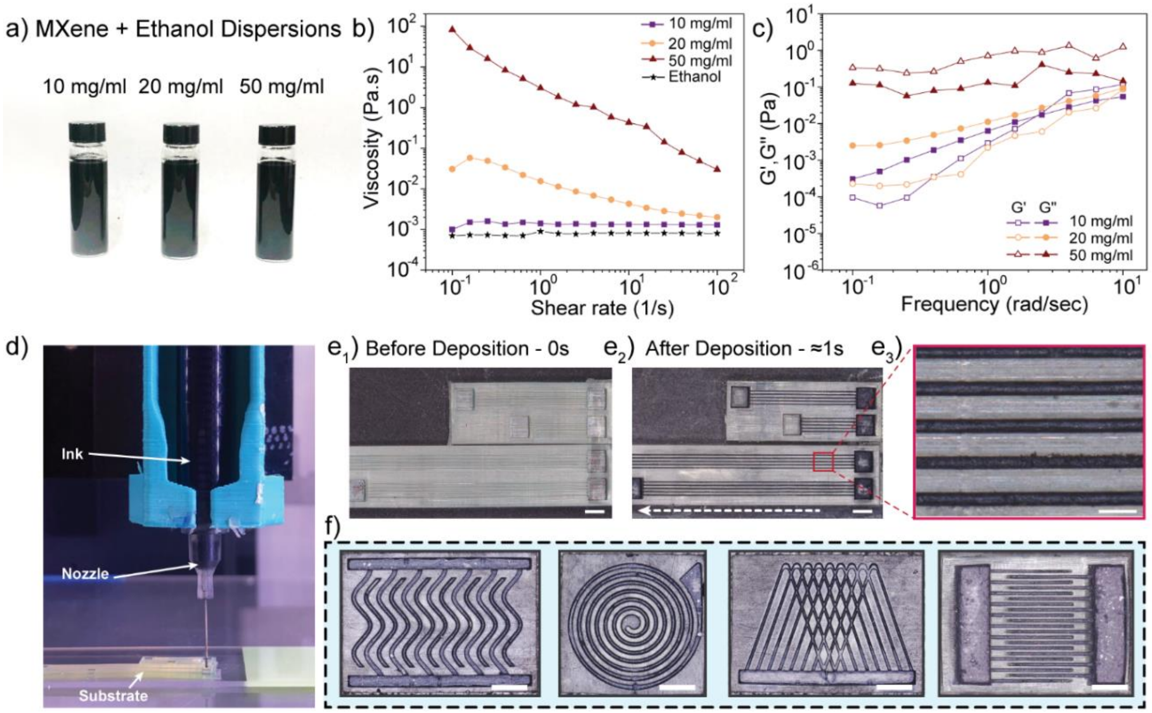

Figure 13. Rheological properties of $Ti_3C_2T_x$ with a) different dispersion concentrations, b) the viscosity as a function of shear rates, c) the storage modulus (G') and loss modulus (G") vs. frequency, d) a photograph showing the hybrid 3D printing approach with the DIW of droplets on the μCLIP-printed surface patterns, e) the optical images for the patterned surface of linear grooves e_1) before and e_2) after droplet deposition with e_3) a zoomed-in image showing homogeneous MXene distribution, f) optical images of complex surface patterning (from left to right – wavy grooves, antenna-shaped circles, cross-linked triangle channels, and interdigitated structure) (Scale bars are 2 mm in e_1 and e_2, 300 μm in e_3 and 1 mm in f).

Fluidic simulations were performed using ANSYS Fluent to theoretically verify the influences of capillary force, channel width, and concentration on nanoparticle distributions. The two-phase discrete model was used to describe the distribution of MXene particles into microchannels under capillary action. The analysis determined the particle concentration (mg/m^3), velocity (m/s), and residence time (s) for varied MXene/ethanol concentrations (*i.e.*, 10, 20, and 50 mg/ml) into 100x100 μm cross-section and 10 mm length microchannels Table 1. Figure 14a-c demonstrates that the pressure difference between the unfilled microchannel end and the filled droplet reservoir drives the MXene suspensions into the microchannels due to capillary force. As a result, the even distribution of particles into microchannels for the 10 mg/ml concentration was obtained within 1 s, which is consistent with the experimental observation. The increase in the concentration of solutions showed a rise in particle density and residence time while particle velocity was reduced. These simulations proved the capillarity effectiveness in driving inks and forming uniform particle distributions mandatory for desirable MXene morphologies and dimensions.

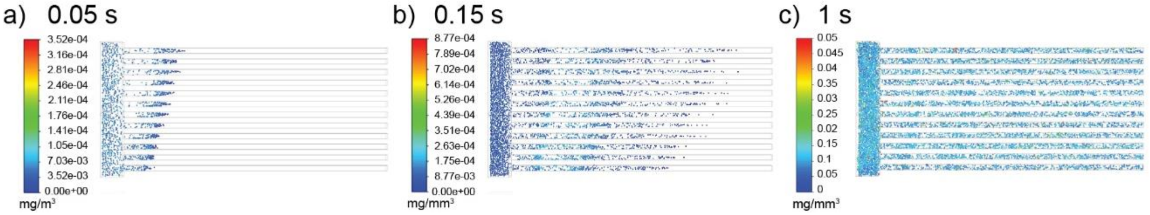

Figure 14. a-c) Simulated nanoparticle position field within microchannels showing the capillary driven MXene transport, scale bar represents the particle density distribution (mg/m^3).

Table 1. Average Values of Particle Properties a) Velocity, b) Density, and c) Residence Time Distributions at 25 sec for 10, 20, and 50 mg/ml Concentration of MXene Inks Obtained from ANSYS Fluent Simulation Studies.

Concentration (mg/ml)	Density (mg/mm^3)	Velocity (in channels) (mm/s)	Residence Time (s)
10	0.0129	16.1	0.090

20	0.031	14.5	0.121
50	0.053	14.3	0.163

3.3.5 Structural and Morphological Characteristics of Printed MXene Multilayers

After confirming the synthesized MXene quality and rheology appropriateness, we deposited the MXene suspensions with an individual droplet size of 3 μL onto the 3D printed substrate, leading to a layer-by-layer additive coating within the microchannels. The solution placed at the microchannel inlets (*i.e.*, reservoir) was immediately transported into the microchannels from the droplet reservoir *via* capillary action (Figure 15a). The subsequent evaporation of the solvent (*i.e.*, ethanol) induced the aligned assembly of nanoparticles, leading to the coverage of a thin MXene layer on the microchannel's inner surfaces containing well-aligned flakes. We studied the influences of (i) the number of ink droplets or additive layers <n> and (ii) ink concentrations on the microstructure and morphology of the multilayer coating. For 10 mg/ml, the optical micrographs show that with an increasing number of layers (*i.e.*, from 5 to 40), the coating width remained constant while the contrast was higher, indicating well-confined MXene assembly within microchannels and uniform deposition in additive manners (Figure 15a). With a droplet number of 40, the deposition of 10 mg/ml inks showed comparatively more uniform morphologies than 20 and 50 mg/ml inks, which was clear from the 3D surface mapping (*i.e.*, smooth surfaces along the microchannel for 10 mg/ml inks while irregular islands for 20 and 50 mg/ml inks, Figure 15b-d). For 10 mg/ml, the surface topography of MXene film deposited into microchannels showed continuous and uniform coating morphology. The higher interparticle interactions in concentrated dispersions (*i.e.*, 20 and 50 mg/ml) contributed to nanoparticle agglomerations and unpredictable island formation inside the microchannels.

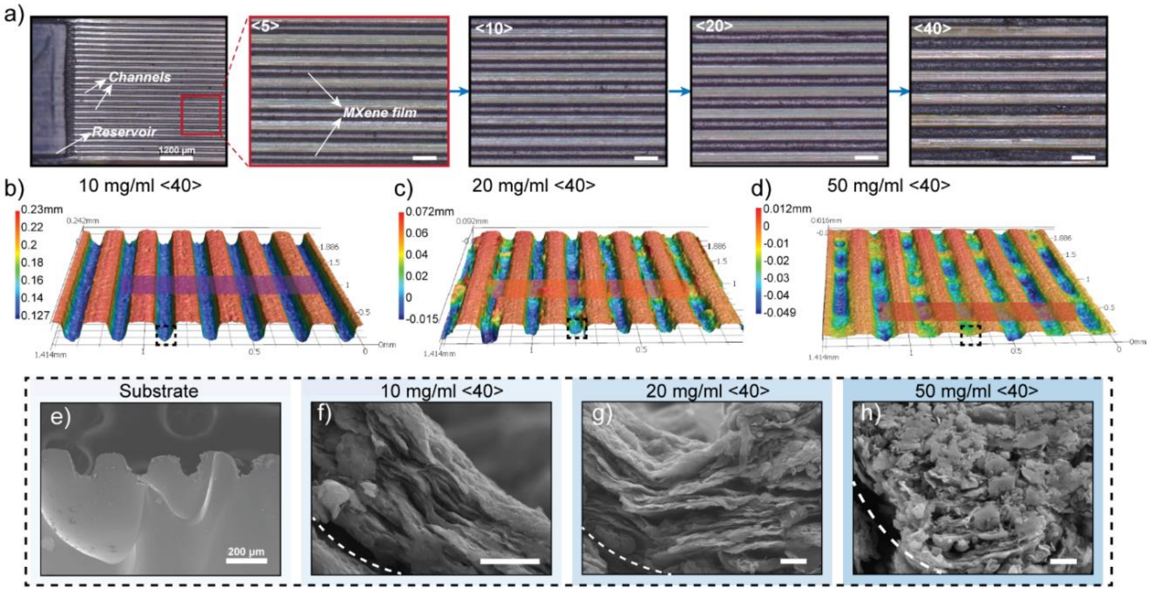

Figure 15. a) optical images showing top views of deposited MXene films on patterned substrates for different <n> (scale bar 300 μm), b-d) cross-sectional 3D optical profilometry images demonstrating the microchannel inner surface roughness at <40>, patterned surface e) before and f-h) after printing 40 layered MXene for f) 10 mg/ml <40>, g) 20 mg/ml <40>, h) 50 mg/ml <40> (scale bar 2 μm and dashed lines show the interface between the substrate and MXene film).

The cross-sectional SEM images of the substrate before and after the MXene printing are shown in Figure 15e-h. The patterned surface showed a grooved microchannel structure (*i.e.*, height and bottom gap of ~100 µm and top spacing of ~200 µm consistent with the surface patterning design) (Figure 15e). The zoomed-in SEM images indicated the two types of thin coating of MXene nanoparticles on the substrates (Figure 15f-h). 10 and 20 mg/ml showed a continuous and parallelly aligned film (Figure 15f-g). This layered structure was attributed to the favorable deposition of MXene sheets by driving them into microchannels with the shear-assisted flow, aligning them along the flow followed by sedimentation, and interconnecting with each other to form a continuous and effective network, even at lower MXene concentrations and viscosity.

However, for concentrated suspensions (*i.e.*, 50 mg/ml), the stacked MXene packing was absent, and the randomly packed MXene chunks were formed (Figure 15h). The random orientation of MXene sheets in 50 mg/ml was possibly due to the viscoelastic properties in the colloidal suspensions behaving with more solid viscoelasticity where the particle interactions and inertia prohibit "long-range" rearrangement. Additionally, in a highly concentrated solution, nucleation occurs from the bulk of the solution when the deposited films were thick to facilitate the in-plane alignment by capillary and drag forces. The height profile analysis of the MXene multilayers showed the film thickness variation, suggesting the abrupt MXene accumulation from 10 & 20 mg/ml to 50 mg/ml due to trapped voids and lower packing factor (Figure 16a).

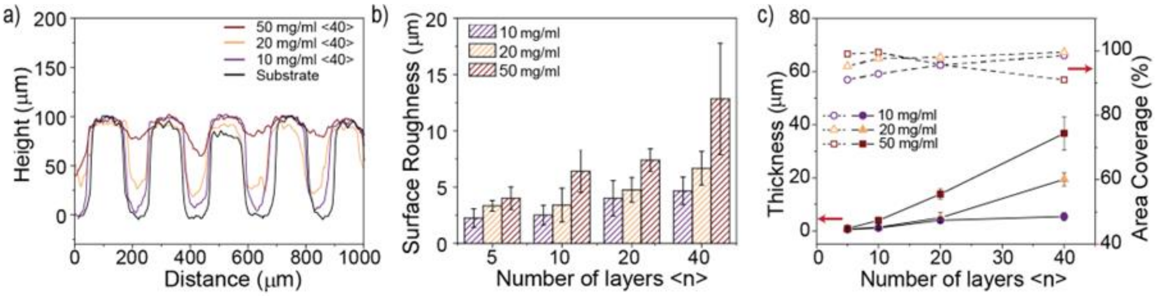

Figure 16. 3D optical profilometer-characterized a) height profile across micro channeled surface patterning, b) Surface roughness versus <n>, and c) thickness growth and area coverage of multilayered MXene with concentration-varied inks (i.e., 10, 20, and 50 mg/ml).

The obtaining of lower surface roughness and roughness variation is significant because it affects many physical properties of the assembled MXene thin film, including thermal dissipation, electrical conductivity, and optical reflectivity. The root mean square (RMS) surface roughness measured by using a profilometer increased as a function of layer numbers and concentrations (Figure 16b). For example, for 10 mg/ml, the surface roughness value of ≈2.2 and ≈4.7 μm was achieved for the <n> of 5 and 40, respectively (Figure 17). The multilayered film thickness increases with growing layer numbers and particle concentrations, with a higher consistency in lower MXene/ethanol concentrations (Figure 16c). A significant variation of film surface roughness in highly concentrated inks (*e.g.*, 50 mg/ml) was due to nanoparticle clustering and surface cracking that would disrupt the structural integrity and mechanical reliability. The residual stress generated in the film due to high surface roughness initiated microcrack formation and reduced area coverage on the microchannel surfaces (*i.e.*, 50 mg/ml in Figure 16c).[128,129] The linear trend between the MXene thickness and the loading cycles showed the additive, layer-by-layer deposition characteristic in Table 2.

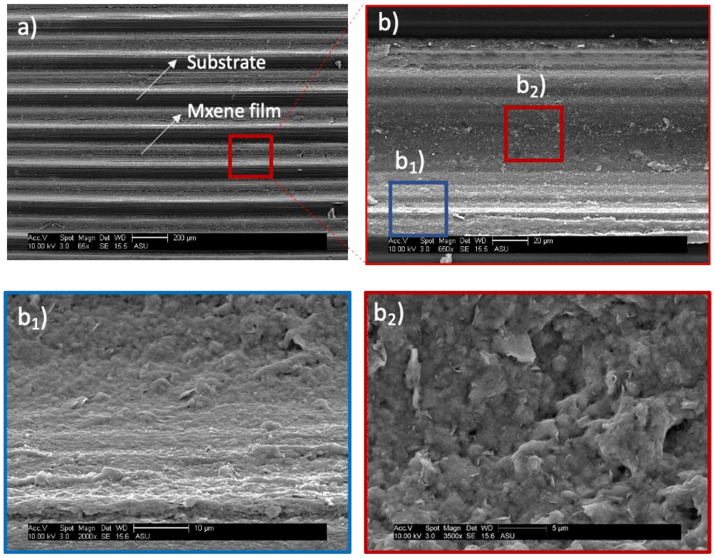

Figure 17. SEM images showing MXene film topography for 10 mg/ml <40> showing continuous and uniform deposition of MXene flakes into microchannels.

Table 2. MXene Film Thickness for Different Concentrations (10, 20, and 50 mg/ml) and Layer Number <n>.

Concentration (mg/ml)	Layer thickness (µm) at deposition layer number <n>			
	5	10	20	40
10	0.50±0.08	1.08±0.41	3.97±0.64	5.38±1.46
20	0.65±0.21	1.36±0.47	4.92±1.97	19.42±2.48
50	0.89±0.26	3.92±1.10	13.84±6.28	36.73±6.28

3.3.6 Electrical, Sensing, and Piezoresistive Properties

For microelectronics, precise positioning and alignment of MXene flakes on complex substrates without any complex chemical and thermal treatment are of great importance to the production of microelectronic devices. A homogeneous and smooth deposition of MXene film onto patterned polymer substrates enables high-performance electromechanical properties with electrical functioning and stretchable flexibility (Figure 18a). Figure 18b shows the anisotropic electrical properties along patterned MXene direction as a function of deposition numbers and ink concentrations. For 10 mg/ml inks, the sheet resistance was determined to be 30.33 kΩ/sqr for <n> = 5, which decreased at a <n> number of 10, 20, and 40 (*i.e.*, 25.76, 12.40, and 0.41 kΩ/sqr, respectively). This resistance reduction was due to the favorable MXene deposition, alignment, network continuity, and packing factor.

With the same printing layer of 40, an increase of MXene/ethanol ink concentration from 10 to 20 and 50 mg/ml increased the device resistance from 0.41 kΩ/sqr to 1.21 kΩ/sqr and 3.75 MΩ/sqr, respectively, showing a conductivity decrease of one to four orders of magnitude (Figure 18b). The more concentrated solutions led to the formation of rough films in the microchannel, causing electron scattering and a decrease in surface electromigration efficiency ($\sigma \propto R^{-2}$).[130,131] The electrical resistance of thin films is thickness-, surface roughness-, and area coverage-dependent. Based on the thickness and sheet resistance at <n>=40, the electrical conductivity of the films was calculated at 626.85 S/m, which was lower than pure $Ti_3C_2T_x$ MXene film from vacuum filtration (*i.e.*, ~130 kS/m in Figure 18c). This is possibly because of an insulating polymer matrix and the larger MXene layer spacing without vacuum effects. Even though the vacuum filtered films showed high electrical conductivity, these free-standing films were too brittle and fragile to resist crack propagations when subjected to subtle bending or fatigue. This conductivity management indicated that by adjusting the ink concentration, film thickness, and deposition morphology, our technique offers digital and additive manufacturing for micropatterning 2D MXene nanoparticles as a resistive/conductive network with a broad range of properties (*i.e.*, an electrical resistance from a few hundred ohms to Mohm) and designable substrate flexibility.

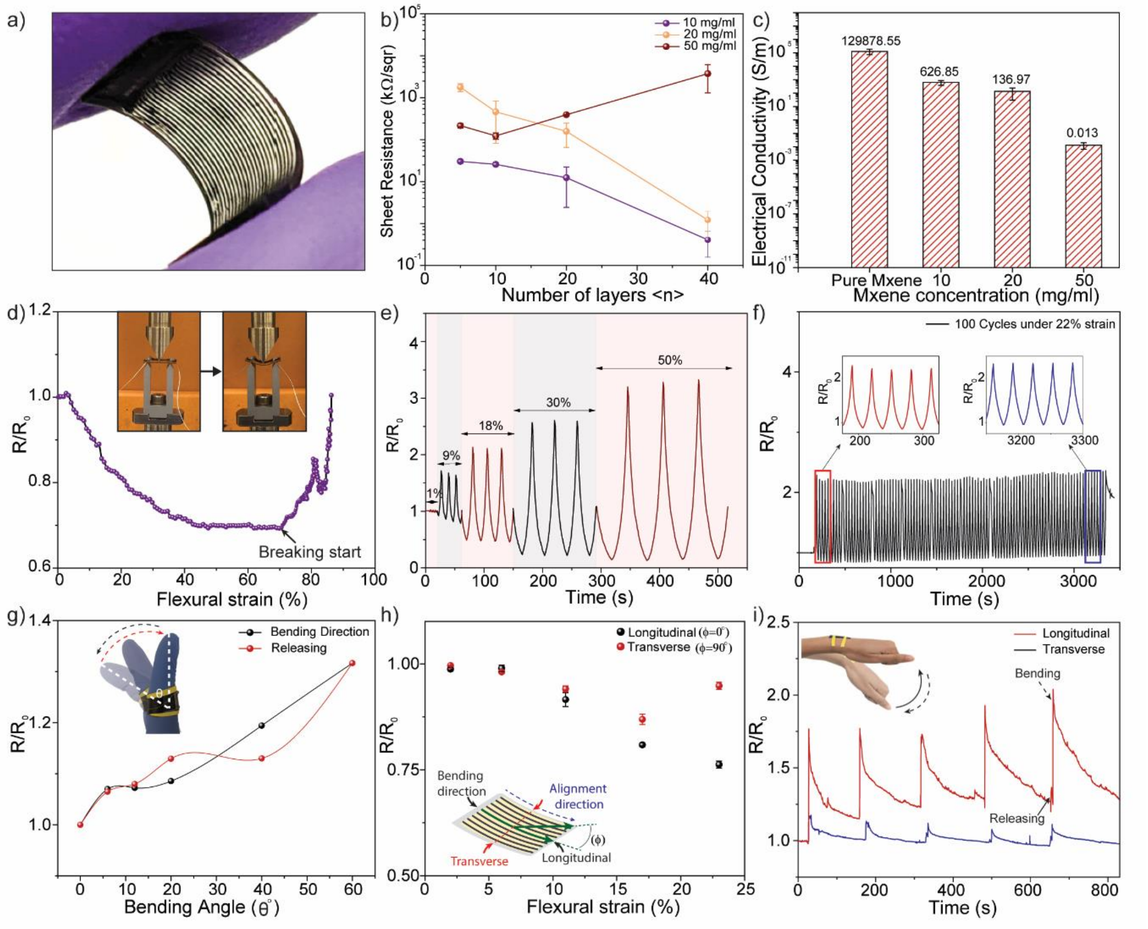

Figure 18. Electrical and piezoresistive properties with a) the digital photograph of the substrate showing mechanical flexibility, b) sheet resistance (R_s) as a function of printing cycles <n> for various inks, c) the electrical conductivity of pure MXene film *via* vacuum filtration and printed composites of different MXene content, d) the normalized resistance *vs*. bending/ flexural strain, e) cyclic performance under bending and unloading cycles from 1% to 50% flexural strains, f) the cyclic fatigue with bending and loading release cycles at a 22% flexural strain, g) the printed device responding to finger motions at different bending angles, h) the anisotropic resistance change as a function of the flexural strain along the longitudinal (ϕ=0°) and transverse directions (ϕ=90°), and i) the electrical responses along with the longitudinal and transverse directions in response to delicate wrist

movement. (Note: Figure 18(d,e,f,h)-inward bending and Figure 18(g, i)-outward bending Figure 19).

The electromechanical performance of the multilayer film was characterized with the 3-point bending performed using Dynamic Mechanical Analyser (DMA) and the resistance change (R/R_0) measured continuously *via* a coupled multimeter (the insert image in Figure 18d). Figure 18d shows that with the continuous increase of flexural strain to the sensor surface, the resistance (i) initially decreased because the MXene multilayers experienced compression on top of the printed device that decreased the inter-MXene spacing and increased the packing factor; and then (ii) increased due to initiation of failure of substrate generates cracks and disrupt the continuity of electron flow.

The electrical resistivity/conductivity change upon mechanical loading is helpful for designing highly sensitive gauge sensors. For example, the resistance variation upon bending at different flexural strains of 1, 9, 18, 30, and 50% confirmed device sensitivity (Figure 18e). The topmost surface experienced compression by bending the flexible substrate within elastic regimes (*e.g.*, << 50%). Upon bending within this range, the MXene flakes came closer and overlapped with each other to form a tunnel junction, transporting electrons more easily through nanolayers by reducing their resistance. After the load removal, the sample bounced back to release its elastic energy due to polymer flexibility. During bouncing, the relocation of MXene, and surface defect generation increases the electrical resistance due to the extended interparticle spacing (Figure 19). However, the sample stretching beyond the elastic region induced a non-reversible resistance change due to the formation of defects (*e.g.*, voids, delamination of nanoparticle layers). With an increase in applied flexural strain, the sample deformed more severely (*e.g.*, more considerable surface compression during loading and more tension during unloading), explaining the increase in resistance change with stepwise loading and unloading cycles (Figure 18e). The gaps and cracks formed due to stretching were not significant in destroying the conductive network; instead, they lengthened the electron conduction pathways.

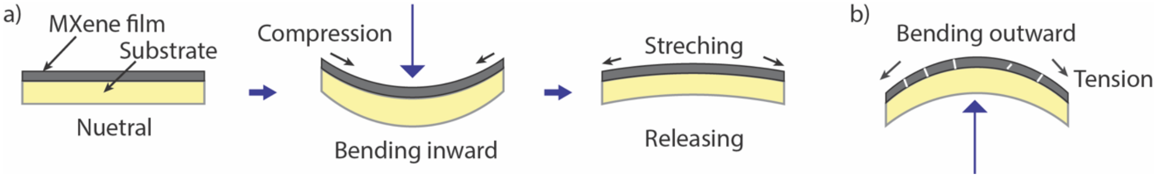

Figure 19. Schematic showing bending sequences for a) inward bending showing neutral position, bending inward, releasing, and stretching of the film (Figure 18 d, e, f, and h); b) outward bending where the MXene film experiences tensile stretch. (The experimental demonstrations of finger and wrist bending were performed with outward bending as shown in Figures g and i).

To better understand the stability of the resistance response with mechanical cycling, the sensor was bent 100 times at 22% flexural strain without showing distinct signal decaying (Figure 18f). High device sensitivity and mechanical reliability can detect delicate human motions, *e.g.*, the index finger bending to different angles (*i.e.*, 0 to 60^o, Figure 18g), bending along different longitudinal or transverse directions (Figure 18h), and wrist rotation with the printed device attached along different directions (Figure 18i). As the finger bending angle increased to 60^o, the normalized resistance became ≈1.4 times more prominent, and the finger bending back to 0^o recovered the initial resistance, implying a fast electron transport capability and stable structural integrity under bending and reloading cycles.

To further reveal the anisotropic piezoresistive property of the MXene sensor, we investigated the effect of bending direction and bending strain on the resistance response for a 2x2 cm device with 10 mg/ml <40> ink printing. Here, we define the angle between alignment /patterning direction and bending direction as a bending angle ϕ. The resistivity changes were measured along the microchannel direction in response to the bending angle (i) 0° (longitudinal) and (ii) 90° (transverse), as shown in Figure 18h. For a flexural strain less than 7%, the response changes along longitudinal and transverse directions were similarly negligible. However, with more considerable mechanical deformation (*i.e.*, 10% to 25%), differences in response increased (*i.e.*, 11% and 23% for $\Delta R/R_o$(%) along with the transverse and longitudinal directions at a flexural strain of ~23%), suggesting anisotropic electrical and sensing behaviors. The higher sensitivity along the longitudinal direction was due to the delicate displacement of MXene flakes and the generation of microcracks that impede electron transport. Besides, along with the microchannel-normal directions, the alternating layers composed of conductive MXene and insulative polymers may serve as mechanical deformation barriers. The sensor's responsiveness was leveraged in the wrist movement sensing due to the unidirectional skin wrinkling (Figure 18i).

The piezoresistive properties are reflected by the electrical resistance variations when subjected to different pressure. Our sample was covered with PDMS in order to transfer applied stress from the PDMS layer to the MXene film. Figure 20a exhibits the change in resistive response (R/R_0) for the pressure ranging from ~2 to 26 kPa and demonstrates the incremental resistance change with increased pressure values. These values showed a stable response without signal attenuation under each loading and unloading cycle. The sensor showed high sensitivity (*i.e.* $(\Delta R/R_0)/\Delta P$) of 4.33 kPa^{-1} under pressure less than 20 kPa and a relative lower sensitivity of 0.097 kPa^{-1} above 20 kPa (Figure 20b). The responses to lower surface pressure (*i.e.*, <20 kPa) indicated greater sensitivity due to deformation in the MXene film that disturbed electron current pathways, broke the interlinks among MXene flakes, and significantly increased film resistance. However, when the applied pressure increased beyond 20 kPa, the sensitivity decreased because the microstructure's deformation tends to saturate. The high sensitivity in our device was due to (i) aligned MXene and the directional electron transport with minimized scattering, and (ii) sensitivity transferred deformation from the flexible substrate to the embedded MXene film leading to microstructural defects and resistance increases.

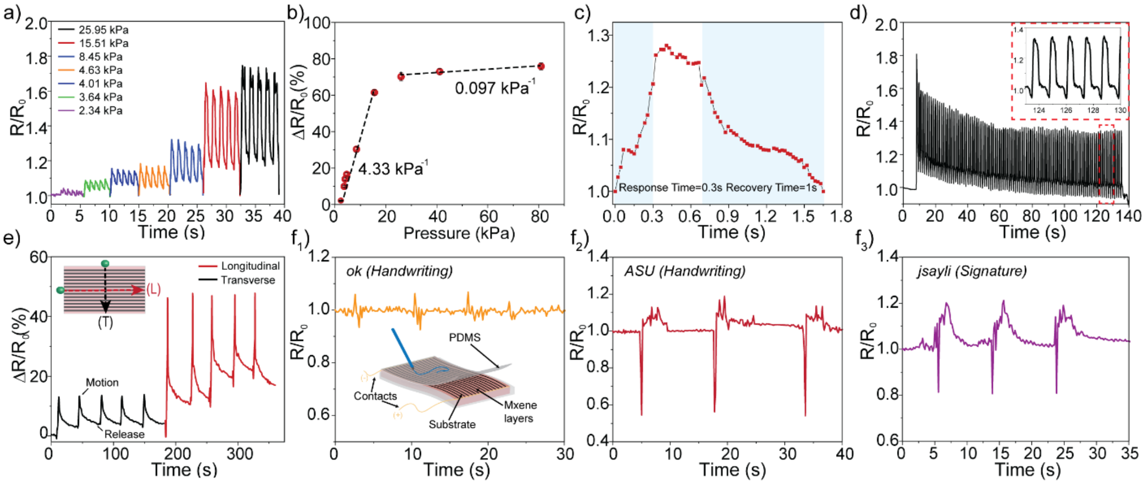

Figure 20. The response of MXene-based sensor to pressure on piezoresistive sensors with the a) sensing responses under pressure loading and unloading from 2.34 to 25.95 kPa, b) the sensitivity as a function of pressure, c) the response time and recovery time of the sensor to 4 kPa, d) the mechanical durability test under the pressure of 15 kPa, e) anisotropic motion sensing in a longitudinal and transverse direction, and f) signature and handwriting sensing.

Besides, our printed sensor showed a fast response time ≈0.3 s and a quick recovery time of ≈0.5s ensuring timely feedback to external pressure (Figure 20c). To evaluate the mechanical durability of an MXene-based sensor, constant pressure of 15 kPa was loaded and unloaded on the sample over 100 times, and no significant recession was observed, indicating high structural robustness (Figure 20d). This demonstration proved high sensing reversibility due to the polymer substrate proception over the microchannel-contained MXene multilayers from delamination.

These MXene-based sensors possess high sensitivity, repeatable selectivity, and rapid response for sensing a wide range of pressure values that can enable cryptosecurity (*e.g.*, fingerprint login, signature identification with highly precise anisotropic/isotropic, and continuous/discrete motion sensing). To test feasibility, we recorded the response of electron flow along the microchannels when an object moved on the device surface with a roughly constant pressure (*e.g.*, a level of ~10 N) along the MXene alignment direction (*i.e.*, longitudinal) and microchannel-normal direction (*i.e.*, transverse)). The sensor showed an increase in resistance to 45% and 14% when the object was moved in a longitudinal and transverse direction, respectively (Figure 20e). Depending on an individual's unique writing characteristic (*i.e.*, force, speed, and continuity), the sensor produced complex and unique waveforms detectable for signature recognitions and handwriting, such as "Ok", "ASU", or "jsayli" (Figure 20f_1-f_3), which has immense potential for anti-counterfeiting applications. Similarly, the sensor showed sensitive responses to finger pressure and lateral motion *via* dynamic finger tapping and releasing cycles, which is useful for tactile applications (Figure 21). These demonstrations showed that our printed devices exhibited advanced sensing applications involving subtle variations in motion speed, direction, and force detectable with high accuracy and sensitivity.

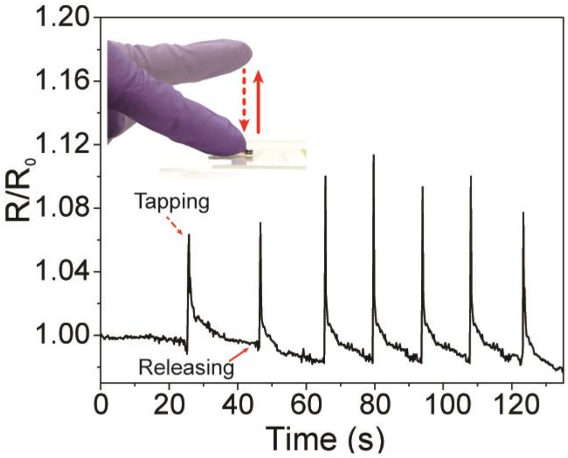

Figure 21. Finger tapping and releasing response of the PDMS-coated MXene sensor.

3.4 Conclusion

We have presented a hybrid and scalable manufacturing approach for nano-aligning and micro-patterning of 2D MXene nanoflakes with hierarchical 3D morphologies. The 3D printing integrated the surface-designable μCLIP technique and nanoparticle-organizable DIW method and provided a layer-by-layer additive manufacturing for the directed assembly of 2D MXene flakes. The highly uniform MXene from our in-house synthesis, the ink rheology control, and the 3D printed surface patterning were critical in directed MXene assembly at low nanoparticle concentrations and minimal viscosity. The additively deposited droplet numbers and the suspension concentrations led to MXene thin films with multilayered stacking, anisotropic alignment, and closely packed deposition morphologies. The laminates between the polymer substrates and layered MXene flakes formed mechanically flexible devices susceptible to bending and pressure, with a few demonstrations in human body motion and signature mode identifications. Our synergistic approach of combining vat-polymerization and ink-writing 3D printing holds immense potential for nanomaterial assembly and broad applications, such as structural composites, sensors, actuators, human-machine interfaces, cryptosecurity, and soft robotics.

REFERENCES

[105] H. Guo, Z. Hu, Z. Liu, J. Tian, *Adv. Funct. Mater.* **2021**, *31*, 2007810.

[106] Y. Zhang, Y. Wang, Q. Jiang, J. K. El-Demellawi, H. Kim, H. N. Alshareef, *Adv. Mater.* **2020**, *32*, 1908486.

[107] B. Xu, M. Zhu, W. Zhang, X. Zhen, Z. Pei, Q. Xue, C. Zhi, P. Shi, *Adv. Mater.* **2016**, *28*, 3333.

[108] K. Kang, K.-H. Lee, Y. Han, H. Gao, S. Xie, D. A. Muller, J. Park, *Nature* **2017**, *550*, 229.

[109] A. K. Pearce, T. R. Wilks, M. C. Arno, R. K. O'Reilly, *Nat Rev Chem* **2021**, *5*, 21.

[110] W. Tian, A. VahidMohammadi, Z. Wang, L. Ouyang, M. Beidaghi, M. M. Hamedi, *Nat Commun* **2019**, *10*, 2558.

[111] B. Elder, R. Neupane, E. Tokita, U. Ghosh, S. Hales, Y. L. Kong, *Adv. Mater.* **2020**, *32*, 1907142.

[112] D. Kokkinis, M. Schaffner, A. R. Studart, *Nat Commun* **2015**, *6*, 8643.

[113] M. Naguib, M. Kurtoglu, V. Presser, J. Lu, J. Niu, M. Heon, L. Hultman, Y. Gogotsi, M. W. Barsoum, *Adv. Mater.* **2011**, 6.

[114] K. Maleski, V. N. Mochalin, Y. Gogotsi, *Chem. Mater.* **2017**, *29*, 1632.

[115] L. Ding, Y. Wei, L. Li, T. Zhang, H. Wang, J. Xue, L.-X. Ding, S. Wang, J. Caro, Y. Gogotsi, *Nat Commun* **2018**, *9*, 155.

[116] J. R. Tumbleston, D. Shirvanyants, N. Ermoshkin, R. Janusziewicz, A. R. Johnson, D. Kelly, K. Chen, R. Pinschmidt, J. P. Rolland, A. Ermoshkin, E. T. Samulski, J. M. DeSimone, *Science* **2015**, *347*, 1349.

[117] G. F. Acosta-Vélez, T. Z. Zhu, C. S. Linsley, B. M. Wu, *International Journal of Pharmaceutics* **2018**, *546*, 145.

[118] G. Vazquez, E. Alvarez, J. M. Navaza, *J. Chem. Eng. Data* **1995**, *40*, 611.

[119] M. Á. Rodríguez-Valverde, M. Tirado Miranda, *Eur. J. Phys.* **2011**, *32*, 49.

[120] E. Shashi Menon, in *Transmission Pipeline Calculations and Simulations Manual*, Elsevier, **2015**, pp. 149–234.

[121] M. Trebbin, D. Steinhauser, J. Perlich, A. Buffet, S. V. Roth, W. Zimmermann, J. Thiele, S. Forster, *Proceedings of the National Academy of Sciences* **2013**, *110*, 6706.

[122] G. Xin, W. Zhu, Y. Deng, J. Cheng, L. T. Zhang, A. J. Chung, S. De, J. Lian, *Nature Nanotech* **2019**, *14*, 168.

[123] S. Ni, L. Isa, H. Wolf, *Soft Matter* **2018**, *14*, 2978.

[124] B. Sun, H. Sirringhaus, *J. Am. Chem. Soc.* **2006**, *128*, 16231.

[125] C. Hanske, M. B. Müller, V. Bieber, M. Tebbe, S. Jessl, A. Wittemann, A. Fery, *Langmuir* **2012**, *28*, 16745.

[126] S. Naficy, R. Jalili, S. H. Aboutalebi, R. A. Gorkin III, K. Konstantinov, P. C. Innis, G. M. Spinks, P. Poulin, G. G. Wallace, *Mater. Horiz.* **2014**, *1*, 326.

[127] B. Akuzum, K. Maleski, B. Anasori, P. Lelyukh, N. J. Alvarez, E. C. Kumbur, Y. Gogotsi, *ACS Nano* **2018**, *12*, 2685.

[128] Q. Li, Y. Gou, T.-G. Wang, T. Gu, Q. Yu, L. Wang, *Coatings* **2019**, *9*, 500.

[129] M. Sebastiani, E. Rossi, M. Zeeshan Mughal, A. Benedetto, P. Jacquet, E. Salvati, A. M. Korsunsky, *Nanomaterials* **2020**, *10*, 853.

[130] V. Timoshevskii, Y. Ke, H. Guo, D. Gall, *Journal of Applied Physics* **2008**, *103*, 113705.

[131] L. Du, D. Maroudas, *Appl. Phys. Lett.* **2017**, *110*, 103103.

CHAPTER 4

A HYBRID 3D PRINTING FOR HIGHLY-EFFICIENT NANOPARTICLE MICROPATTERNING

Abstract: FDM 3D printing often generates inevitable surface phenomena/defects called the "staircase effect," which involves anisotropic material texture, rough surface topology, and interlayer voids. Besides, the staircase morphology (i.e., interlayer microchannel dimensions and surface roughness) can be well-controlled with essential printing parameters, for example, layer height and print orientation. Here, staircase surface defects generated from FDM 3D printing were utilized as the confined environment to directly assemble 2D NPs of MXene as long-range patterned microstructures via a combination with simple DIW 3D printing. Based on the layer-by-layer deposition procedure, Mxene NPs were patterned into microfilm with parallelly stacked morphology by combining the confinement effect from surface microchannels, MXene ink quantity control, and NP-substrate interactions. These commonly regarded surface defects (i.e., staircase effect) from 3D printing demonstrated the potential for large-scale anisotropic patterning of a wide variety of NPs and biomolecules via simple microfluidic forces for structural reinforcement, thermal sensing, microelectronic devices, optical imaging, wireless data transportation, and metasurface applications.

4.1 Introduction

In Chapter 3, the hybrid manufacturing mechanism (µCLIP/DIW) is applied for assembling and patterning 2D MXene NPs 3D printed template. In this Chapter, the similar mechanism is further explored with different 3D printing techniques (i.e., FDM and DIW) to demonstrate the generality and applicability of the NP assembly mechanism.

Even though 3D printing offers different advantages, such as rapid prototyping, fewer material compositions, faster production, product customization, and comprehensive materials selection, each 3D printing technique has certain limitations. For example, the extrusion-based approach generates defects, such as delamination and void formation;[132] vat polymerization technique has limited build size from resins and light control;[55] material jetting-based requires suitable inks, such as viscoelastic properties and wettability with substrates;[133] PBF-based printing generates components that have low mechanical strength and limited surface finish;[134] DED-based printing requires post-processing of components due to high surface roughness;[135] and LOM need decubing with a labor-intensive process.[136] Some defects may significantly deteriorate the performance of the 3D-printed components. However, some of the surface defects can effectively tune surface properties for different applications. For example, FDM 3D printing displays the most widely observed surface phenomena/defects, such as the "staircase effect," which is more noticeable for oblique and curved surfaces.[137,138] Though premature, these surface defects displayed potential as scaffolds/templates for regulating the deposition of anisotropic nanoparticles and biomolecules from their solutions.[139]

For the small-area deposition of NPs on patterned templates (e.g., grooves, microchannels, trenches, pillars), fluid-mediated deposition techniques, including dip coating, spin coating, droplet casting, and microfluidic, have been studied.[140,141] Among them, the microfluidic exhibits many advantages over conventional suspension-based deposition approaches, e.g., fast deposition, precise manipulation fluid, low material consumption, and good scalability.[142,143] Also, the topological micropatterns displayed unique functional properties on the surface, which can be enhanced with nanoscale engineering.[144] However, the challenge is that most template manufacturing has been achieved through traditional processing, such as lithography, micromachining, injection molding, and stamping, which can be compatible with programmable NPs deposition into predetermined sites via microforces.[145–148] These techniques are energy intensive, time-consuming, costly, and laborious. On the contrary, 3D printing technology has the potential for high throughput and large-scale nano/micro-manufacturing.[149,150] On top of that, the printed templates can be customized and designed into complex 3D architectures with multifunctionality highly required for many applications.[106]

In our previous research, we demonstrated novel nanomanufacturing via combining 3D printing (i.e., SLA, μCLIP, MDIW) and fluid-mediated deposition for microscale surface patterning and nanoscale particle alignment.[42,151] The 3D-printed templates with microscale gratings acting as anchoring sites allowed the deposition of NPs at predetermined locations from the particle dispersions.[93,116,152] On the other hand, fluid-mediated deposition utilized interparticle interaction and microfluid forces, such as capillary, van der Waals, and hydrogen bonding without any external field, to assemble nanoparticles onto patterned surfaces.[153,154] In one case, the SLA-printed template anisotropically aligned 1D carbon nanofibers in a layer-by-layer (LbL) manner facilitated by dip coating.[151] To improve the patterning resolution and particle assembly autonomy, μCLIP 3D printing was used in another case study to generate the template with less surface roughness and combined with capillary-induced deposition for well-stacked patterning of 2D MXene flakes.[42] Additionally, in the MDIW, the selective etching of the sacrificial layer generated high aspect-ratio boron nitride micropatterns. Unlike traditional top-down and bottom-up methods, 3D printing and fluid-mediated deposition enabled complex micropatterning and alignment of 1D and 2D NPs in a simple, rapid, scalable, and cost-effective manner.[42,151] Employing patterning and aligning of NPs into 3D architectures, the performance and application range of topological micropatterns can be enhanced. Our previously reported 3D printing processes involved multi-step manufacturing, limited to photosensitive materials, and required post-processing (i.e., curing, washing, and etching). Comparatively, FDM is a faster, single-step process, suitable for a wide range of thermoplastics as substrate materials, and requires minimum optimization of printing parameters.[155] Thus, this 3D printing-enabled nanoparticle assembly mechanism needs to be investigated in the FDM 3D printing technique for cost-efficient surface patterning and scalable nanoparticle assembly.

In this study, we have developed a novel technique for anisotropic patterning and nanoscale stacking of MXene NPs on the 3D printed substrate by integrating the FDM and DIW 3D printing. First, the FDM 3D printing technique generated the template with microscopic surface topology (reservoirs and microchannels) formed via layer-upon-layer filament deposition. Then, MXene ink was dropped into the reservoir by DIW to understand how template surfaces drive the assembly of NPs inside microchannels. The NP assembly was induced by capillary and microfluidic forces acting on NPs on the top of the patterned surface to produce microarrays of MXene. By engineering surface defects (i.e., staircase effect), the template surface microstructure, and the resolution of microchannels, MXene assembly efficiency (e.g., deposition distance, layer thickness, film topology) could be tuned depending on the microchannel characteristics (i.e., layer height

(LH)). Additionally, well-aligned and high-aspect-ratio (≈250) patterning of MXene NPs over meso- and macroscale printing shows potential for quick, high throughput, large-scale, and low-cost NPs deposition techniques.

4.2 Experimental Section

4.2.1 Materials

Acrylonitrile butadiene styrene (ABS) 3D printing filament (diameter of 1.75 mm, glass transition temperature (Tg) ≈105°C, density ≈1.06 gm/cc, CAS-No 9003-56-9, product No 3DXABS011, Sigma Aldrich, USA), and ethanol (anhydrous, ⩾99.5%, Sigma Aldrich, USA, CAS-No 64-17-5) were used in this research. All chemicals were used as received without further purification.

4.2.2 FDM 3D Printing

The pure ABS filament was 3D printed via a Flashforge 3D printer (i.e., the model is Creator 3 Pro) to prepare the template of various topologies (e.g., LH, microchannel dimensions, surface roughness) (Figure 22a). The 3D model consisting of a rectangular substrate (20x5 mm) and a reservoir (2x2 mm) was prepared by SolidWorks software and exported as an STL file for FDM 3D printing. FlashPrint was used to conduct the digital slicing of the 3D model. First, the object was sliced in the direction parallel to the long edge of the substrate (x-y plane) and perpendicular to the reservoir (z-axis), followed by 3D printing in a layer-upon-layer fashion to create the microchannels connecting to the reservoir. Multiple samples were printed before optimizing the 3D printing parameters. The following 3D printing parameters were used: nozzle diameters 0.4 mm, LH 20-400 µm, nozzle temperature 235° C, print bed temperatures 110° C, print speed 60 mm/sec, and infill percentage 100 %.

4.2.3 MXene Nanoparticle Deposition

MXene nanoparticles were synthesized by in-situ HF etching approach as described in Chapter 3 (section 3.2.1). The 5 and 10 mg/ml concentration MXene ink was prepared by dispersing the NPs in ethanol by sonication for 15 minutes. Then the stable ink was loaded into the DIW syringe, and a single drop of approximately 5 µl volume was deposited into the 3D printed reservoir (Figure 22b). After the drop deposition in a reservoir, the dispersion would be confined within the microchannels and driven via capillary action following ethanol evaporation at room temperature (RT) (i.e., controlled by drying thermodynamics with the total time for deposition and evaporation ~10 sec for 2 cm microchannels). After the solvent evaporation, whether the mono- and multilayer microstructure of MXene NPs formed directed assembly within the microchannels would depend on DIW processing parameter control (e.g., the number of deposition layers) and printing ink characteristics (e.g., particle size, colloidal rheology).

4.2.4 Characterization

The SEM images and EDS mapping were measured by FE-SEM (Auriga, SE, 5-20 kV). XRD spectra were obtained from a PAN analytical X'Pert PRO powder diffractometer in the range of 5–70° (2θ) with a step size of 0.01°. The interlayer spacing (d) of multilayered MXene was calculated from the Bragg's law.

The optical imaging, 3D surface imaging, height profile, and surface roughness of the FDM-printed substrates and MXene-deposited thin films were taken from the Keyence optical scanning microscope. In addition, AFM images were captured by Witech Alpha 300 RA in tapping mode with 8 nm tip radius.

The rheology test of MXene dispersion was conducted using TA instruments (Discovery HR2) rheometer with a 40 mm 2° cone Peltier plate. The viscoelastic properties of the MXene dispersion were studied by measuring the viscosity, viscous modulus (G'), and elastic modulus (G") of the sample as a function of frequency (i.e., 1 to 100 Hz) at a constant stress of 0.015 Pa at RT.

4.3 Results and Discussion

4.3.1 3D printing surface templates for directed nanoparticle assembly

The templates with patterned surface features were 3D printed via FDM for subsequent nanoparticle assembly. Commercial acrylonitrile butadiene styrene (ABS) filaments that went through the FDM printhead were heated closer to ≈235°C (recommended extrusion temperature) and extruded through a nozzle onto the printing platform, as shown in Figure 22a. As a result, the surface topology was controlled by depositing extruded filaments on the printing platform in a layer-upon-layer fashion. As known, most FDM methods deposit material as flat layers, which result in a "staircase" effect (Figure 22a) on non-vertical or horizontal surfaces and may mechanically compromise part strength because of adhesion weakness between the laminations. Compared to these generally treated defects of staircases (Figure 22a), this research intentionally created these features (e.g., cross-section contours, individual layer thickness, texture along printing directions) for directed nanoparticle assembly. During FDM printing, the melted ABS filament solidifies immediately upon deposition due to the temperature difference between the extrusion nozzle and the substrate in the ambient atmosphere (i.e., RT). Specifically, the computer-aided design (CAD) model consisting of the flat substrate and a reservoir for the MXene ink deposition was first designed, as shown in Figure 22a$_1$. Then, the surface feature was printed along the longer edge of the substrate to control the polymer layer orientation. As represented in Figure 22a$_2$, the 2D design of the substrate was printed into 3D morphology with the "staircase defects" formed in layer-manufactured microchannels. The template surface topology and resolution of microchannels (depth (D) and width (W)) were adjustable depending on the dimensions of the printing layers (i.e., LH). The FDM 3D printing fabricated the template in a layer-upon-layer manner, with the surface template consisting of an ink reservoir connecting to microchannels. The microchannels acted as material feeding sites for MXene NPs to form long-range ordered microstructures via the LbL deposition of MXene inks during DIW printing (Figure 22b). Due to the capillary action and microfluidic forces, the NPs were transported, confined, and oriented within the microchannels to produce MXene nanoparticle microarrays (Figure 22b$_1$). The evolution of surface topology and composition at different processing stages, such as during the reservoir creation, surface patterning, DIW ink deposition, MXene micropatterning, and their influences on nanoparticle assembly, will be discussed in the subsequent sections.

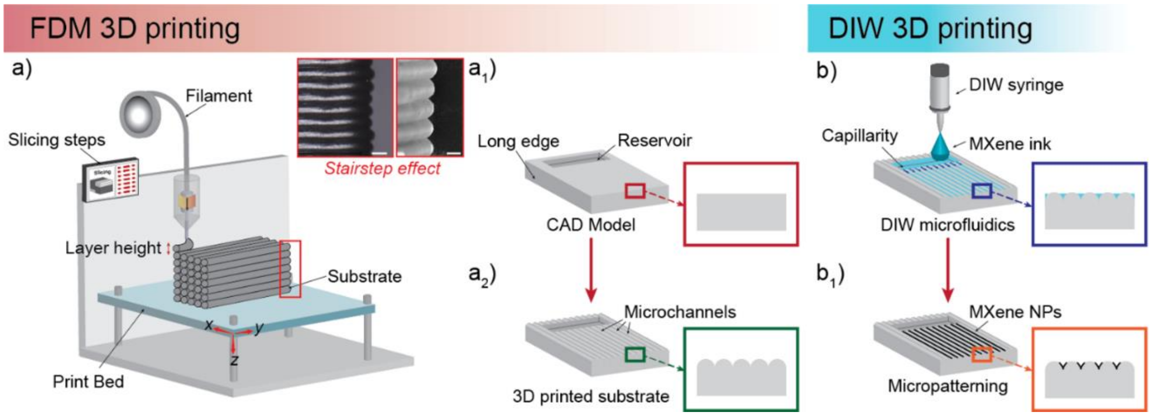

Figure 22. a-b) The schematic shows the working principle of hybrid processing combining FDM and DIW 3D printing for directed assembly of NPs. a) 3D printing of templates from FDM-heated and -extruded thermoplastic filaments of ABS with staircase effect shown in optical (scale bar 300 µm) and SEM (scale bar 100 µm) images and (b) showing the template effects from DIW-deposited MXene inks. Specifically, a$_1$) a designed CAD model of a substrate consisting of a reservoir for ink deposition, a$_2$) the FDM-fabricated template with stair-stepping effects leading to the formation of microchannels on top of the templated surface, b) deposited MXene inks were driven primarily by the capillarity forces within microchannels, and b$_1$) effects of template topology (e.g., cross-section shapes of the substrate tuned by different FDM printing parameters) on MXene nanoparticle assembly efficiency (e.g., particle layer morphologies and layer thicknesses programmable via DIW parameters).

Due to the FDM printing limitations, the template surface morphology and resolution were determined by the layer height. Therefore, samples with different LH values, such as 20, 50, 100, 150, 180, 300, and 400 µm, were printed. The "staircase effect" generated by the additive manufacturing process led to contour-like patterns of the printed substrates, as shown in Figure 23a, where the interlayer spacing increased with the LH. As confirmed by optical profilometer measurements, LH values were close to the theoretical predictions, which proved the accuracy and consistency of the 3D printing system. The contour-like staircase features were anisotropic, desirable for directed NP assembly useful for heterogeneous mass transport (e.g., limited electron or phonon scattering). The cross-sectional SEM images provided additional information about the staircase morphology as well as the dimension of the microchannels (Figure 42). The staircase effect generated the microchannels (black region) between adjacent printed layers (white area), which showed sine-wave shape morphology with the variation in microchannels D and W. The D and W linearly increased as a function of the LH with a rough slope of one, as represented in Figure 23b. For LH= 20 and 300 μm, the average depth was measured as D ≈7.5 and ≈110 μm, respectively. The width of microchannels was measured as W ≈30, 103, 148, and 300 μm for LH= 20, 100, 150, and 300 μm, respectively. Lower LH (i.e., < 50 μm) resulted in structures with smooth surface finish (surface roughness (S_a) ≈3.6 μm) due to more closely packed layers, as shown in 3D imaging (Figure 23c_1). Similarly, higher LH displayed increased S_a generated on the printed substrate surface. For example, staircase surface morphology was observed in LH= 100 and 300 μm samples with an average S_a of ≈11.6 and 38.6 μm, as shown in 3D images (Figure 23c_2-c_3). The structural defects between the adjacent layers for different LH were identified through SEM analysis (inset imaging in Figure 23c). For LH<50 μm, there were interlayer diffusions due to molten molecular chain movement among densely packed layers (Figure 23c_1). On the other side, for LH>300 μm, poor bonding between the adjacent layers caused possibly by uneven heating would form micro gaps or voids at the interface (Figure 23c_3). The layer delamination along the printing plane normal has been the most prominent defect in FDM 3D printing, which influences the transverse mechanical properties of the components (i.e., fracture toughness and strength).[156,157] As compared, although smaller LH minimized the voids in the FDM 3D printed substrates, it also negatively affected the production efficiency.[158] As LH decreased, the number of layers required to print the same-dimension substrates increased (i.e., 500, 100, and 33 layer numbers for LH 20, 100, and 300 μm, respectively), leading to lower manufacturing rates. Therefore, this research focuses on the optimized printing parameter (i.e., LH= 100 μm used as one example) to demonstrate directed nanoparticle assembly due to well-controlled surface topology, distinct interfaces, consistent microchannels, and predictable microforces.

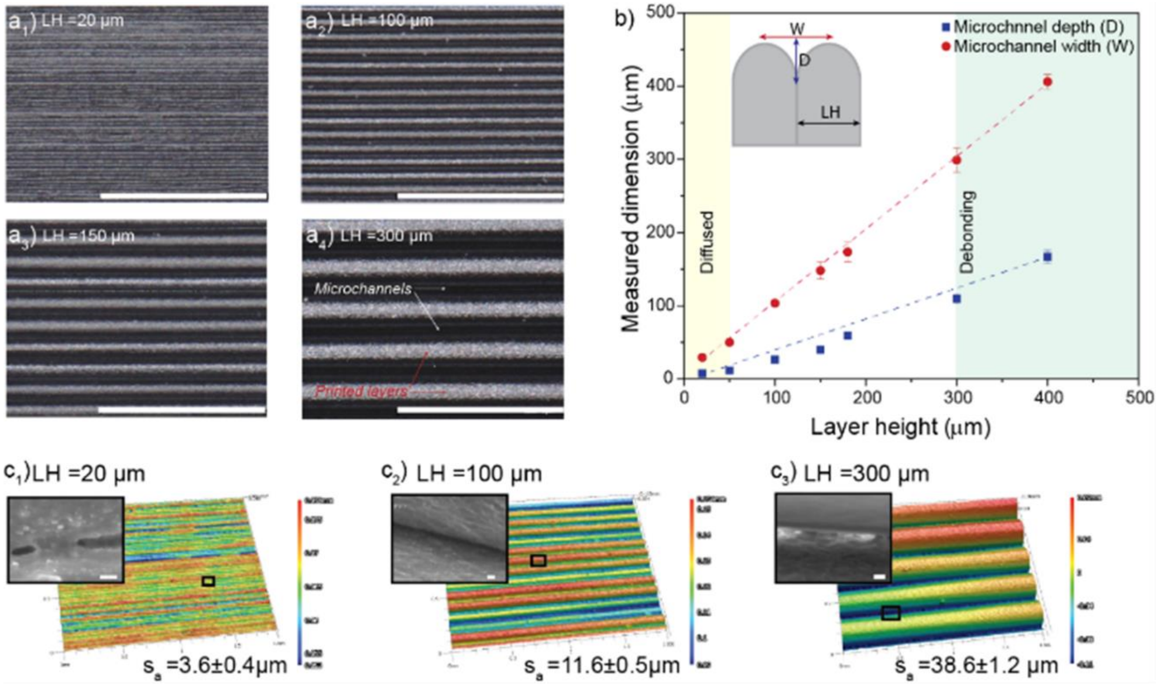

Figure 23. Surface template morphologies. a_1-a_4) Optical images of FDM 3D-printed substrates having different layer LH values (i.e., 20, 100, 150, and 300 μm) with the white region as the FDM-printed layer and the black region as microchannels (scale bar 1200 μm), b) measured dimensions of microchannels (i.e., D and W) depending on the LH

control, showing the layer diffusion and inconsistency below 50 µm and layer debonding above 300 µm and defining our printing window to be [50 µm, 300 µm]. Furthermore, the surface profile characterizations validated this surface template printability in the confocal optical microscope (COM) and SEM imaging in c_1-c_3), with the COM showing the printing roughness (i.e., an average roughness values of ≈3.6 µm, 11.6 µm, and 38.6 µm as a result of the staircase effect for LH ≈20, 100, and 300 µm) and zoomed-in SEM images showing the different interfacial behaviors, namely, the diffused, clear, and debonded interfaces (scale bars of 2 µm in SEM images).

4.3.2 MXene synthesis with tunable particle dimensions and physics

The MXene flakes were synthesized by the selective chemical exfoliation of the Al layer from the Ti_3AlC_2 MAX phase, as described in the experimental section. The crystal structure changes during the chemical etching and exfoliation process are represented in Figure 24a. First, the Ti_3AlC_2 MAX phase powder was prepared by mechanical milling followed by heat treatment, which displayed closed stacked and layered morphology (Figure 43a). Next, the MAX phase was etched using a mixture of lithium fluoride (LiF) salt and hydrochloric acid (HCl) for etching the Al layer and obtaining the multilayered accordion-like MXene (Figure 43b). Then, the etched multilayers were exfoliated into single- and few-layered MXene flakes by sonication and centrifugation, as shown in Figure 24b, with an average lateral size of ≈500 nm and thickness of ≈7.5 nm. The MXene nanoflakes film after filtration showed stacking morphology with small interlayer spacing. The EDS mapping confirmed the successful removal of Al and the formation of oxygen and fluorine surface termination with the homogenous distribution of Ti, C, O, and F (Figure 24c). The well-exfoliated MXene structures were also reflected in the XRD spectra of the precursor MAX phase and MXene nanoflakes. For example, the delamination of $Ti_3C_2T_x$ MXene displayed the distinct peak shift for (002) characteristic peak from 9.43° (MAX) to 6.73° (MXene) due to increased interlayer spacing with the disappearance of crystalline peaks near 40.0° (Figure 24d). Additionally, the broadening of the (002) peak suggested an increase in d-spacing (9.37 to 13.26 Å) and a decrease in the thickness of $Ti_3C_2T_x$ layers.

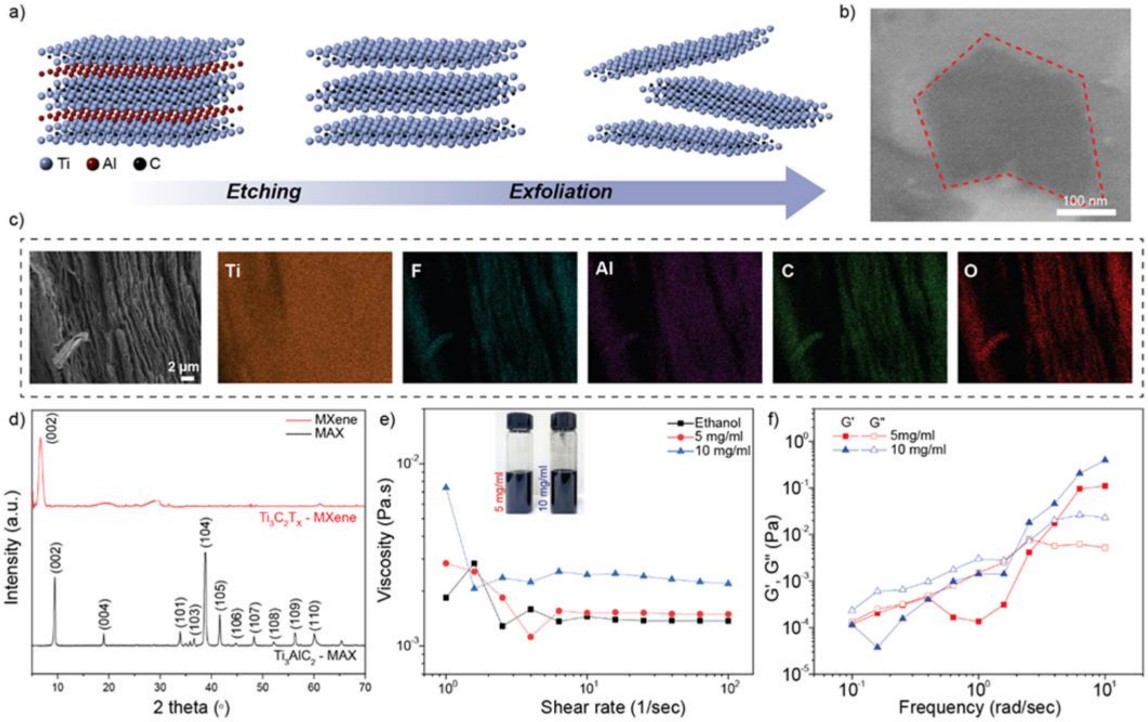

Figure 24. a) The schematic showing the chemical etching and exfoliation process of Ti_3AlC_2 during the syntheses of MAX powders and MXene nanoparticles, b) SEM image showing the MXene surface flatness, and c) SEM image and EDS scanning of MXene cross-section showing the layered morphology in nanoflakes, d) XRD spectra of MAX phase and MXene nanoflakes, e) viscosity of MXene/ethanol inks as a function of shear rates (1-100 1/sec), and f) viscoelastic properties (G' and G") of MXene/ethanol inks as a function of frequency (rad/sec).

The MXene flakes owing to their hydrophilic nature, show excellent dispersibility in water, ethanol, and many other solvents.[114] Here, the $Ti_3C_2T_x$ MXene nanoflakes were added in ethanol because it has low surface tension, good wettability, and a fast evaporation rate. The MXene/ethanol dispersion was prepared by sonicating for 15 min, resulting in a mixture (i.e., 5 and 10 mg/ml) with excellent stability without any macroscopic precipitates or aggregation even 24 hr after preparation (Figure 24e). In addition to dispersion homogeneity, the rheological properties of the inks were significant properties ensuring the successful deposition and patterning of NPs. The viscosities of the ink as a function of shear rate were measured as depicted in Figure 24e. The 5 and 10 mg/ml inks exhibited typical shear thinning behavior, enabling smooth extrusion of MXene ink through the small-diameter DIW nozzle under shear forces and droplet deposition. However, higher MXene particle loading (> 10 mg/ml) would decrease the fluidity of the dispersion due to the increased aggregation of NPs via hydrogen and van der Waals bonding.[159] The viscoelastic properties of the inks were also investigated by performing an oscillation sweep at a constant strain rate. The storage modulus (G') and loss modulus (G") of the inks were recorded as a function of frequency (rad/sec) at fixed stress 0.015 Pa (Figure 24f). The inks showed the transition from a liquid to solid-like nature at frequencies of ≈3 and 1.9 rad/sec for 5 and 10 mg/ml, respectively. The frequency increase in gelation could probe microstructural rearrangement with the solidification of ink at shorter time scales.[59] The magnitude of modulus increased with the ink concentration, indicating higher interparticle interaction, which would cause crowding of NPs.[160] The dominance of G" over G' displayed that the MXene/ethanol dispersion was suitable for high shear-rate processing methods via suspension-based deposition approaches. These rheological characteristics were thus ideal for processing low-concentration inks without causing clogging of printhead and patterned features.

4.3.3 Directed 2D MXene Assembly

The primary principle for the directed nanoparticle assembly involves the (i) confinement of nanoparticles to reduce interparticle interactions (e.g., van der Waals, electrostatic, hydrogen bonding), (ii) capillarity-driven mass transport to distribute along microchannels, and (iii) shear-stress for 2D plane orientation and stacking. The width and depth of microchannels are typical structural features of microchannels tunable during 3D printing (Figure 23). For example, Figure 25a-b explains the effect of microchannel dimensions on the transport of MXene inks. Regardless of the MXene/ethanol concentrations in inks, the substrate with a deeper microchannel (i.e., corresponding to larger capillary forces) transported a higher amount of MXene ink from the 500 μm-deep reservoir into the microchannels (Figure 25a-b). During FDM, the depth of the microchannel was adjusted by the variation of LH from 20-300 μm. A single droplet of 5 μL of MXene ink was dropped into the reservoir, and the transport distance of the nanoparticles was measured. For LH= 100 μm samples, the transport distance was ≈52.29% and 85.18% higher than LH= 50 μm for 5 and 10 mg/ml, respectively. For LH <50 μm, MXene ink could not flow into the microchannel due to the smaller channel depth and frequent interparticle interactions. Besides, layer diffusion could also disrupt the consistency of directed nanoparticle assembly. As LH increased with deeper microchannels, the deposition distances also increased for LH= 50-180 μm because of increased capillary forces and other comparatively negligible microforces (e.g., particle gravity, van der Waals). For LH>300 μm, the MXene ink would not be effectively deposited between the channels due to leakage of the fluids from the micro gaps. More importantly, the lack of strict confinement over MXene nanolayers lacked the control of extra momentum (e.g., local fluid turbulence due to printing layer roughness). The effect of NPs loading on the transport distance of MXene ink was also investigated, which showed that for less viscous ink, the transport distances were more prolonged across the microchannel (Figure 25c). For example, the transport distance for 10 mg/ml was shorter than in LH= 100 μm due to more vital interparticle interactions. The transport velocity of MXene ink transport for LH =100 μm was calculated as ≈0.3 and ≈0.1 mm/sec for 5 and 10 mg/ml, respectively.

The ANSYS Fluent simulation was performed to verify the influence of microchannel dimensions on MXene ink distribution. The analysis determined the volume distribution of 5 mg/ml MXene ink into microchannels of different dimensions (i.e., LH 50, 100, 150, 180 µm, and 20 mm length) via capillary action. Figure 25d demonstrates that the higher capillary force for high LH microchannels (Table 4) favored the spreading of MXene ink into microchannels and thus higher volume of ink was driven into the microchannel. The increase in the aspect ratio of microchannels resulted in the rapid spreading of MXene ink from LH 50 to 180 µm, similar to experimental observations. These simulation results proved the effectiveness of capillary action in driving MXene ink into 3D-printed templates in an autonomous fashion.

For 3D printed microelectronics, the straight-line micropatterns of different widths, gaps, and thicknesses are essential for high-performance devices. By carefully designing the FDM templates and programming ink rheology, linear or circular micropatterns of conductive NPs can be directly assembled, leading to value-added functions (e.g., electrical conductivity or heat transfer). The optical image shows the MXene NPs were trapped within the microchannel via capillary action for a single droplet of MXene ink of 5 μL. Multiple droplets (DIW printing cycles, #n) of MXene inks were deposited into the reservoir to obtain the uniform deposition of MXene NPs. The optical images show the distinct change in the deposition morphology from a non-uniform deposition for #1 to a continuous deposit for #10 (Figure 26a$_1$-a$_2$) after the evaporation of ethanol at RT. The successive sediment of MXene ink droplets, followed by the evaporation of ethanol, and a thin layer of MXene NPs deposited into cm-scale microchannels proved the nano-manufacturability and assembly efficiency of long-range anisotropic microstructures. For example, the linear micropatterns of MXene NPs of width ≈41 μm, gaps ≈54 μm, and an aspect ratio ≈250 can be quickly generated within minutes via hybrid manufacturing combining FDM and DIW 3D printing techniques. The SEM and EDS mapping also confirmed the formation of linear micropatterns with MXene confinement, smooth surfaces, and particle edge-to-edge connectivity within the microchannels (Figure 26a$_3$). The cross-sectional SEM image of patterned structures also shows the well-stacked and in-plane parallelly aligned MXene flakes formed due to shear-assisted MXene exfoliation (Figure 26a$_4$).

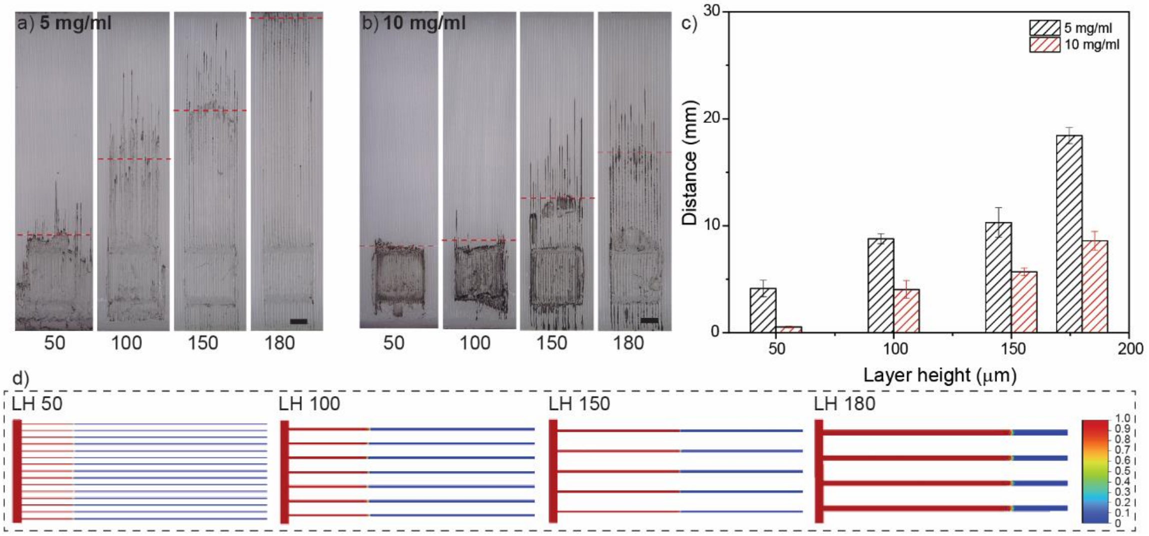

Figure 25. Optical imaging of the MXene ink transport distances along microchannels from the DIW-deposited 5 µL size droplets for a) 5 mg/ml and b) 10 mg/ml MXene/ethanol colloids with varying surface LH (i.e., 50, 100, 150, and 180 µm) (scale bar 1200 µm), c) distance traveled from the MXene inks driven via the capillary action showed consistent increases as a function of LH but decreased as a nanoparticle concentration, d) ANSYS Fluent simulation results of MXene ink (5 mg/ml) transported within microchannels of different LH via the capillary effect (scale bar represents the volume fraction of MXene ink).

Figure 26b schematic illustrates the directed assembly mechanism via NPs transportation and stacking, a combination of (i) capillarity from microfluidic, (ii) shear forces from Newtonian fluids, and (iii) gravity from evaporative force-assisted sedimentation.[42,161] Specifically, the nanoparticle micropatterning was initiated by the formation of ink meniscus between the walls of microchannels from the colloidal delivery, where the NPs are accumulated and assembled into millimeter-long arrays (Figure 25a-b). The rapid evaporation of ethanol caused the NPs to sediment at the bottom microchannels, followed by NPs self-assembly via short-range intermolecular forces. As the ethanol displayed good wettability on ABS (i.e., 15.5° (Figure 44), the capillary force was the dominant force for MXene ink deposition compared to other micro forces (e.g., drag force and gravitational force).[42] The shear fields within the microchannel promoted the alignment of 2D MXene flakes, considering much smaller gravity, buoyancy, and van der Waals. This is because the small, Reynolds number (Re) (i.e., Re <<1), representing a laminar flow of the ink for smooth and uniform deposition of NPs followed by ethanol evaporation.[47] Last but not least, this 2D flake orientation was retained during solvent evaporation in the vicinity of the deposition sites. The U-shape meniscus of the confined ink got MXene pinned to the microchannel surface because of the excellent wettability of the ink, and the evaporation of ethanol accelerated the convection towards the meniscus, eventually resulting in the compliance of NPs to the microchannel wall surfaces. During the solvent's evaporation, the inks' viscosity increased, and particles were sedimented within the microchannels. The rigid 2D layers caused localized compliance of MXene to the microchannel walls in the form of a thin film. After the first layer deposition, the lateral capillary force would work between the adjacent NPs due to the Laplace pressure gradient to connect MXene edge-to-edge in subsequent assembly (Figure 45).[162] The shearing of NPs followed by short-range forces, such as microcapillary force and van der Wall force, resulted in the long-range in-plane and out-of-plane ordering of NPs with high assembly effectiveness.[163] This technique shows massive potential for the deposition of different nanoparticles and possible biomolecules with directed assembly at the microscale.

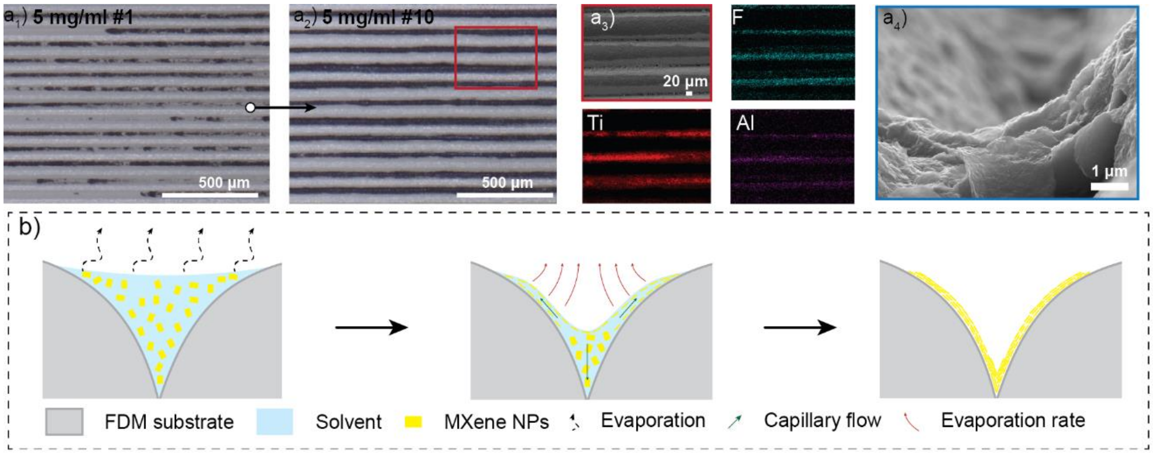

Figure 26. a_1-a_4) optical, SEM, and EDS maps showing the surface topography and parallel stacking of MXene NPs deposited into microchannels with 100 µm LH for 5 mg/ml MXene inks, and b) schematics describing the mechanism of MXene NPs deposition and assembly.

4.4 Conclusion

The staircase effects, usually treated as manufacturing defects in 3D printing, can be utilized as an effective template for the selective deposition, preferential orientation, and anisotropic placement of MXene NPs. By optimizing the FDM printing parameters (e.g., contour profiles, LH, print orientation), the surface topology (i.e., microchannels) on the top of the template can be created. The programmable 3D microchannels of different dimensions were shown to be effective for directional nanoparticle assembly. The drying of ethanol within microchannels formed a meniscus between the sidewalls of microchannels, driving the NPs toward the bottom of the meniscus within the confined region. This research showed the combination of FDM 3D printing for designing surface topography with DIW 3D printing for templated NPs self-assembly. The resolution of microchannels, the viscosity of MXene inks, and NPs-substrate interactions were critical parameters for the confinement, alignment, and edge-edge interconnections among patterned MXene flakes. With this defect engineering strategy, many nanoparticles and biomolecules having a structurally anisotropic nature can be potentially patterned into long-range orders for broad applications.

[132] Y. Tao, F. Kong, Z. Li, J. Zhang, X. Zhao, Q. Yin, D. Xing, P. Li, *Journal of Materials Research and Technology* **2021**, *15*, 4860.

[133] S. Mora, N. M. Pugno, D. Misseroni, *Materials Today* **2022**, *59*, 107.

[134] M. Ziaee, N. B. Crane, *Additive Manufacturing* **2019**, *28*, 781.

[135] M. Lalegani Dezaki, A. Serjouei, A. Zolfagharian, M. Fotouhi, M. Moradi, M. K. A. Ariffin, M. Bodaghi, *Advanced Powder Materials* **2022**, *1*, 100054.

[136] B. Dermeik, N. Travitzky, *Adv. Eng. Mater.* **2020**, *22*, 2000256.

[137] H. Guo, J. Xu, S. Zhang, G. Yi, *Applied Sciences* **2020**, *11*, 304.

[138] S. Wickramasinghe, T. Do, P. Tran, *Polymers* **2020**, *12*, 1529.

[139] S. Miao, M. Nowicki, H. Cui, S.-J. Lee, X. Zhou, D. K. Mills, L. G. Zhang, *Biofabrication* **2019**, *11*, 035030.

[140] D. Baranov, A. Fiore, M. van Huis, C. Giannini, A. Falqui, U. Lafont, H. Zandbergen, M. Zanella, R. Cingolani, L. Manna, *Nano Lett.* **2010**, *10*, 743.

[141] M. Grzelczak, J. Vermant, E. M. Furst, L. M. Liz-Marzán, *ACS Nano* **2010**, *4*, 3591.

[142] A. Olanrewaju, M. Beaugrand, M. Yafia, D. Juncker, *Lab Chip* **2018**, *18*, 2323.

[143] N. Bhattacharjee, A. Urrios, S. Kang, A. Folch, *Lab Chip* **2016**, *16*, 1720.

[144] H.-N. Barad, H. Kwon, M. Alarcón-Correa, P. Fischer, *ACS Nano* **2021**, *15*, 5861.

[145] D. Lebedev, G. Malyshev, I. Ryzhkov, A. Mozharov, K. Shugurov, V. Sharov, M. Panov, I. Tumkin, P. Afonicheva, A. Evstrapov, A. Bukatin, I. Mukhin, *Microfluid Nanofluid* **2021**, *25*, 51.

[146] L. Jiang, N. S. Korivi, in *Nanolithography*, Elsevier, **2014**, pp. 424–443.

[147] D. J. Guckenberger, T. E. de Groot, A. M. D. Wan, D. J. Beebe, E. W. K. Young, *Lab Chip* **2015**, *15*, 2364.

[148] K. Sugioka, J. Xu, D. Wu, Y. Hanada, Z. Wang, Y. Cheng, K. Midorikawa, *Lab Chip* **2014**, *14*, 3447.

[149] W. Xu, S. Jambhulkar, D. Ravichandran, Y. Zhu, M. Kakarla, Q. Nian, B. Azeredo, X. Chen, K. Jin, B. Vernon, D. G. Lott, J. L. Cornella, O. Shefi, G. Miquelard-Garnier, Y. Yang, K. Song, *Small* **2021**, *17*, 2100817.

[150] D. Ravichandran, W. Xu, S. Jambhulkar, Y. Zhu, M. Kakarla, M. Bawareth, K. Song, *ACS Appl. Mater. Interfaces* **2021**, *13*, 52274.

[151] S. Jambhulkar, W. Xu, D. Ravichandran, J. Prakash, A. N. Mada Kannan, K. Song, *Nano Lett.* **2020**, *20*, 3199.

[152] L. Lu, P. Guo, Y. Pan, *Journal of Manufacturing Science and Engineering* **2017**, *139*, 071008.

[153] T. Brezesinski, M. Groenewolt, A. Gibaud, N. Pinna, M. Antonietti, B. Smarsly, *Adv. Mater.* **2006**, *18*, 2260.

[154] P. Zhu, T. Kong, C. Zhou, L. Lei, L. Wang, *Small Methods* **2018**, *2*, 1800017.

[155] D. Rahmatabadi, A. Aminzadeh, M. Aberoumand, M. Moradi, in *Fused Deposition Modeling Based 3D Printing* (Eds.: H. K. Dave, J. P. Davim), Springer International Publishing, Cham, **2021**, pp. 131–150.

[156] H. Gonabadi, A. Yadav, S. J. Bull, *Int J Adv Manuf Technol* **2020**, *111*, 695.

[157] H. Kim, K.-H. Ryu, D. Baek, T. A. Khan, H.-J. Kim, S. Shin, J. Hyun, J. S. Ahn, S.-J. Ahn, H. J. Kim, J. Koo, *ACS Appl. Mater. Interfaces* **2020**, *12*, 23453.

[158] J. Wu, *IOP Conf. Ser.: Mater. Sci. Eng.* **2018**, *392*, 062050.

[159] X. Meng, Y. Sun, M. Yu, Z. Wang, J. Qiu, *Small Science* **2021**, *1*, 2100021.

[160] S. Abdolhosseinzadeh, J. Heier, C. (John) Zhang, *J. Phys. Energy* **2020**, *2*, 031004.

[161] H. Zargartalebi, S. H. Hejazi, A. Sanati-Nezhad, *Nat Commun* **2022**, *13*, 3085.

[162] K. Kato, F. Dang, K. Mimura, Y. Kinemuchi, H. Imai, S. Wada, M. Osada, H. Haneda, M. Kuwabara, *Advanced Powder Technology* **2014**, *25*, 1401.

[163] D. Luo, C. Yan, T. Wang, *Small* **2015**, *11*, 5984.

CHAPTER 5

A MULTI-MATERIAL 3D PRINTING-ASSISTED MICROPATTERNING

Abstract: Micropatterned structures have applications in microchips, circuit board designs, microfluidics, evaporator/condenser coils, microelectronics, metasurfaces, and other functional devices. Conventional microfabrication techniques include lithography, vapor deposition, and laser writing. However, these methods have slow processing rates, complex requirements, or costly procedures. As a result, it is challenging to fabricate micropatterned structures onto large-scale surfaces with high production rates and resolution features. Thus, this study focuses on a non-conventional, mask-free micropatterning technique that combines bottom-up 3D printing capable of processing multiple materials and top-down wet etching for selective elimination of sacrificial material. The unique 3D printing, Multiphase Direct Ink Writing (MDIW), utilizes various polymer and nanoparticle systems as feedstocks for depositing lamellar structures containing sublayers of varying compositions (i.e., wet etchable sacrificial ink and ultraviolet-curable patterning ink). The rapid phase transformation of photosensitive ink into solidified features enables "micro-confinement" of the sacrificial ink. Subsequently, wet etching can locally and selectively dissolve sacrificial polymers by solvent diffusion and polymer dissolution at the polymer-solvent interface. The parameter control (i.e., ink rheology, polymer-polymer interdiffusion, layer multiplication, phase transformation, and solvent-polymer interactions) can precisely tune the lamellar-groove transition, thus forming desirable surfaces or internal microstructures. Our MDIW 3D printing and its facilitation in surface micropatterning demonstrate the massive potential of distributing nanoparticles for

dissipating thermal energies. With production scalability, operation simplicity, and multi-material compatibility, our 3D-printed micropatterning shows broader applications in nanoparticle assembly, drug delivery, optical lenses, intelligent microbots, and morphing objects.

5.1 Introduction

In previous chapters, we discussed the use of 3D printing techniques such as SLA, µCLIP, and FDM to create templates with a resolution of hundreds of microns. In chapter 4, a new 3D printing technique called MDIW is introduced to improve patterning resolution to the tens of micron scale. MDIW is a technique that enables the printing of laminar multilayer structures with individual layer thicknesses on the order of sub-ten microns. This 3D printing technique combined with wet etching involves can precisely control the dissolution of sacrificial layers, allowing for the creation of complex, high-resolution structures from retaining layers with a high degree of accuracy.

Surface patterned 2D or 3D microstructures (*e.g.*, dots, lines, grooves, wells, sieves, pillars, and cellular solids) have been of significant importance in numerous applications, such as microfluidics, microelectronics, optoelectronics, photovoltaics, microreactors, and biomedical devices.[164–166] Conventional techniques used to generate micropatterned surfaces include self-assembly (*e.g.*, coffee ring, flow field, electrical field, or magnetic field directed assembly), micromolding (*e.g.*, roll-to-roll, microcontact printing, replica molding, solvent-assisted micromolding), lithography (*e.g.*, soft lithography, electron beam lithography, nanoimprint lithography), and vapor deposition (*i.e.*, physical vapor deposition (PVD), CVD).[36,37,144,167–169] Among these techniques, self-assembly has been effective in nanomaterial organizations. However, the thermodynamically and kinetically controlled procedure often appears in small-area or volume fabrications.[88] For example, block-copolymer (BCP) crystals can be engineered with pre-designed surfaces that nanoparticles can form orientations or periodicity with external field stimuli.[144,170] In comparison, micromolding has acceptable scalability due to its simple mechanism but only provides 2D surface features.[43] On the contrary, lithography-based methods can design complex features but have tedious multistep processes (*e.g.*, spin coating, masking, baking, developing, and etching) with delicate parameter control.[171] Vapor deposition techniques can generate submicron to nanoscale featured resolutions; however, the high pressure and temperature-controlled reactions are slow and chemically complex, with large footprint apparatuses in scalable manufacturing.[36]

Etching for fabricating micro or nanoscale features is essential in semiconductor industries.[172] Dry etching methods avoid chemical solvents and can provide high processing precisions, but they are limited to a few costly techniques, *e.g.*, reactive ion etching, plasma etching, and multiphoton lithography.[1] Comparatively, wet etching is a cost-efficient and convenient technique for delicate structural design, primarily *via* polymer-assisted patterning and selective elimination.[173] For example, in microlithography, polymer dissolution plays a crucial role in fabricating positive and negative resist for the semiconductor industry. Another example is inkjet-etching, which can fabricate concave surface microstructures, such as microwells and microgrooves, by ejecting organic solvent droplets onto an insulator polymer film, followed by polymer dissolution.[175,176] However, the polymer dissolution strategy only generates as high feature resolutions as hundreds of microns, with limited microfeature depth up to the sub-micrometer range.[177] The universal etching rates from the solvent-polymer interactions also affect the patterning regularity. Moreover, selective etching of uniform surfaces may need mask assistance, adding time and technical challenges to patterning processing. Hence, it is still challenging to fabricate surface micropatterning with controlled high-resolution or tunable morphology in a low-cost, large-area, highly efficient, and flexible way.

As an alternative to conventional micropatterning approaches, 3D printing has played an essential role in micropatterning. *Via* 3D printing, small molecules and nanoparticles can be assembled through an on-demand manufacturing and maskless process. Different 3D printing approaches, such as SLA,[70,151,178] DLP,[179] volumetric printing,[180] CLIP,[42,116] FDM,[71] DLW,[181] DIW,[51] electrohydrodynamic jetting (EHD),[182,183] aerosol jet,[184] and inkjet,[175,185] have been studied for regular or irregular patterns, hierarchies, or architectures *via* a layer-by-layer additive strategy. Many of these 3D printing techniques have proven a high degree of design flexibility to fabricate functional devices, such as origami structures, heat exchangers, circuit boards, batteries, supercapacitors, sensors, actuators, microfluidic devices, and biomedical devices.[186,187] However, photosensitive monomer-based printing (*e.g.*, SLA, DLP, CLIP, DLW) relies on a limited class of monomers with residue on printed objects mandating the post-processability.[188] Current extrusion-based methods (*e.g.*, FDM, DIW) can print various topologies but also have difficulties printing multiple materials, manipulating sub-printing line compositions, or designing submicron structures. Ink-based methods (*e.g.*, EHD, aerosol, and inkjet) have been the mainstream in printed circuit boards due to their high-resolution control at the micron or even nanoscale; however, the printing speed has been limited to the nozzle size and ink quality, especially at the microscale.

This paper reports the facile and mask-free technique for fabricating micropatterns by combining bottom-up 3D printing and top-down wet etching methods. A 3D printing platform, MDIW has been developed for the first time with multi-material compatibility and wet etchability for micropattern fabrication. The MDIW 3D printing has two immiscible, solvent-free inks printed into lamellar structures. These two inks consist of alternating sublayers of wet-etchable sacrificial ink (*i.e.*, polyethyleneimine (PEI)) and UV-curable patterning ink (*i.e.*, epoxy (E) and boron nitride nanoparticles (BNs)). The 3D-printed multilayer structures show varying morphology and resolution that can be manipulated *via* polymer-polymer phase separations, ink rheology, layer multiplications, and phase transformation. The phase transformation of UV-curable ink forms patterning sublayers (PLs) with micro-confined inks for the sacrificial sublayers (SLs). These SLs are removable during the selective polymer dissolution process, leading to micropatterns (*i.e.*, arrays of microgrooves) tunable *via* polymer-solvent interaction thermodynamics/kinetics. These micropatterns contain the anisotropic distribution of thermally conductive BNs and confined coolants that form thermally conductive pathways to dissipate heat. This layer additive essence *via* our MDIW also suggests the merits of processing scalability (≈7.35 cm^2/hr) and material flexibility, creating functional morphologies or architectures more quickly and cost-efficiently compared to conventional mask-assisted or vapor-deposited protocols.

5.2 Experimentation and Material Characterization

5.2.1 Materials

Polyethyleneimine with branched molecular structure (molecular weight M_w 25,000, density, 1.05 g/ml, CAS number 25987-06-8) was purchased from Sigma-Aldrich, USA.

The transparent acrylic epoxy (Loctite AA3494, product number 235070) was purchased from Krayden, Inc., USA. BN nanoparticles (500 nm) (99.5%, product number 1523DX) were purchased from Sky Spring Nanomaterials Inc., USA. Ethanol (ACS reagent, 99.5%, CAS number, 64-17-5) and isopropyl alcohol IPA (ACS reagents, natural, ≥98%, FG, CAS number, 67-63-0) were purchased from Sigma-Aldrich, USA.

5.2.2 3D Printing Ink Preparations

The BN nanoparticles were added to the 50 ml of epoxy at different concentrations (5-30 wt.%) to obtain the composite ink as surface patterning (PL) compositions (Table 3). Next, the BNs were added to epoxy while the mixture was mechanically stirred for 2 hr until uniform mixing was obtained. After that, the prepared mixture was evacuated at room temperature for 24 hr to remove bubbles before 3D printing. Lastly, 50 ml of PEI was heated at 50°C inside an oven (model of Lindberg Blue M from Thermo Scientific) as SL material for printing.

Table 3. Ink compositions and sample nomenclature.

Feedstocks	Polymer	BN (wt.%)	Nomenclature
UV-curable patterning layer (PL) material	Epoxy	0	E
		5	E-BN5
		10	E-BN10
		20	E-BN20
		25	E-BN25*
		30	E-BN30
Micropatterned surface with water as a coolant trapped between microchannels for thermal management demonstrations	Epoxy	25	E-BN25C
Non-patterned/planar composite surface as the contrast sample	Epoxy	25	E-BN25P
Wet etchable sacrificial layer (SL) material to facilitate surface patterning formation	Polyethyleneimine	0	PEI

Sacrificial material heated at different temperatures of X °C	Polyethyleneimine	0	PEI-X^

*E-BN25, 25wt.% BN was selected as the optimized loading due to the printability; ^PEI-50, sacrificial material heated at a temperature of 50°C.

5.2.3 MDIW 3D Printing

3D printable inks form multilayered lamellar structures *via* a custom-made 3D printing platform. This 3D printer, MDIW, was in-house developed, consisting of a spinneret, a reducer, a minimizer, and several layer multipliers. The design principles detailed in Figure 27a were modified from our previous publications.[25-27] The printer components were fabricated *via* a metal 3D printer, Concept Laser M2 (GE additive), with metallic powders of Inconel 718 to be mechanically robust and corrosion-resistant during printing. The E-BN25 and PEI heated at a temperature of 50°C (PEI-T50, Table 3) for matching fluid dynamics were loaded into separated stainless-steel syringes and dispensed using syringe pumps (KDS LEGATO 200) at the same flow rate of 1.5 ml/min. Printing paths were guided by computer-aided design (CAD) before being converted into G-code programs by commercial software to control the XYZ motion of the print head. The multilayer structure of E-BN25 and PEI was printed on the glass substrate for all experiments unless otherwise noted. The printed E-BN25 ink was *in situ* crosslinkable while printing on the glass substrate under a UV lamp (*i.e.*, 395-405 nm wavelength). After 3D printing, the printed layered structures were cured within a DYMAX ECE 5000 UV oven (*e.g.*, 325-395 nm) for 30 sec for full solidification. The complete crosslinking networks adhesive to the substrate were critical to avoid structural disruptions during subsequent wet etching. The generated G-code and syringe pump controlled other printing parameters (*e.g.*, print speeds, printing directions, print gap) for optimized patterning structures.

5.2.4 Wet Etching

The ethanol, water, and IPA, as good PEI solvents, were used as etchants. The 3D printed samples were immersed in a bath full of an etchant at different etching temperatures of 25 and 35°C while the bath was magnetically stirred at 100 rpm for different durations of 1, 5, 10, 15, and 20 min. When taken out from the etchant bath, these samples were thoroughly rinsed with the respective etchant and dried on the hot plate (Thermo Scientific) at 50°C for 30 minutes before the subsequent etching cycle. After the solvent evaporation, the weight of the sample was measured by Mettler Toledo microbalance as a function of different etching durations, temperatures, cycles, and etchant types to calculate the dissolution of PEI and estimate etching kinetics.

5.2.5 Material Characterizations

The rheology of E-BN25 and PEI inks was performed using a Discovery HR2 rheometer (TA Instruments) with a 40 mm 2° cone Peltier plate with a 100 µm truncation gap. The viscosity of the samples was measured by flow sweep test from 0.001 to 5000 1/s shear rate. The viscoelastic properties (loss, elastic modulus, and tan delta) were measured by amplitude sweep test from 0.1 to 10000 Pa shear stress at a constant frequency step of 1 Hz. The test geometry temperate was kept at 25°C for E-BN25 ink while the test temperature varied from 25 to 50°C for PEI. The photo-rheology of the sample was tested by irradiating the surface with UV light for 10s, followed by amplitude sweep tests. Thixotropic viscosities were measured at a low shear rate of 0.1 1/s and a high shear rate of 5,10, 25, and 50 1/s.

The SEM images, EDS mapping, and line profile were taken by a field emission scanning electron microscope (FESEM), operated at 20kV with Auriga SEM/FIB (Zeiss).

Before imaging, the sample surface was sputter coated with a thin layer of gold. XRD spectra were obtained from a PAN analytical X'Pert PRO powder diffractometer in the range of 10−70° (2θ). The optical image, 3D surface imaging, and surface roughness of the multilayer structures were taken from the Keyence VR-3200 3D optical scanning microscope. The cross-sectional imaging of the multilayer structures was performed with the OLYMPUS MX-50 optical microscope. The thermal characteristics of the inks were investigated with TGA (TA instruments, TGA 550) and DSC (TA instruments, DSC 250).

The thermal conductivity and thermal diffusivity of the samples were measured with the hot disk TPS-2500S. The through-plane thermal properties were characterized to investigate the effect of composite patterning on the thermal dissipation properties, especially the effects from selective distribution and coolants. The samples with different <32>, <64>, and <128> layers having identical width (*i.e.*, 10 mm), length (*i.e.*, 10 mm), and average thickness (*i.e.*, 350 µm) were heated from 20 to 100°C on DMA Peltier plate (TA instruments). The surface temperature was recorded with the KEITHLEY digital multimeter (DMM7510). Thermal images were captured *via* an infrared camera E8-XT (FLIR) with a 320×240-pixel resolution to analyze the thermal conduction and temperature mapping. Also, to demonstrate the heat dissipation effect of the patterned E-BN25 surfaces depending on the strong convection systems, the thermal images were recorded after heating the sample from 20 to 100°C at a 10°C/min heating rate in the presence of air and trapped water, respectively, on <32> layered samples.

5.3 Results and Discussion

5.3.1 Overview of the Micropatterning Mechanism.

The micropatterning mechanism *via* the MDIW 3D printing and wet etching procedures is shown in Figure 27. The MDIW 3D printing platform was in-house developed (Figure 27a) and synchronously connected with the necessary systems, namely: (i) the transitional control over the printing path *via* G-codes, (ii) the feedstock delivery system *via* separate syringes and syringe pumps, (iii) the patterning system *via* the unique printhead, (iv) the *in situ* curing system *via* a platform-mounted UV source, and (v) the wet etching system within a chemical-filled bath. Among these components, the most critical part was the design of the printhead consisting of a spinneret, a minimizer, a series of multipliers, and a reducer. The MDIW 3D printing was used for fabricating lamellar structures with alternating sublayers of two polymer inks through a sequential layer multiplication process. Once the polymer inks entered different spinneret channels, the minimizer would reduce the flow area for the potential benefits of increasing shear rates, aligning polymer chains/nanoparticles, and maximizing the printing resolution.[36,38] The initial two polymer inks forming two-layer structures in the spinneret would flow through the several layer multipliers, producing from tens to hundreds of individual sublayers within a single printing line. In each layer multipliers, the polymer ink was cut horizontally into two parts, where one part flew and spread into the top channel, and the other part flew and spread into a bottom channel, followed by stacking (Figure 27a_1).

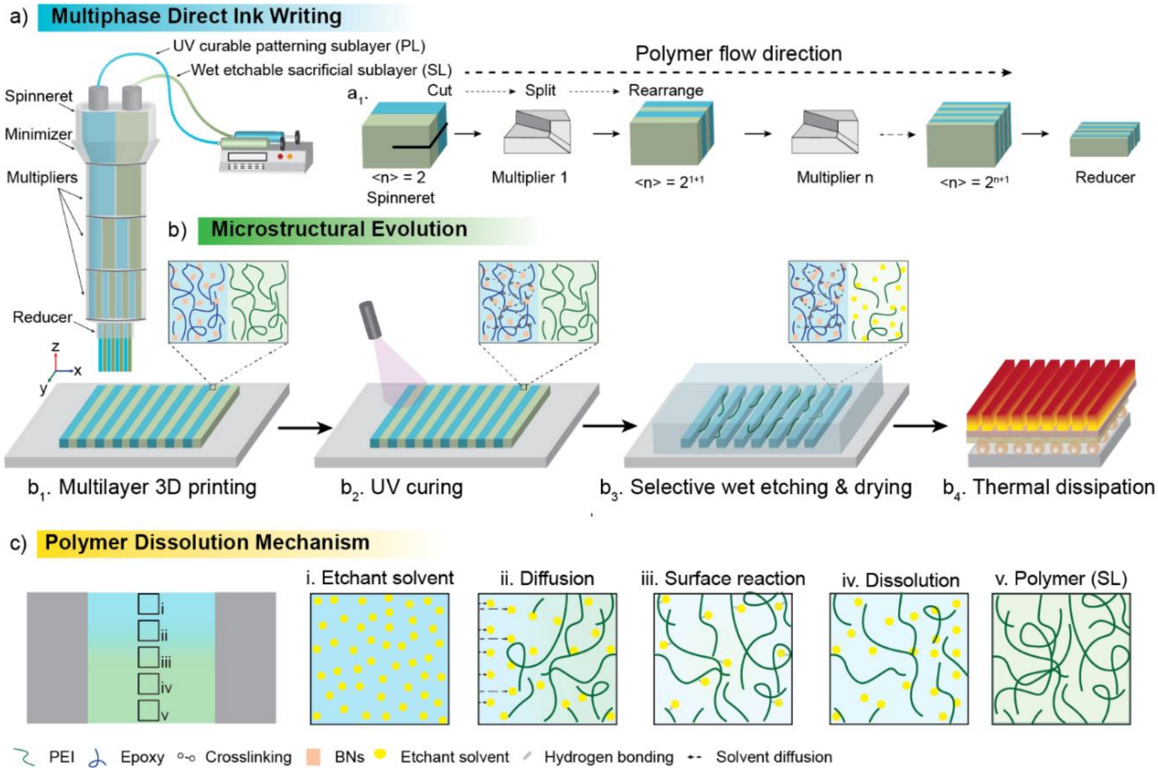

Figure 27. Fabrication strategy for micropatterns with MDIW 3D printing and wet etching. a) Multilayer 3D printing with MDIW demonstrating a_1) the sublayer formation mechanism enabled by printhead components consisting of a spinneret, a minimizer, multipliers, and a reducer, b) the distinct microstructural change in the patterning layer (PL) and sacrificial layer (SL) at different manufacturing stages, such as b_1) 3D printing, b_2) UV curing, b_3) wet etching followed by drying to form permanent patterns, b_4) demonstrating micropatterned surfaces for heat dissipation applications in semiconductor packaging, and c) selective wet etching of SL upon exposure to etchant and its microstructural evolution as a function of time, showing intermediate etching stages between the etchant solvent and SL polymer.

Through this process of splitting, spreading, and stacking, the layer number was doubled by each multiplier. As a result of 2 inks, one multiplier would produce 4 sublayers, 2 multipliers generate 8 sublayers, and *n* multipliers lead to 2^{n+1} sublayers within one printing line exiting the reducer. The reducer dimension (*e.g.*, width, thickness) and shape (*e.g.*, circular, rectangular, triangular, trapezium) were programmable. In this study, the rectangular cross-section was to circumvent voids frequently seen in FDM or DIW 3D printing methods.[57,132] This research has demonstrated layer numbers <n> from <32> to <128>, with a much higher printing speed of ≈16 mm/s than the current state of the art in similar-resolution DIW. Note that our in-house MDIW has been first reported for printing composites as structural supports and stimuli-responsive microbots.[56,189] This study is the novel use of MDIW for micropatterning with standard protocols of 3D printing lamellar structure, phase transformation, and selective wet etching for heat dissipation applications, as demonstrated in Figure 27.

Interdiffusion of inks is a critical issue in multilayer 3D printing because it can cause interfacial distortion, nonuniform layer width, irregular interface, and nonuniform structural thickness. Therefore, to optimize the layer structure, two immiscible inks with distinct chemical compositions and physical morphology were coextruded for multilayer 3D printing. The two feedstock inks (*i.e.*, PEI as the wet etchable SL vs. E-BN composites as the UV-curable PL) were used mainly because of the following reasons. (i) The solvent-free inks (PL and SL) provides flexibility of rheology control for 3D printing processibility and uniform layer formability without interfacial diffusion (Figure 27b$_1$); (ii) the rapid phase transformation of PL allows little time for interfacial instabilities and facilitates fine-resolution lamellar structure formation (Figure 27b$_2$); (iii) the photo-crosslinked PL forms strong adhesion to the substrate (*e.g.*, metal, glass, or plastics), which is essential to retain layers integrity while retaining the mechanical, thermal, and chemical properties when exposed to harsh chemical after wet-etching; (iv) the poor adhesion of SL to the printing substrate guarantees stable etching without damaging the multilayer structure (surface tension ≈70 mN/m for PL and 31.1-28.9 mN/m for SL) and avoids wetting from printing materials;[194–196] (v) the hydrophilic SL enables increased etchability upon etchant exposure (*e.g.*, IPA, ethanol, and water) that could facilitate etching kinetics for precise patterning (Figure 27b_3);[197,198] and (vi) highly loaded BNs in patterning materials enhances heat dissipation for microelectronics applications (Figure 27b_4).[199,200] The understanding of the ink printability, etched surface morphologies, and thermal conductive properties would establish the processing-structure-property relationships for 3D printed micropatterns.

The hybrid chemical and physical properties enable the creation of lamellar microstructure consisting of sublayers of (i) crosslinkable, non-dissolvable PL and (ii) hydrophilic-dissolvable SL, which is a prerequisite for the successful wet etching process. When the lamellar structure is introduced to a good solvent for the SL (not for the PL due to its crosslinking characteristics), the distinct physio-chemical properties would cause selective removal of SL, creating the micropatterns (*i.e.*, microgrooves) after etching. Theoretically, wet etching is a process of polymer dissolution into a solvent that involves a two-step process consisting of (i) solvent diffusion to induce swelling of the polymer network, allowing increased solute mobility, and (ii) chain disentanglement of swollen polymers for dissolution.[201,202] Figure 27c shows the microstructural distribution at the polymer/solvent interface consisting of different segments (*i.e.*, interdiffusion, polymer swelling, and dissolution). The increased mobility of solute would diffuse polymer chains into the surrounding solvent during the wet etching process.[202] The external parameters, such as temperature and agitation, facilitate the polymer dissolution by diffusing etchant molecules and desorbing polymer chains from the swollen polymer gel layer *via* microforces (*i.e.*, van der Waals, centrifugal, and gravitational).[202]

5.3.2 Ink Rheology and 3D Printing Processibility

The rheological properties, such as viscosity, fluid behavior, thixotropic, and viscoelasticity significantly influence the 3D printing of composite ink.[203,204] The expected goals for the MDIW 3D printing of inks include (i) multilayer formation without any interfacial defects (for PL and SL), (ii) reduction of sublayer width to achieve high printing resolution (for PL and SL), and (iii) rapid phase transformation for patterning sublayer of lamellar microstructures after printing on the platform (for PL). For MDIW 3D printing, the inks in the form of polymer solution and the liquid polymer were studied using (i) 20 wt.% polyvinyl alcohol (PVA)/water (PVA20-W) and E, (ii) 22 wt.% cellulose acetate butyrate (CAB)/acetone (CAB22-A) and E, (iii) 30 wt.% halloysite/polyethylene glycol (PEG30-H) and E, and (iv) PEI and E-BN ink. The abbreviations are derived from ink material and ink processing conditions (*e.g.*, filler concentration, solvent, and temperatures). The PVA, CAB, PEG, and PEI were SL materials that displayed good solubility in common solvents, and the PL was E/E-BN. However, polymer solutions, such as PVA20-W/E and CAB22-A/E, revealed interfacial instability due to localized interlayer diffusion of solvents (*i.e.*, water and acetone) from higher (SL) to lower (PL) concentration region at the SL/PL interface. To avoid the solvent molecules' diffusion at SL/PL interface, liquid polymers (*e.g.*, PEG and PEI) were studied as SL compositions. However, the higher wettability of PEG than PEI on the glass substrate caused the spreading of PEI during printing, which prevented the adhesion of the PL sublayer to the substrate (Figure 37). Therefore, the

PEI/E-BN material system was studied and proven with satisfied essential criteria, including material compatibility (during printing), phase separation capability (during printing), and structural stability (after printing).

Figure 28a represents the apparent viscosity of E-BN composite inks with different concentrations of 5-30 wt.% BNs (concentrations confirmed from thermogravimetric analyzer (TGA)) as a function of shear stress. Generally, pure epoxy exhibits Newtonian flow, but adding fillers (*i.e.*, BNs) can generate non-Newtonian properties.[205,206] The composite inks showed an increase in zero shear viscosity from 11 (E) to 76 Pa.s (E-BN 25) due to physical cross-linking between the epoxy molecules and BNs. The magnitude of the shear-thinning behavior (*i.e.*, slope) near the 1 1/s shear rate increased with the higher BNs loading up to 30 wt.%. A slight shear thickening was observed for the ink 10-30 wt.% at a shear rate of less than 0.1 1/s, which may result from the transient yielding of the samples under shear.[207] When the shear rate increased from ≈0.1 to 1 1/s, the viscosity of the composite ink decreased, suggesting the aligned polymer chains and fillers along the shear direction and the decreased molecular entanglement.[208] However, the viscosity stabilized and reached around ≈20-30 Pa.s for a shear rate of 1-100 1/s, within the theoretical shear rate range experienced during the layer formation process.

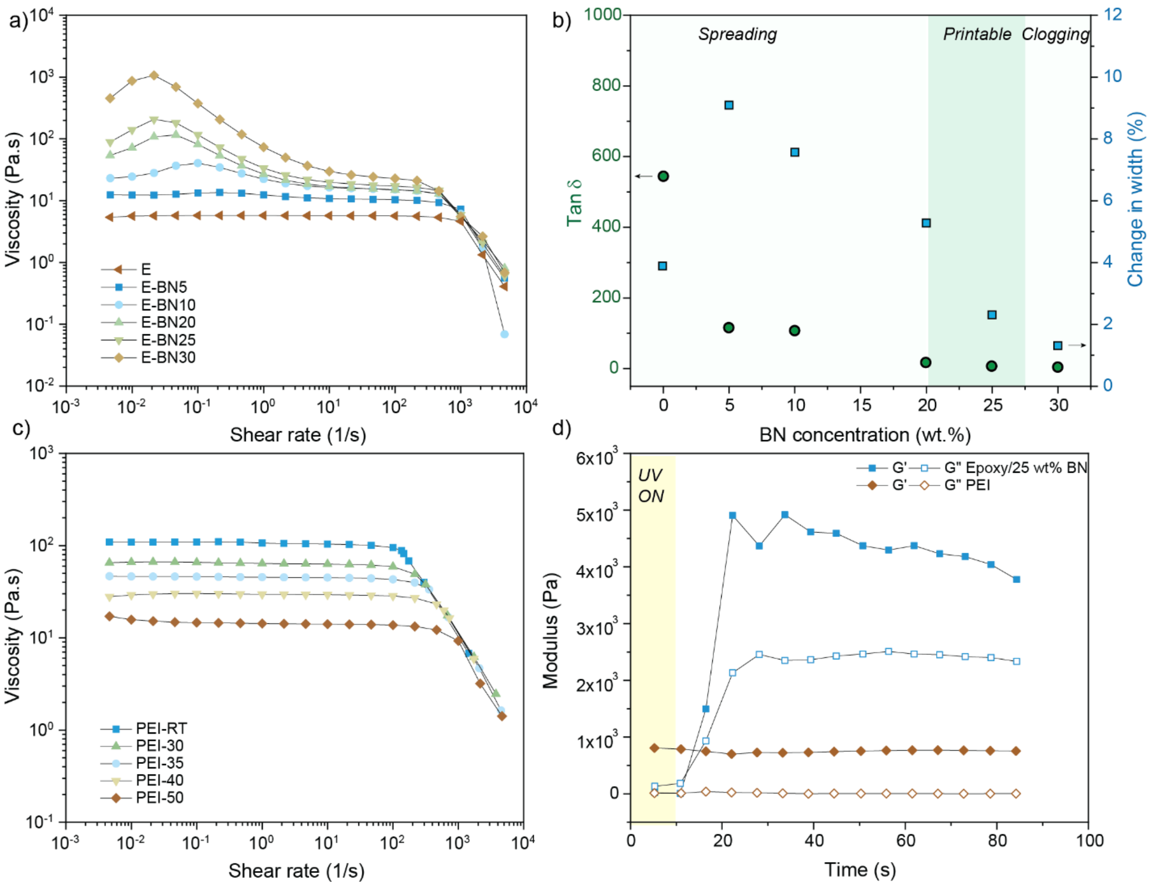

Figure 28. Rheological properties of feedstock inks used for MDIW 3D printing. a) The apparent viscosity of the epoxy ink with and without BNs fillers as a function of the shear rates, b) tan delta (δ) and dimensional change (*i.e.*, the printing line width) of E-BN composite inks containing varying BNs concentrations, c) the apparent viscosity of PEI measured at different temperatures, d) photo-rheology measurements of the evolution of storage modulus (G') and loss modulus (G") during UV light irradiation (light wavelength ≈365 nm and switched off after 10 sec) for both patterning layer (*i.e.*, E-BN25) and sacrificial layer (*i.e.*, PEI-50) samples.

The storage (G') and loss modulus (G") of the inks were investigated for E-BN and PEI inks at different testing ranges of shear rate (0.1-8000 1/s). For both the inks, the loss modulus was higher than the storage modulus, suggesting a dominant viscous behavior (Figure 38). The dominance of loss modulus *(tan delta (G"/G') > 1)* was beneficial for the ink flowability and easy extrusion through the nozzle during the layer multiplication and printing process (Figure 28b).[51,92] The E-BN composite inks containing low BN concentration (<20 wt.%) usually had low viscosity and high tan delta, causing the lateral spreading of 3D printed inks on the printing substrate. On the other hand, the composite ink containing high BN concentration (>30 wt.%) caused clogging of the printing nozzle due to the formation of large aggregates. Hence, the intermediate range of BN concentration, *i.e.*, epoxy-25wt.% BN (E-BN25) as PL material provided optimal rheological properties and 3D printability *via* MDIW. Additionally, the inks should possess thixotropic properties to quickly recover the initial viscosity and thicken to retain the shape of the printed objects after the involvement of shear stress (Figure 39).

Multi-material 3D printing has various challenges, *e.g.*, designing printable ink, interfacial instability, and layer-to-layer nonuniformity. The difference in the viscoelastic characteristics of the coextruding polymers and the presence of organic solvents is a critical contributing factor to the interfacial defects.[209] The weak secondary flow at the interface caused by viscoelastic effects (from the second normal stress differences) has been demonstrated to produce layer nonuniformities during extrusion.[210] Thus, these interfacial instabilities can be reduced or eliminated by matching the viscosity of the inks with the addition of fillers or applying heat to polymers. Thus, to obtain similar viscoelastic properties for PEI as SL and E-BN25 as PL, the PEI was heated from room temperature (RT) to 50°C for proper flow behavior. The apparent viscosity of the PEI gels measured at different temperatures showed that the gel's viscosity decreased due to increased polymer chain movements at higher temperatures (Figure 28c). The PEI-50 (≈17 Pa.s) and E-BN25 (≈20 Pa.s) have a suitable viscosity match at the theoretical shear rate range (*i.e.*, 5-25 1/s). This viscosity matching limited the unfavorable interlayer diffusion at the PEI-50/E-BN25 interface from the time feedstocks combined at the spinneret till the multilayer structure was formed when exiting the MDIW 3D printing nozzle (Figure 40).[192]

The extruded E-BN25 composite ink had phase transformation depending on the photo-viscoelastic characteristics. The photopolymerization kinetics was evaluated with photo-rheology, monitoring the evolution of the storage modules (G') during UV-light irradiation. The liquid-to-solid transition of the ink after the photoirradiation was necessary for the storage modulus to exceed the loss modulus, *i.e.* when the thermomechanical energy was stored elastically than dissipating viscously.[211] Figure 28d shows the high reactivity of acrylic-based epoxy over PEI, confirming their suitability for the MDIW 3D printing and wet etching process. The maximum reactivity of acrylic bonds was attained at ≈20 s, increasing storage modulus by 4-fold, with the gel point (*i.e.*, cross over of modulus (G' and G") obtained within 5 s of UV exposure. Once the E-BN ink exited the nozzle, the rapid phase transformation limited the interlayer diffusion in printed lamellar microstructures. On the other hand, the PEI-50 sublayer remaining unaffected by the UV-curing process was favorable for the subsequent removal during the wet etching process.

5.3.3 Multiphase Sublayer Formability

The superior printability of multi-material polymeric inks can facilitate 3D printed structures with high resolution, complex geometry, assembled nanostructure, and scalable micropatterning. To demonstrate the multi-material printability, the E-BN25 and PEI-50 inks were coextruded into different sublayers through the MDIW printhead, where a white sublayer was E-BN25 and a transparent sublayer was PEI (Figure 29a). The morphology of multilayers was programmable *via* the multiplier number and size. The printed microstructures in Figure 29a$_1$-a$_3$ show alternating sublayers of E-BN25 and PEI-50 with different layer numbers (*e.g.*, <32>, <64>, and <128>). The increase in <n> enabled thinner individual sublayers with curved morphology. The favorable rheological properties of the E-BN25 and PEI-50 inks rendered well-controlled fabrication of multilayer structures with high aspect ratios and fine micron resolutions. The multilayer structures can be printed into a large area of ≈400 cm^2 with an average thickness of ≈350 μm within ≈10 mins. The rapid phase transformation of the printed E-BN25 sublayer by photopolymerization reaction constrained the PEI-50 sublayer between neighboring E-BN25 sublayers, with better regularity in higher <n> numbers (Figure 29a$_4$-a$_6$).

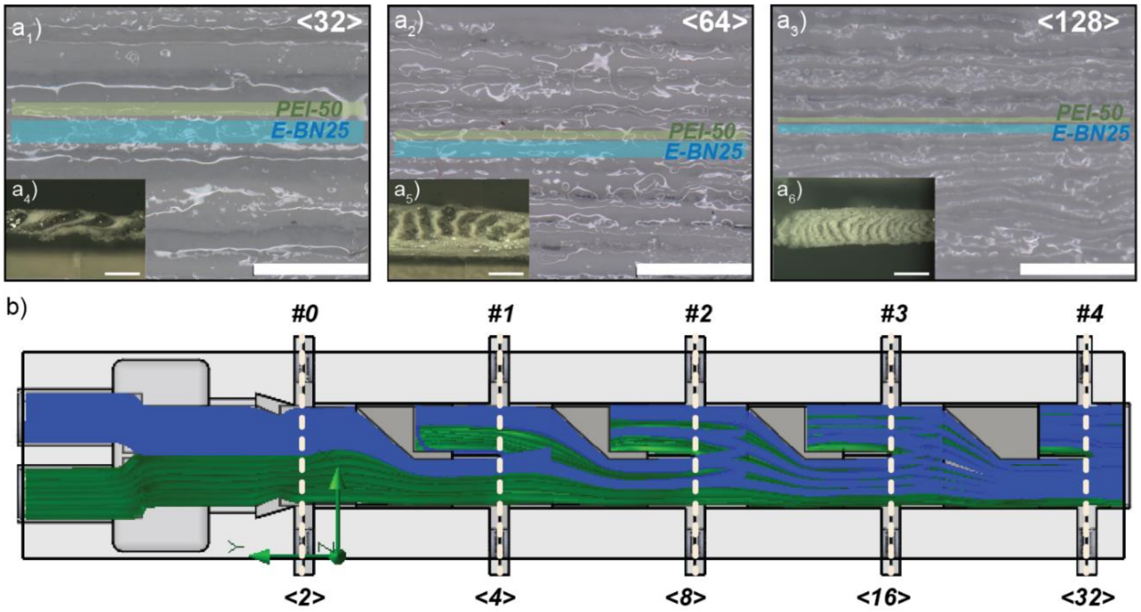

Figure 29. Microstructure of the 3D printed multilayer structures. a$_1$-a$_3$) E-BN25 and PEI-50 with different layer numbers <32>, <64>, and <128> (scale bar 1200 μm). a$_4$-a$_6$) Inset optical images show the cross-sectional morphology of the printed microlayers (scale bar

500 μm), b) computational fluidic dynamic (CFD) simulations of E-BN25 and PEI-50 inks for <32> as an example to show the layer multiplying mechanism (*i.e.*, green sublayer as E-BN25 and blue sublayer as PEI-50.

The computational fluidic dynamic (CFD) simulations were used to understand the layer multiplication and printability process of multimaterial inks at a constant flow rate. Figure 29b shows CFD simulation for layer multiplication mechanism within each multiplier (#n) for the fabrication of <32> layers (*i.e.*, green sublayer as E-BN25 and blue sublayer as PEI-50). The ink with similar viscoelastic properties passed through the #4 layer multiplier where <16> layers multiplied into <32> across the major axis, generating lamellar microstructure with sublayers of E-BN25 and PEI-50 in stacking. Similarly, increasing layer multiplier numbers to #5 and #6 would generate the <64> and <128> layers as used during experimentation. Even though the volumetric flow rate of the inks was equal (1.5 ml/min), the E-BN25/PEI-50 sublayers experienced nonuniform shear stress spanning from the center to the periphery of the print head. This shearing inhomogeneity would cause a slight deviation in the width of individual sublayers (Figure 30a).[209]

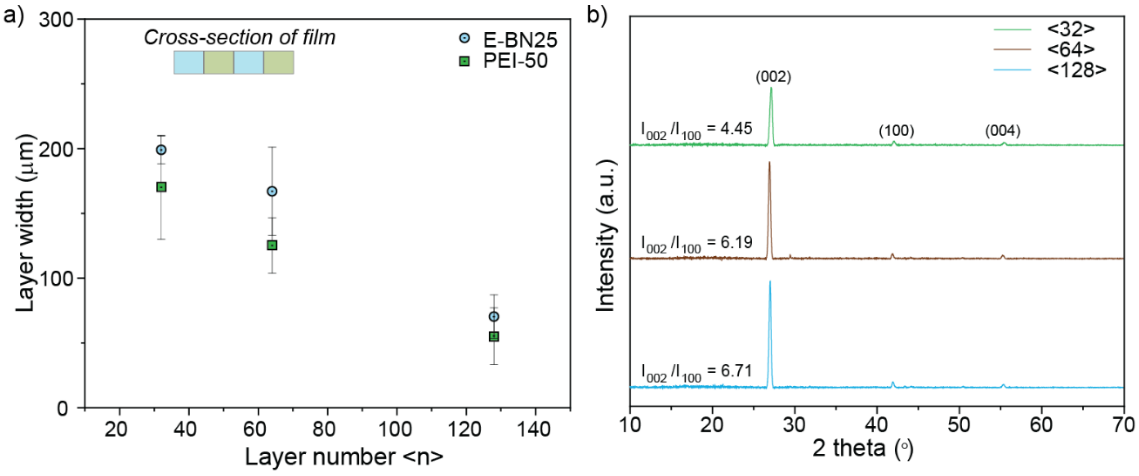

Figure 30. a) dimensions of the E-BN25 and PEI sublayers exhibit consistent layer size evolutions (i.e., width values decrease vs. higher layer numbers), and b) XRD patterns of the E-BN25 multilayer composites with improved BNs orientations as layers multiply.

The average width of PEI-50 and E-BN25 sublayers for <128> are 55 and 70 μm, respectively. The orientation of BNs within the sublayers was explored by XRD patterns with displayed (002), (100), and (004) peaks corresponding to the 27.1, 41.8, and 55.3° (Figure 30b).[212] The intensity of the (002) diffraction peak was much stronger than (100). Generally, a higher intensity ratio between (002) and (100) diffraction peaks (I_{002}/I_{100}) means a higher orientation degree along the in-plane than plane-normal direction.[213,214] The increase in I_{002}/I_{100} intensities ratios with higher layer number, <n>, indicated the improved orientation of BNs due to higher shear stress undergoing between adjacent sublayers.[215]

5.3.4 Etching Kinetics for Surface Micropatterning

A bottom-up MDIW 3D printing was combined with top-down wet etching process to fabricate micropatterns (*i.e.*, microgrooves). A few suitable PEI solvents, including IPA (C_3H_7OH), ethanol (C_2H_5OH), and water (H_2O), were selected as etchants for the E-BN25/PEI-50 multilayer structures to understand the micropatterning kinetics (Figure 31a-f). The hydrogen bonding between the PEI and these etchants was critical for the selective PEI elimination that was not observed for non-hydrogen-bonding solvents, such as acetone ($(CH_3)_2CO$).[216] The polymer etching and microgroove formation mechanism was attributed to the PEI dissolution at the polymer-etchant interface (Figure 27c).[202]

During the etching process, the etchant dissolved the SL composition, and the material flowed from the substrate to the liquid upon agitation. The PEI dissolution percentage (SL material released in the etchant media in the unit of wt%) was measured *via* $((w_i-w_f)/w_i)*100$, where w_i was the initial weight of the sample before etching and w_f was the final weight of the sample after etching. The <32> layered samples were first used as an example to study the etching kinetics (Figure 31a). The PEI dissolution increased as a function of time for all etchants, with the water dissolving PEI faster than ethanol and IPA. Similarly, water behaved as the most interactive solvent with PEI sublayers in <64> and <128> layered structures. The difference in PEI dissolution rates was correlated to (i) the etchant molecular size (*i.e.*, water = 0.28 nm, ethanol = 0.44 nm, and IPA = 0.6 nm), *i.e.*, the smaller the molecular size of the solvent, the faster the diffusion and polymer swelling,[217,218] and (ii) wettability, *i.e.*, the better wettability of the etchants with PEI than E-BN25 would generate a stronger affinity of etchant for faster diffusion.

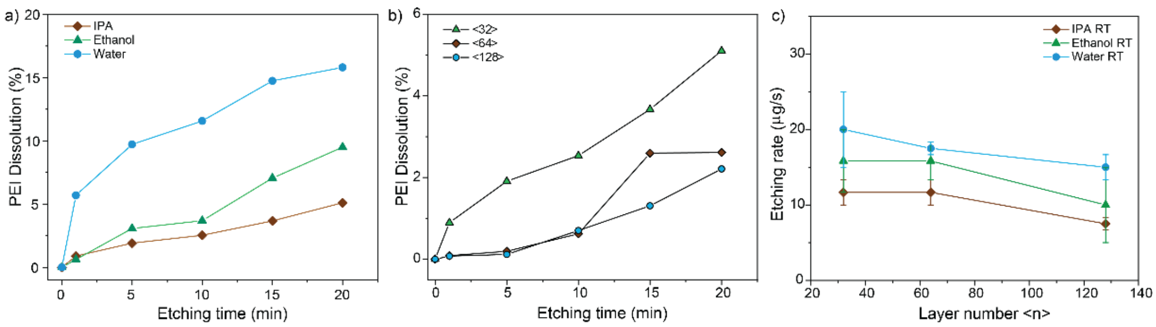

Figure 31. Etching kinetics of E-BN25/PEI-50 multilayer structures. a) PEI sublayer dissolution (%) for <32> by different etchants (*i.e.*, IPA, ethanol, and water) as a function of etching time (min), b) PEI dissolution by IPA etchant at room temperature (RT ≈25°C) for different layer numbers, c) etching rate (µg/s) of PEI sublayer as a function of <n> for different etchants (*i.e.*, IPA, ethanol, and water) and bath temperatures at RT.

As expected, the sublayer of E-BN25 exposed to UV curing showed no etching due to negligible dissolution because of the densely crosslinked structure, consistent with

Figure 28d. However, with the increase in soaking time, the E-BN25 layers were partially or entirely detached from the glass substrate for water and ethanol etchants. This printing layer detachment could be due to more severe water or ethanol diffusion on substrate-layer interfaces, and thus, caused the mechanical failure (consistent with the larger interaction parameter in water and ethanol in Figure 31d). Comparatively, the IPA solvent showed higher structural stability of E-BN25 micropatterns after etching. Thus, the IPA was chosen as a preferential etchant for studying etching kinetics.

The etching rate of SL was expected to depend on a combination of four factors: etchant type, etching temperature, interaction time, and layer number. Therefore, we first investigated the effect of sublayer numbers on the etching rates. The higher <n> (*i.e.*, <64> and <128>) samples showed slower PEI dissolution than the lower <n> (*i.e.*, <32>), which was consistent at different etching periods and temperatures (Figure 31b). The slower etching with the increase of <n> could be attributed to higher resistance to polymer removal due to more confined SL (*i.e.*, by an average of 170, 125, and 55 µm for <32>, <64>, and <128>, respectively, Figure 30a). Moreover, the interfacial interaction area increases of the SL sublayer from 5.25 (for <128>) to 12.75 mm^2 (for <32>) also improved the PEI dissolution rates, as shown in Figure 31b. Here, the interaction area is the top surface area of SL measured from multilayer film. The removal of the PEI SL as a function of etching time led to the formation of the microgroove patterns of different surface roughness values (Figure 41). The material removal for higher sublayer numbers, <n>, was selective, stable, and precise, eventually leading to high-resolution micro features. Polymer dissolution is a thermodynamic phenomenon dependent on temperature. The higher etchant bath temperature (from 25 to 35°C) improved the polymer solubility. As a result, the etching rate consistently increased for samples of different layers (*i.e.*, <32>, <64>, and <128>) that were independent of the etching bath type.

To theoretically understand the mechanism of the polymer etching that involved two transport processes, namely, diffusion and dissolution, the diffusion kinetics relationship $Q = kt^n$ was first generated.[219] Here, Q is the dissolution of SL in the etchant (%), k and n are constant, and t is time (min). The diffusion kinetics relationship for PEI/IPA with <32>, <64>, and <128> layers were fitted as $Q_{<32>} = 0.03t^{0.62}$, $Q_{<64>} = 0.02t^{0.69}$, and $Q_{<128>} = 0.02t^{0.67}$, respectively. The exponent (n) value was fitted as 0.62, 0.69, and 0.67 for layers <32>, <64>, and <128>, respectively, indicating the diffusion of PEI/etchant is a non-Fickian type diffusion.[201] During the non-Fickian diffusion, solvent molecules penetrated through the macro/microvoids formed at the polymer surface and bound to polymer molecules by hydrogen bonding, which led to the expansion and dissolution of the polymer chains.[219,220] Additionally, the Flory-Huggins (FH) interaction parameters between polymer-etchant ($\chi_{polymer/etchant}$) were obtained as $\chi_{PEI/IPA} = 0.56$, $\chi_{PEI/ethanol} = 0.6$, and $\chi_{PEI/water} = 1.3$. This difference suggested the favorable miscibility of PEI in all solvents (*i.e.*, IPA, water, and ethanol) and higher swelling in water and IPA than ethanol, matching experimental observations.

The morphology of the etched micropattern was studied as a function of the interaction between the PEI sublayer and etchant. Figure 32a shows that as the etching time elapsed, the exposed channel width and depth increased, which led to the evolution from narrower/shallower to wider/deeper microgroove regions. For example, the microgroove width of the <128> layered samples increased from ≈80 to 110 μm with an etching time of 1 to 20 min at RT (Figure 32a). At the same time, the groove depth increased from ≈20 to

35 μm under the same condition (Figure 32a). The etching efficiency depended on the thermodynamic parameters (Figure 31) and the confinement effects. Specifically, the PEI sublayer was quickly exposed to the etchant in the <32>. In contrast, the finer E-BN sublayers with curved topology would confine PEI sublayers more robustly in the <64> and <128>, slowing down the dissolution during the etching process. To confirm the selective etching, the EDS in the multilayer samples showed well-controlled removal of the PEI sublayer (Figure 32b) after etching *via* IPA at RT. In addition, the EDS line profile perpendicular to the sublayer texture direction showed a sharp and periodic drop in the boron chemical composition spanning the etched locations (Figure 32c). Figure 32d also represents the cross-sectional morphology of the microgrooves fabricated *via* IPA (RT) etching for different <n> layers, demonstrating the SL etching effectiveness along the in-plane and out-of-plane directions as a function of etching time. The 3D surface topography of etched micropatterns also presented the consistent production of microgrooves with tunable dimensions and surface roughness (Figure 32e).

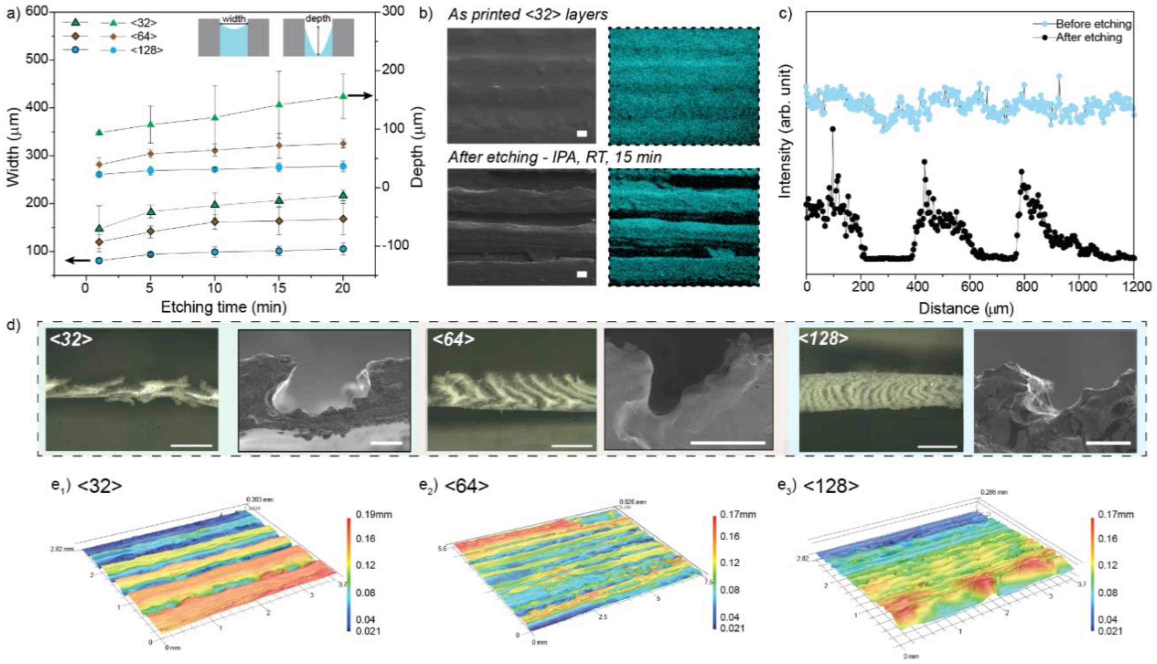

Figure 32. Microstructure evolution of MDIW micropatterns. a) Width and depth plot of micropatterns depending on the etching time for different layer numbers, b) surface EDS mapping of the <32> before and after etching (boron tracing), c) EDS line profile of boron across the patterned surfaces before and after etching, d) optical and SEM images show the cross-sectional view of micropatterns (*i.e.*, microgrooves) fabricated *via* different multiplying/layering after IPA etching at RT (scale bar 500 and 100 μm for optical and SEM, respectively), and the corresponding 3D surface topography of etched samples showing the formation of microgrooves after IPA etching at RT for e_1) <32>, e_2) <64>, and e_3) <128> layers.

5.3.5 Thermal Dissipation Demonstration

The micropattern structures (*e.g.*, channeled microfluidics) were used to demonstrate the heat dissipation efficiency with trapped air or cooling liquids for comparison purposes (Figure 33a). Including BNs in composite microchannels could significantly increase the thermal properties by combining the effect of template design and the selective distribution of NPs. For example, the thermal properties of the E-BN composites were measured, showing a consistent increase in thermal conductivity (K_c) and thermal diffusivity (D_c) with higher BNs concentrations (Figure 33b). The E-BN25 showed the highest thermal property improvement. The filler fraction within the composite microchannels has been no higher than 25 wt.% primarily due to 3D printing processability and to avoid nozzle clogging issues. Quantitatively, the thermal conductivity (K_c) values of E-BN25 micropatterned surfaces were calculated by the parallel models as 0.30, 0.18, and 0.24 W/mK for <32>, <64>, and <128> layers, respectively. However, the experimentally measured values were 0.19, 0.19, and 0.20 W/mK, mainly due to the instrument precision limit and trapped air during the hot disk measurement (Figure 33c). As a result, the difference in K_c was attributed to higher thermal resistance at the substrate/air interface in testing, which would increase the probability of phonon scattering.[221]

Due to the higher surface area (*i.e.*, 185, 164, and 141 mm^2 for <32>, <128>, and <64> respectively), the <32> samples were demonstrated to contain coolants as two-phase heat transfer that occurs in micro or nano-sized passages, making these configurations increasingly essential to provide significant enhancement in heat management capabilities. Several cooling liquids, such as water, oil, and liquid metal (Ga-In-Sn), are commonly used in microelectronics packaging because of their higher heat dissipation efficiency.[222] Theoretical simulations *via* the Finite Element Method (FEM) predicted the average surface temperature and heat flux of E-BN25 <32> micropatterns (air-cooled vs. liquid-cooled). As a result, the fluids with higher heat transfer coefficients showed increased heat transfer from a heated micropatterning surface to fluids, thus lowering the average surface temperatures (*i.e.*, air>oil>water>liquid metal, Figure 33d). Therefore, the water was used to demonstrate the cooling efficiency considering that coolants should be nonflammable, nontoxic, noncorrosive, and inexpensive in the microelectronics industry or computing facility management.

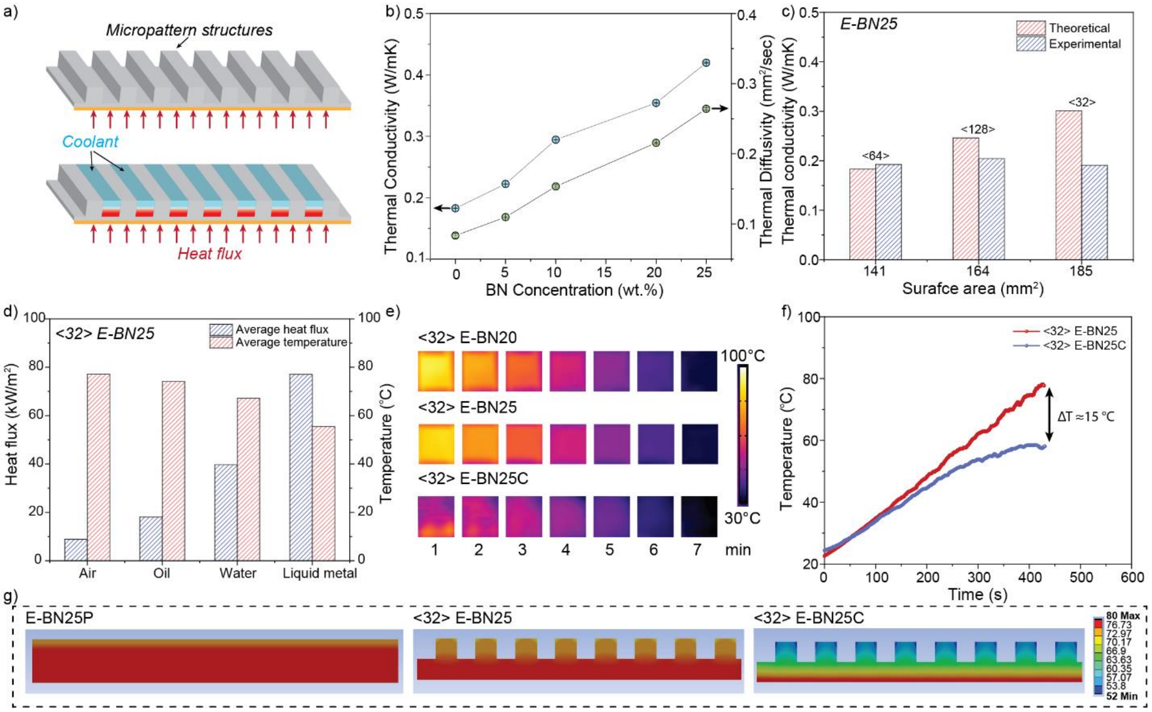

Figure 33. Thermal capability demonstrations. a) The schematic illustration of microgrooves as channeled microfluidic cooling systems, b) measured thermal property (*i.e.*, conductivity, diffusivity) values of the composite as a function of BN concentrations, c) theoretical and experimental thermal conductivity values of E-BN25 for as a function of measured surface area (*i.e.*, <32> layer number exposed the highest surface area due to the shape distortion, as shown in Figure 32d), d) average surface temperature and average heat flux of E-BN25 <32> with air (no coolant) and coolant liquids (*i.e.*, oil, water, and liquid metal) confined between microchannels (as shown in schematic 6a) for <32> samples, e) IR images of composite microchannel surfaces for E-BN20, E-BN25, and E-BN25C, f)

comparison of the surface temperature of E-BN25 and E-BN25C for <32>, and g) simulation results showing the temperature distribution profile for E-BN25P, E-BN25, and E-BN25C without/with the cooling liquids.

The electronics components have been designed to operate over a specified range, *e.g.*, an upper limit of up to 80°C for industrial applications.[223] Therefore, E-BN25 <32> composites with and without water coolant were placed on the same hot stage at 80°C, with an infrared camera used to capture the IR images every 5°C (Figure 33e). A calibrated thermocouple was used to record the real-time sample surface temperature. The surface temperature of the samples without coolant, E-BN25, increased much faster than one with the entrapped coolant, E-BN25C. A temperature difference as significant as ≈15°C demonstrated the superior capability of the E-BN25C composite in heat dissipation (Figure 33f). This difference was also confirmed by simulations, where the average surface temperature of E-BN25 composites with different layer numbers was lowered to 61.32°C (<32>), 60.75 °C (<64>), and 60.27 °C (<128>) from 75.92 °C (<32>), 76.04 °C (<64>), and 75.71°C (<128>), demonstrating high-performance micro cooling systems that can enable faster heat dissipation benefiting conventional heat sink microstructures. The BN nanoparticles within micropatterns are preferentially aligned along the printing direction and interconnected, forming thermal conductive pathways to adjacent coolant regions. The nanoscale heat transfer within a substrate and micro heat exchange between two phases (*i.e.*, substrate and coolant) improved the heat dissipation in the plane direction, and lowered surface temperature in the through-plane direction was observed. The FEM simulation contour mapping also indicated heat accumulation and higher surface temperature for E-BN25 planar than micropattern structures (Figure 33g). By contrast, the trapped cooling agents in E-BN25C can significantly enhance the heat transfer along the out-of-plane direction without much heat accumulation (Figure 33g). Besides, E-BN25 micropattern structure exhibit superior electrically insulating property. Thus, a thermally conductive but electrically insulating film is supposed to be an efficient thermal management structure to conduct the heat from electronic components to the environment, improving the components' efficiency and lifespan.

5.4 Conclusion

In summary, we have demonstrated a novel technique combining unique 3D printing (i.e., MDIW) and wet etching to create micropatterns (i.e., an array of micro-grooves). The in-house developed MDIW was used to fabricate the lamellar structure with alternating sublayers of UV-curable PL and wet-etchable SL. The morphology (i.e., layer number and width) of multilayer 3D printed structures were fabricated by controlling the polymer composition, particle loading, ink viscoelasticity, phase transformation, shear stress, and extrusion rates. The rapid phase transformation of PL retained the printed microstructures and enabled "micro-confinement" of SL for subsequent wet etching. As a result, the printed multilayer structures had well-controlled sublayer dimensions, ranging from ≈50 to 200 μm depending on the layer multiplying procedures. The selective dissolution of SL formed the micropatterns due to polymer-solvent interdiffusion during the wet-etching process. The etching kinetics (e.g., time, temperature, interaction parameters), pattern microstructures, and etchant types significantly influenced the micropatterning geometries and morphologies. Besides, the micropatterned surfaces with confined BNs-enabled thermally conductive behaviors and micropattern-contained liquid coolant further increased heat dissipation efficiency. The polymer-polymer and polymer-solvent interaction phenomena helped multilayer printability and micropatterning via controlled polymer dissolution to establish the processing-structure-property relationship. Our micropatterning technique opens a new pathway that enables the fabrication of hierarchical structures through a printing-solvent-free, maskless, scalable, and cost-effective process compared to conventional patterning protocols. MDIW 3D printing also shows high compatibility with various polymeric and metallic inks, suggesting possibilities to design mechanical, thermal, electrical, optical, and magnetic properties for broad applications.

[164] B. Bharti, A.-L. Fameau, M. Rubinstein, O. D. Velev, *Nature Mater* **2015**, *14*, 1104.

[165] M. R. Jones, K. D. Osberg, R. J. Macfarlane, M. R. Langille, C. A. Mirkin, *Chem. Rev.* **2011**, *111*, 3736.

[166] Y. Choi, Y. Song, Y. T. Kim, S. J. Lee, K. G. Lee, S. G. Im, *ACS Appl. Mater. Interfaces* **2021**, *13*, 3098.

[167] Y. Kim, T. Kim, J. Lee, Y. S. Choi, J. Moon, S. Y. Park, T. H. Lee, H. K. Park, S. A. Lee, M. S. Kwon, H. Byun, J. Lee, M. Lee, B. H. Hong, H. W. Jang, *Adv. Mater.* **2021**, *33*, 2004827.

[168] I. Topolniak, A. M. Elert, X. Knigge, G. C. Ciftci, J. Radnik, H. Sturm, *Advanced Materials* **2022**, *34*, 2109509.

[169] P. Li, X. Dou, H. Schönherr, *Polym. Int.* **2019**, *68*, 1015.

[170] G. G. Yang, H. J. Choi, K. H. Han, J. H. Kim, C. W. Lee, E. I. Jung, H. M. Jin, S. O. Kim, *ACS Appl. Mater. Interfaces* **2022**, *14*, 12011.

[171] W. Jung, S. Jang, S. Cho, H. Jeon, H. Jung, *Adv. Mater.* **2020**, *32*, 1907101.

[172] J. A. Rogers, H. H. Lee, *Unconventional Nanopatterning Techniques and Applications*, John Wiley & Sons, Inc., Hoboken, NJ, USA, **2008**.

[173] H. Puliyalil, U. Cvelbar, *Nanomaterials* **2016**, *6*, 108.

[174] L. Zhang, Y. Liu, Z. Li, W. Wang, *Micromachines* **2018**, *9*, 162.

[175] D. Kwak, J. A. Lim, B. Kang, W. H. Lee, K. Cho, *Adv. Funct. Mater.* **2013**, *23*, 5224.

[176] B.-J. de Gans, S. Hoeppener, U. S. Schubert, *Adv. Mater.* **2006**, *18*, 910.

[177] B. Bao, J. Jiang, F. Li, P. Zhang, S. Chen, Q. Yang, S. Wang, B. Su, L. Jiang, Y. Song, *Adv. Funct. Mater.* **2015**, *25*, 3286.

[178] S. Jambhulkar, W. Xu, R. Franklin, D. Ravichandran, Y. Zhu, K. Song, *J. Mater. Chem. C* **2020**, *8*, 9495.

[179] D. Ahn, L. M. Stevens, K. Zhou, Z. A. Page, *ACS Cent. Sci.* **2020**, *6*, 1555.

[180] B. E. Kelly, I. Bhattacharya, H. Heidari, M. Shusteff, C. M. Spadaccini, H. K. Taylor, *Science* **2019**, *363*, 1075.

[181] S. Coelho, J. Baek, J. Walsh, J. Justin Gooding, K. Gaus, *Nat Commun* **2022**, *13*, 647.

[182] A. Reiser, M. Lindén, P. Rohner, A. Marchand, H. Galinski, A. S. Sologubenko, J. M. Wheeler, R. Zenobi, D. Poulikakos, R. Spolenak, *Nat Commun* **2019**, *10*, 1853.

[183] J.-U. Park, M. Hardy, S. J. Kang, K. Barton, K. Adair, D. kishore Mukhopadhyay, C. Y. Lee, M. S. Strano, A. G. Alleyne, J. G. Georgiadis, P. M. Ferreira, J. A. Rogers, *Nature Mater* **2007**, *6*, 782.

[184] W. Jung, Y.-H. Jung, P. V. Pikhitsa, J. Feng, Y. Yang, M. Kim, H.-Y. Tsai, T. Tanaka, J. Shin, K.-Y. Kim, H. Choi, J. Rho, M. Choi, *Nature* **2021**, *592*, 54.

[185] W. Su, B. S. Cook, Y. Fang, M. M. Tentzeris, *Sci Rep* **2016**, *6*, 35111.

[186] W. Xu, S. Jambhulkar, Y. Zhu, D. Ravichandran, M. Kakarla, B. Vernon, D. G. Lott, J. L. Cornella, O. Shefi, G. Miquelard-Garnier, Y. Yang, K. Song, *Composites Part B: Engineering* **2021**, *223*, 109102.

[187] W. Xu, S. Jambhulkar, D. Ravichandran, Y. Zhu, M. Kakarla, Q. Nian, B. Azeredo, X. Chen, K. Jin, B. Vernon, D. G. Lott, J. L. Cornella, O. Shefi, G. Miquelard-Garnier, Y. Yang, K. Song, *Small* **2021**, *17*, 2100817.

[188] B. Elder, R. Neupane, E. Tokita, U. Ghosh, S. Hales, Y. L. Kong, *Adv. Mater.* **2020**, *32*, 1907142.

[189] D. Ravichandran, W. Xu, M. Kakarla, S. Jambhulkar, Y. Zhu, K. Song, *Additive Manufacturing* **2021**, *47*, 102322.

[190] W. Xu, D. Ravichandran, S. Jambhulkar, Y. Zhu, K. Song, *Adv. Funct. Mater.* **2021**, *31*, 2009311.

[191] W. Xu, R. Franklin, D. Ravichandran, M. Bawareth, S. Jambhulkar, Y. Zhu, M. Kakarla, F. Ejaz, B. Kwon, M. K. Hassan, M. Al-Ejji, A. Asadi, N. Chawla, K. Song, *Adv Funct Materials* **2022**, 2204731.

[192] D. Ravichandran, W. Xu, M. Kakarla, S. Jambhulkar, Y. Zhu, K. Song, *Additive Manufacturing* **2021**, *47*, 102322.

[193] M. G. Rasul, M. Cheng, Y. Jiang, Y. Pan, R. Shahbazian-Yassar, *ACS Nanosci. Au* **2022**, *2*, 297.

[194] K. Grundke, S. Michel, M. Osterhold, *Progress in Organic Coatings* **2000**, *39*, 101.

[195] I. C. Bellettini, R. Eising, A. C. Felippe, J. B. Domingos, E. Minatti, V. G. Machado, *Química Nova* **2015**, DOI 10.5935/0100-4042.20150085.

[196] J. Penfold, I. Tucker, R. K. Thomas, D. J. F. Taylor, J. Zhang, X. L. Zhang, *Langmuir* **2007**, *23*, 3690.

[197] M. Y. Lee, J. H. Lee, J. W. Chung, S.-Y. Kwak, *Journal of Environmental Management* **2018**, *206*, 740.

[198] N. Uzal, N. Ates, S. Saki, Y. E. Bulbul, Y. Chen, *Separation and Purification Technology* **2017**, *187*, 118.

[199] T. Wang, G. Zhang, B. Zhang, S. Liu, D. Li, C. Liu, *ACS Appl. Nano Mater.* **2021**, *4*, 4153.

[200] J. Han, G. Du, W. Gao, H. Bai, *Adv. Funct. Mater.* **2019**, *29*, 1900412.

[201] *Encapsulation Technologies for Electronic Applications*, Elsevier, **2019**.

[202] B. A. Miller-Chou, J. L. Koenig, *Progress in Polymer Science* **2003**, *28*, 1223.

[203] M. Schaffner, P. A. Rühs, F. Coulter, S. Kilcher, A. R. Studart, *Sci. Adv.* **2017**, *3*, eaao6804.

[204] S. Zhao, G. Siqueira, S. Drdova, D. Norris, C. Ubert, A. Bonnin, S. Galmarini, M. Ganobjak, Z. Pan, S. Brunner, G. Nyström, J. Wang, M. M. Koebel, W. J. Malfait, *Nature* **2020**, *584*, 387.

[205] M. Cheng, A. Ramasubramanian, M. G. Rasul, Y. Jiang, Y. Yuan, T. Foroozan, R. Deivanayagam, M. Tamadoni Saray, R. Rojaee, B. Song, V. R. Yurkiv, Y. Pan, F. Mashayek, R. Shahbazian-Yassar, *Adv. Funct. Mater.* **2021**, *31*, 2006683.

[206] K. Shen, J. Ding, S. Yang, *Adv. Energy Mater.* **2018**, *8*, 1800408.

[207] O. D. Yirmibesoglu, L. E. Simonsen, R. Manson, J. Davidson, K. Healy, Y. Menguc, T. Wallin, *Commun Mater* **2021**, *2*, 82.

[208] H. Yuk, B. Lu, S. Lin, K. Qu, J. Xu, J. Luo, X. Zhao, *Nat Commun* **2020**, *11*, 1604.

[209] J.-F. Agassant, Y. Demay, *Polymers* **2022**, *14*, 1309.

[210] B. Lu, H. Zhang, A. Maazouz, K. Lamnawar, *Polymers* **2021**, *13*, 417.

[211] A. Cortés, A. Cosola, M. Sangermano, M. Campo, S. González Prolongo, C. F. Pirri, A. Jiménez-Suárez, A. Chiappone, *Adv. Funct. Mater.* **2021**, *31*, 2106774.

[212] V. Guerra, C. Wan, V. Degirmenci, J. Sloan, D. Presvytis, T. McNally, *Nanoscale* **2018**, *10*, 19469.

[213] Z. Lin, Y. Liu, S. Raghavan, K. Moon, S. K. Sitaraman, C. Wong, *ACS Appl. Mater. Interfaces* **2013**, *5*, 7633.

[214] G. Han, D. Zhang, C. Kong, B. Zhou, Y. Shi, Y. Feng, C. Liu, D.-Y. Wang, *Chemical Engineering Journal* **2022**, *437*, 135482.

[215] B. Zhong, J. Zou, L. An, C. Ji, X. Huang, W. Liu, Y. Yu, H. Wang, G. Wen, K. Zhao, X. Lin, *Composites Part A: Applied Science and Manufacturing* **2019**, *127*, 105629.

[216] M.-X. Du, Y.-F. Yuan, J.-M. Zhang, C.-Y. Liu, *Macromolecules* **2022**, *55*, 4578.

[217] T. C. Chan, H. T. Li, K. Y. Li, *J. Phys. Chem. B* **2015**, *119*, 15718.

[218] T. P. Gall, R. C. Lasky, E. J. Kramer, *Polymer* **1990**, *31*, 1491.

[219] C. F. Jasso-Gastinel, in *Modification of Polymer Properties*, Elsevier, **2017**, pp. 185–210.

[220] L. Baij, J. J. Hermans, K. Keune, P. D. Iedema, *Macromolecules* **2018**, *51*, 7134.

[221] J. R. Harter, T. S. Palmer, P. A. Greaney, in *Advances in Heat Transfer*, Elsevier, **2020**, pp. 335–488.

[222] S. M. Sohel Murshed, C. A. Nieto de Castro, *Renewable and Sustainable Energy Reviews* **2017**, *78*, 821.

[223] V. G. Pastukhov, Yu. F. Maidanik, C. V. Vershinin, M. A. Korukov, *Applied Thermal Engineering* **2003**, *23*, 1125.

CHAPTER 6

SUMMARY AND FUTURE OUTLOOK

In conclusion, this dissertation discusses hybrid nanomanufacturing via combining 3D printing and dispersion-mediated deposition for microscale surface patterning and nanoscale particle alignment. The 3D-printed templates fabricated by SLA, μCLIP, and FDM with microscale patterns acted as anchoring sites that allowed the deposition of 1D CNF and 2D MXene NPs at predetermined locations from the nanoparticle dispersions. The assembled NPs displayed the scalable micropatterning with the nanoscale assembly into anisotropic microstructures. Moreover, in Chapter 4, the MDIW 3D printing generated high aspect-ratio boron nitride micropatterns by selective etching of the sacrificial layer. These micropatterns displayed electrical and thermal conductivity, chemical sensitivity, and mechanical durability for application as multifunctional sensors and heat exchangers. The use of hybrid manufacturing showed the general application to assemble various NPs into scalable structures without the limit of sample size and a high level of autonomy.

So far, we have demonstrated 2D surface micropatterning of nanoparticles and this hybrid approach can be extended to the self-assembly of nanoparticles into 3D architectures. The advancement of the 3D printing approach can be utilized for the printing of complex 3D pattern templates (e.g., circular, triangular, square, and hexagonal honeycomb structures) that can mimic biological systems. However, this approach adds structural complexity for efficient NP assembly. Thus, using a closed microchannel-based fluidic deposition approach would be highly beneficial to allow the self-assembly of various NPs (e.g., zinc sulfide, cadmium sulfide nanorods, and lead sulfide nanosheets) into 3D patterns (e.g. concentric rings, stripes, dots) through nanoparticle-substrate interaction. Three-dimensional control over the placement of different types of nanoparticles (0D, 1D, and 2D) on various polymeric 3D-printed substrates for advanced applications (e.g., optoelectronics, catalysis, sensing, and biomedical) as well as for industrialization would be the focus of this study.

Additionally, multi-material patterning techniques for the creation of a device with well-controlled morphology, multi-functionality, and functional complexity remain unexplored. The different sizes, morphology, and properties of NPs would require the combination of different assembly and printing technologies for the production of complex printed structures for microelectronics applications. For example, the reported MDIW technique for micropatterning or μCLIP 3D printing approach can be utilized for the fabrication of high-resolution templates. On the top of the patterned template, nanoparticles such as gold (Au) nanostars/ silver (Ag) nanorods can be deposited by suspension-based deposition approaches like dip coating and microfluidics for unidirectional assembly generating the structure with multi-material patterns (as discussed in Chapter 3 and 5). The Ag-Au micropattern with well-aligned morphologies is necessary to enhance the polarization/optical properties with narrower plasmon resonance for future optoelectronic applications.

Lastly, the resolution of assembled NPs micropatterns depends on 3D printed template resolution. So far, tens of micron-resolution micropatterns were fabricated via the MDIW 3D printing and wet etching technique. However, the dimensions, roughness, and stability of MDIW micropatterns can be further improved to a sub-micron scale by optimizing the rheological properties of patterning materials. The properties like high solidus modulus as well as viscosity, shear thinning behavior, and thixotropy will require attention to achieve the desired flow properties and pattern quality. Additionally, 3D patterns e.g., criss-cross and squares can be fabricated by controlled multilayer 3D printing in an out-of-plane direction.

REFERENCES

[1] N. Baig, I. Kammakakam, W. Falath, *Mater. Adv.* **2021**, *2*, 1821.

[2] R. Kassing, P. Petkov, W. Kulisch, C. Popov, Eds., *Functional Properties of Nanostructured Materials*, Springer Netherlands, Dordrecht, **2006**.

[3] K. Shin, Y. Song, Y. Goh, K. Lee, *IJMS* **2019**, *20*, 1424.

[4] P. Wang, C. Jia, Y. Huang, X. Duan, *Matter* **2021**, *4*, 552.

[5] Z. Tang, N. A. Kotov, *Adv. Mater.* **2005**, *17*, 951.

[6] Z.-M. Dang, M.-S. Zheng, J.-W. Zha, *Small* **2016**, *12*, 1688.

[7] J. Petrovic, D. Bekric, I. Vujicic, I. Dimic, S. Putic, *Acta per tech* **2013**, 151.

[8] P. Su Shin, J. Hyun Kim, H. S. Park, Y. Min Baek, D. Jun Kwon, K. L. DeVries, J. Man Park, *J Powder Metall Min* **2017**, *06*, DOI 10.4172/2168-9806.1000169.

[9] H. Bark, M. W. M. Tan, G. Thangavel, P. S. Lee, *Adv. Energy Mater.* **2021**, *11*, 2101387.

[10] S. Salimian, M. Montazer, A. S. Rashidi, N. Soleimani, A. Bashiri Rezaie, *J of Applied Polymer Sci* **2021**, *138*, 51357.

[11] R. Shenhar, T. B. Norsten, V. M. Rotello, *Adv. Mater.* **2005**, *17*, 657.

[12] D. Karnaushenko, T. Kang, V. K. Bandari, F. Zhu, O. G. Schmidt, *Adv. Mater.* **2020**, *32*, 1902994.

[13] M. P. Nikitin, T. A. Zdobnova, S. V. Lukash, O. A. Stremovskiy, S. M. Deyev, *Proc. Natl. Acad. Sci. U.S.A.* **2010**, *107*, 5827.

[14] I. U. Arachchige, S. L. Brock, *Acc. Chem. Res.* **2007**, *40*, 801.

[15] C. Mavroidis, A. Ferreira, C. Mavroidis, Eds., *Nanorobotics: Current Approaches and Techniques*, Springer, New York, **2013**.

[16] B. Wang, D. Liu, Y. Liao, Y. Huang, M. Ni, M. Wang, Z. Ma, Z. Wu, Y. Lu, *ACS Nano* **2022**, acsnano.2c08626.

[17] L. Zhang, F. Gu, J. Chan, A. Wang, R. Langer, O. Farokhzad, *Clin Pharmacol Ther* **2008**, *83*, 761.

[18] S. Jiang, K. Y. Win, S. Liu, C. P. Teng, Y. Zheng, M.-Y. Han, *Nanoscale* **2013**, *5*, 3127.

[19] M. C. Roco, *Current Opinion in Biotechnology* **2003**, *14*, 337.

[20] K. Thorkelsson, P. Bai, T. Xu, *Nano Today* **2015**, *10*, 48.

[21] M. A. Boles, M. Engel, D. V. Talapin, *Chem. Rev.* **2016**, *116*, 11220.

[22] A. Sánchez-Iglesias, M. Grzelczak, T. Altantzis, B. Goris, J. Pérez-Juste, S. Bals, G. Van Tendeloo, S. H. Donaldson, B. F. Chmelka, J. N. Israelachvili, L. M. Liz-Marzán, *ACS Nano* **2012**, *6*, 11059.

[23] S. F. Tan, S. W. Chee, G. Lin, U. Mirsaidov, *Acc. Chem. Res.* **2017**, *50*, 1303.

[24] T. Udayabhaskararao, T. Altantzis, L. Houben, M. Coronado-Puchau, J. Langer, R. Popovitz-Biro, L. M. Liz-Marzán, L. Vuković, P. Král, S. Bals, R. Klajn, *Science* **2017**, *358*, 514.

[25] A. Dong, J. Chen, P. M. Vora, J. M. Kikkawa, C. B. Murray, *Nature* **2010**, *466*, 474.

[26] K. Kim, H. S. Han, I. Choi, C. Lee, S. Hong, S.-H. Suh, L. P. Lee, T. Kang, *Nat Commun* **2013**, *4*, 2182.

[27] L. Song, B. B. Xu, Q. Cheng, X. Wang, X. Luo, X. Chen, T. Chen, Y. Huang, *Sci. Adv.* **2021**, *7*, eabk2852.

[28] X. Fu, J. Cai, X. Zhang, W.-D. Li, H. Ge, Y. Hu, *Advanced Drug Delivery Reviews* **2018**, *132*, 169.

[29] M. Drost, F. Tu, L. Berger, C. Preischl, W. Zhou, H. Gliemann, C. Wöll, H. Marbach, *ACS Nano* **2018**, *12*, 3825.

[30] H. Ding, Q. Zhang, H. Gu, X. Liu, L. Sun, M. Gu, Z. Gu, *Adv. Funct. Mater.* **2020**, *30*, 1901760.

[31] J. Ahn, S. Hong, Y.-S. Shim, J. Park, *Applied Sciences* **2020**, *10*, 8780.

[32] R. Šakalys, K. W. Kho, T. E. Keyes, *Sensors and Actuators B: Chemical* **2021**, *340*, 129970.

[33] N. Chiang, L. Scarabelli, G. A. Vinnacombe-Willson, L. A. Pérez, C. Dore, A. Mihi, S. J. Jonas, P. S. Weiss, *ACS Materials Lett.* **2021**, *3*, 282.

[34] W. Zhang, Y. Lei, F. Ming, Q. Jiang, P. M. F. J. Costa, H. N. Alshareef, *Adv. Energy Mater.* **2018**, *8*, 1801840.

[35] A. Garg, W. Nam, W. Zhou, *ACS Appl. Mater. Interfaces* **2020**, *12*, 56290.

[36] F. Pfeiffer, N. M. Felix, C. Neuber, C. K. Ober, H.-W. Schmidt, *Adv. Funct. Mater.* **2007**, *17*, 2336.

[37] M. Obst, G. Arnauts, A. J. Cruz, M. Calderon Gonzalez, K. Marcoen, T. Hauffman, R. Ameloot, *Angewandte Chemie Intl Edit* **2021**, *60*, 25668.

[38] J. Zhang, Y. Li, K. Cao, R. Chen, *Nanomanuf Metrol* **2022**, *5*, 191.

[39] N. A. Abu Hatab, J. M. Oran, M. J. Sepaniak, *ACS Nano* **2008**, *2*, 377.

[40] F. Demami, L. Pichon, R. Rogel, A. C. Salaün, *IOP Conf. Ser.: Mater. Sci. Eng.* **2009**, *6*, 012014.

[41] D. Zhao, B. Chang, M. Beleggia, *ACS Appl. Mater. Interfaces* **2020**, *12*, 6436.

[42] S. Jambhulkar, S. Liu, P. Vala, W. Xu, D. Ravichandran, Y. Zhu, K. Bi, Q. Nian, X. Chen, K. Song, *ACS Nano* **2021**, *15*, 12057.

[43] S. Kiruthika, B. Radha, *ACS Omega* **2020**, *5*, 20739.

[44] F. Yang, P. Li, X. Li, L. Huo, J. Chen, R. Chen, W. Na, W. Tang, L. Liang, W. Su, *Applied Surface Science* **2013**, *274*, 241.

[45] C. M. Thakar, S. S. Parkhe, A. Jain, K. Phasinam, G. Murugesan, R. J. M. Ventayen, *Materials Today: Proceedings* **2022**, *51*, 842.

[46] W. Xu, S. Jambhulkar, Y. Zhu, D. Ravichandran, M. Kakarla, B. Vernon, D. G. Lott, J. L. Cornella, O. Shefi, G. Miquelard-Garnier, Y. Yang, K. Song, *Composites Part B: Engineering* **2021**, *223*, 109102.

[47] M. Manoj Prabhakar, A. K. Saravanan, A. Haiter Lenin, I. Jerin leno, K. Mayandi, P. Sethu Ramalingam, *Materials Today: Proceedings* **2021**, *45*, 6108.

[48] S. Park, W. Shou, L. Makatura, W. Matusik, K. (Kelvin) Fu, *Matter* **2022**, *5*, 43.

[49] R. Ranjan, D. Kumar, M. Kundu, S. Chandra Moi, *Materials Today: Proceedings* **2022**, *61*, 43.

[50] A. M. E. Arefin, N. R. Khatri, N. Kulkarni, P. F. Egan, *Polymers* **2021**, *13*, 1499.

[51] J. A. Lewis, *Adv. Funct. Mater.* **2006**, *16*, 2193.

[52] D. E. Yunus, W. Shi, S. Sohrabi, Y. Liu, *Nanotechnology* **2016**, *27*, 495302.

[53] Y. Yang, X. Li, M. Chu, H. Sun, J. Jin, K. Yu, Q. Wang, Q. Zhou, Y. Chen, *Sci. Adv.* **2019**, *5*, eaau9490.

[54] J. J. Martin, B. E. Fiore, R. M. Erb, *Nat Commun* **2015**, *6*, 8641.

[55] A. Al Rashid, W. Ahmed, M. Y. Khalid, M. Koç, *Additive Manufacturing* **2021**, *47*, 102279.

[56] D. Ravichandran, R. J. Ahmed, R. Banerjee, M. Ilami, H. Marvi, G. Miquelard-Garnier, Y. Golan, K. Song, *J. Mater. Chem. C* **2022**, 10.1039.D2TC01109C.

[57] H. Guo, H. Zhao, H. Niu, Y. Ren, H. Fang, X. Fang, R. Lv, M. Maqbool, S. Bai, *ACS Nano* **2021**, *15*, 6917.

[58] R. Kumar, R. Singh, M. Singh, P. Kumar, *Journal of Thermoplastic Composite Materials* **2020**, 089270572092511.

[59] J. Orangi, F. Hamade, V. A. Davis, M. Beidaghi, *ACS Nano* **2020**, *14*, 640.

[60] W. Yang, J. Yang, J. J. Byun, F. P. Moissinac, J. Xu, S. J. Haigh, M. Domingos, M. A. Bissett, R. A. W. Dryfe, S. Barg, *Adv. Mater.* **2019**, *31*, 1902725.

[61] Y. Zhang, L. Wu, M. Zou, L. Zhang, Y. Song, *Advanced Materials* **2022**, *34*, 2107249.

[62] S. F. Busch, M. Weidenbach, M. Fey, F. Schäfer, T. Probst, M. Koch, *J Infrared Milli Terahz Waves* **2014**, *35*, 993.

[63] X. You, Q. Zhang, J. Yang, S. Dong, *Composites Part A: Applied Science and Manufacturing* **2023**, *167*, 107420.

[64] M.-S. Scholz, B. W. Drinkwater, R. S. Trask, *Ultrasonics* **2014**, *54*, 1015.

[65] J. Huang, V. Koutsos, N. Radacsi, *3D Print Med* **2020**, *6*, 8.

[66] X. Wang, M. Jiang, Z. Zhou, J. Gou, D. Hui, *Composites Part B: Engineering* **2017**, *110*, 442.

[67] U. Kalsoom, P. N. Nesterenko, B. Paull, *RSC Adv.* **2016**, *6*, 60355.

[68] J. Saroia, Y. Wang, Q. Wei, M. Lei, X. Li, Y. Guo, K. Zhang, *Int J Adv Manuf Technol* **2020**, *106*, 1695.

[69] X. Chen, W. Liu, B. Dong, J. Lee, H. O. T. Ware, H. F. Zhang, C. Sun, *Adv. Mater.* **2018**, *30*, 1705683.

[70] M. P. de Beer, H. L. van der Laan, M. A. Cole, R. J. Whelan, M. A. Burns, T. F. Scott, *Sci. Adv.* **2019**, *5*, eaau8723.

[71] G. Loke, R. Yuan, M. Rein, T. Khudiyev, Y. Jain, J. Joannopoulos, Y. Fink, *Nat Commun* **2019**, *10*, 4010.

[72] H. Lin, L. Li, J. Ren, Z. Cai, L. Qiu, Z. Yang, H. Peng, *Sci Rep* **2013**, *3*, 1353.

[73] M. A. Meitl, Y. Zhou, A. Gaur, S. Jeon, M. L. Usrey, M. S. Strano, J. A. Rogers, *Nano Lett.* **2004**, *4*, 1643.

[74] Y. Joo, J. Byun, N. Seong, J. Ha, H. Kim, S. Kim, T. Kim, H. Im, D. Kim, Y. Hong, *Nanoscale* **2015**, *7*, 6208.

[75] R. Tietze, J. Zaloga, H. Unterweger, S. Lyer, R. P. Friedrich, C. Janko, M. Pöttler, S. Dürr, C. Alexiou, *Biochemical and Biophysical Research Communications* **2015**, *468*, 463.

[76] Yongtao Yang, Yun Chen, Fan Leng, Li Huang, Zijian Wang, Weiqun Tian, *Applied Sciences* **2017**, *7*, 1215.

[77] X. Zhao, C. Zhou, Y. Lvov, M. Liu, *Small* **2019**, *15*, 1900357.

[78] J. P. Lewicki, J. N. Rodriguez, C. Zhu, M. A. Worsley, A. S. Wu, Y. Kanarska, J. D. Horn, E. B. Duoss, J. M. Ortega, W. Elmer, R. Hensleigh, R. A. Fellini, M. J. King, *Sci Rep* **2017**, *7*, 43401.

[79] S. Wu, S. Peng, C. Wang, *Polymers* **2018**, *10*, 542.

[80] B. Su, Y. Wu, L. Jiang, *Chem. Soc. Rev.* **2012**, *41*, 7832.

[81] X. Zhang, J. Xie, F. Shi, D. Lin, Y. Liu, W. Liu, A. Pei, Y. Gong, H. Wang, K. Liu, Y. Xiang, Y. Cui, *Nano Lett.* **2018**, *18*, 3829.

[82] H. Li, B. C.-K. Tee, J. J. Cha, Y. Cui, J. W. Chung, S. Y. Lee, Z. Bao, *J. Am. Chem. Soc.* **2012**, *134*, 2760.

[83] W. Liu, S. W. Lee, D. Lin, F. Shi, S. Wang, A. D. Sendek, Y. Cui, *Nat Energy* **2017**, *2*, 17035.

[84] P. C. Millett, *The Journal of Chemical Physics* **2014**, *140*, 144903.

[85] J. J. Martin, B. E. Fiore, R. M. Erb, *Nat Commun* **2015**, *6*, 8641.

[86] H. Xin, A. T. Woolley, *Nano Lett.* **2004**, *4*, 1481.

[87] K. Thorkelsson, P. Bai, T. Xu, *Nano Today* **2015**, *10*, 48.

[88] M. Grzelczak, J. Vermant, E. M. Furst, L. M. Liz-Marzán, *ACS Nano* **2010**, *4*, 3591.

[89] Q. Liu, Y. Cui, D. Gardner, X. Li, S. He, I. I. Smalyukh, *Nano Lett.* **2010**, *10*, 1347.

[90] H. Yoshida, K. Kawamoto, H. Kubo, T. Tsuda, A. Fujii, S. Kuwabata, M. Ozaki, *Adv. Mater.* **2010**, *22*, 622.

[91] Y. Yang, X. Song, X. Li, Z. Chen, C. Zhou, Q. Zhou, Y. Chen, *Adv. Mater.* **2018**, *30*, 1706539.

[92] M. A. S. R. Saadi, A. Maguire, N. T. Pottackal, M. S. H. Thakur, M. Md. Ikram, A. J. Hart, P. M. Ajayan, M. M. Rahman, *Advanced Materials* **2022**, *34*, 2108855.

[93] Y. Yang, Z. Chen, X. Song, Z. Zhang, J. Zhang, K. K. Shung, Q. Zhou, Y. Chen, *Adv. Mater.* **2017**, *29*, 1605750.

[94] R. R. Collino, T. R. Ray, R. C. Fleming, J. D. Cornell, B. G. Compton, M. R. Begley, *Extreme Mechanics Letters* **2016**, *8*, 96.

[95] T. M. Llewellyn-Jones, B. W. Drinkwater, R. S. Trask, *Smart Mater. Struct.* **2016**, *25*, 02LT01.

[96] H. Lee, B. Seong, J. Kim, Y. Jang, D. Byun, *Small* **2014**, *10*, 3918.

[97] D. Friedmann, A. F. Lee, K. Wilson, R. Jalili, R. A. Caruso, *J. Mater. Chem. A* **2019**, *7*, 10858.

[98] J. Huang, F. Kim, A. R. Tao, S. Connor, P. Yang, *Nature Mater* **2005**, *4*, 896.

[99] P. Maury, M. Escalante, D. N. Reinhoudt, J. Huskens, *Adv. Mater.* **2005**, *17*, 2718.

[100] R. Jafari, C. Cloutier, A. Allahdini, G. Momen, *Int J Adv Manuf Technol* **2019**, *103*, 1225.

[101] N. K. Mandsberg, O. Hansen, R. Taboryski, *Sci Rep* **2017**, *7*, 12794.

[102] M. Cavallaro, L. Botto, E. P. Lewandowski, M. Wang, K. J. Stebe, *Proceedings of the National Academy of Sciences* **2011**, *108*, 20923.

[103] M. Abkarian, J. Nunes, H. A. Stone, *J. Am. Chem. Soc.* **2004**, *126*, 5978.

[104] T. Yamada, Y. Hayamizu, Y. Yamamoto, Y. Yomogida, A. Izadi-Najafabadi, D. N. Futaba, K. Hata, *Nature Nanotech* **2011**, *6*, 296.

[105] H. Guo, Z. Hu, Z. Liu, J. Tian, *Adv. Funct. Mater.* **2021**, *31*, 2007810.

[106] Y. Zhang, Y. Wang, Q. Jiang, J. K. El-Demellawi, H. Kim, H. N. Alshareef, *Adv. Mater.* **2020**, *32*, 1908486.

[107] B. Xu, M. Zhu, W. Zhang, X. Zhen, Z. Pei, Q. Xue, C. Zhi, P. Shi, *Adv. Mater.* **2016**, *28*, 3333.

[108] K. Kang, K.-H. Lee, Y. Han, H. Gao, S. Xie, D. A. Muller, J. Park, *Nature* **2017**, *550*, 229.

[109] A. K. Pearce, T. R. Wilks, M. C. Arno, R. K. O’Reilly, *Nat Rev Chem* **2021**, *5*, 21.

[110] W. Tian, A. VahidMohammadi, Z. Wang, L. Ouyang, M. Beidaghi, M. M. Hamedi, *Nat Commun* **2019**, *10*, 2558.

[111] B. Elder, R. Neupane, E. Tokita, U. Ghosh, S. Hales, Y. L. Kong, *Adv. Mater.* **2020**, *32*, 1907142.

[112] D. Kokkinis, M. Schaffner, A. R. Studart, *Nat Commun* **2015**, *6*, 8643.

[113] M. Naguib, M. Kurtoglu, V. Presser, J. Lu, J. Niu, M. Heon, L. Hultman, Y. Gogotsi, M. W. Barsoum, *Adv. Mater.* **2011**, 6.

[114] K. Maleski, V. N. Mochalin, Y. Gogotsi, *Chem. Mater.* **2017**, *29*, 1632.

[115] L. Ding, Y. Wei, L. Li, T. Zhang, H. Wang, J. Xue, L.-X. Ding, S. Wang, J. Caro, Y. Gogotsi, *Nat Commun* **2018**, *9*, 155.

[116] J. R. Tumbleston, D. Shirvanyants, N. Ermoshkin, R. Janusziewicz, A. R. Johnson, D. Kelly, K. Chen, R. Pinschmidt, J. P. Rolland, A. Ermoshkin, E. T. Samulski, J. M. DeSimone, *Science* **2015**, *347*, 1349.

[117] G. F. Acosta-Vélez, T. Z. Zhu, C. S. Linsley, B. M. Wu, *International Journal of Pharmaceutics* **2018**, *546*, 145.

[118] G. Vazquez, E. Alvarez, J. M. Navaza, *J. Chem. Eng. Data* **1995**, *40*, 611.

[119] M. Á. Rodríguez-Valverde, M. Tirado Miranda, *Eur. J. Phys.* **2011**, *32*, 49.

[120] E. Shashi Menon, in *Transmission Pipeline Calculations and Simulations Manual*, Elsevier, **2015**, pp. 149–234.

[121] M. Trebbin, D. Steinhauser, J. Perlich, A. Buffet, S. V. Roth, W. Zimmermann, J. Thiele, S. Forster, *Proceedings of the National Academy of Sciences* **2013**, *110*, 6706.

[122] G. Xin, W. Zhu, Y. Deng, J. Cheng, L. T. Zhang, A. J. Chung, S. De, J. Lian, *Nature Nanotech* **2019**, *14*, 168.

[123] S. Ni, L. Isa, H. Wolf, *Soft Matter* **2018**, *14*, 2978.

[124] B. Sun, H. Sirringhaus, *J. Am. Chem. Soc.* **2006**, *128*, 16231.

[125] C. Hanske, M. B. Müller, V. Bieber, M. Tebbe, S. Jessl, A. Wittemann, A. Fery, *Langmuir* **2012**, *28*, 16745.

[126] S. Naficy, R. Jalili, S. H. Aboutalebi, R. A. Gorkin III, K. Konstantinov, P. C. Innis, G. M. Spinks, P. Poulin, G. G. Wallace, *Mater. Horiz.* **2014**, *1*, 326.

[127] B. Akuzum, K. Maleski, B. Anasori, P. Lelyukh, N. J. Alvarez, E. C. Kumbur, Y. Gogotsi, *ACS Nano* **2018**, *12*, 2685.

[128] Q. Li, Y. Gou, T.-G. Wang, T. Gu, Q. Yu, L. Wang, *Coatings* **2019**, *9*, 500.

[129] M. Sebastiani, E. Rossi, M. Zeeshan Mughal, A. Benedetto, P. Jacquet, E. Salvati, A. M. Korsunsky, *Nanomaterials* **2020**, *10*, 853.

[130] V. Timoshevskii, Y. Ke, H. Guo, D. Gall, *Journal of Applied Physics* **2008**, *103*, 113705.

[131] L. Du, D. Maroudas, *Appl. Phys. Lett.* **2017**, *110*, 103103.

[132] Y. Tao, F. Kong, Z. Li, J. Zhang, X. Zhao, Q. Yin, D. Xing, P. Li, *Journal of Materials Research and Technology* **2021**, *15*, 4860.

[133] S. Mora, N. M. Pugno, D. Misseroni, *Materials Today* **2022**, *59*, 107.

[134] M. Ziaee, N. B. Crane, *Additive Manufacturing* **2019**, *28*, 781.

[135] M. Lalegani Dezaki, A. Serjouei, A. Zolfagharian, M. Fotouhi, M. Moradi, M. K. A. Ariffin, M. Bodaghi, *Advanced Powder Materials* **2022**, *1*, 100054.

[136] B. Dermeik, N. Travitzky, *Adv. Eng. Mater.* **2020**, *22*, 2000256.

[137] H. Guo, J. Xu, S. Zhang, G. Yi, *Applied Sciences* **2020**, *11*, 304.

[138] S. Wickramasinghe, T. Do, P. Tran, *Polymers* **2020**, *12*, 1529.

[139] S. Miao, M. Nowicki, H. Cui, S.-J. Lee, X. Zhou, D. K. Mills, L. G. Zhang, *Biofabrication* **2019**, *11*, 035030.

[140] D. Baranov, A. Fiore, M. van Huis, C. Giannini, A. Falqui, U. Lafont, H. Zandbergen, M. Zanella, R. Cingolani, L. Manna, *Nano Lett.* **2010**, *10*, 743.

[141] M. Grzelczak, J. Vermant, E. M. Furst, L. M. Liz-Marzán, *ACS Nano* **2010**, *4*, 3591.

[142] A. Olanrewaju, M. Beaugrand, M. Yafia, D. Juncker, *Lab Chip* **2018**, *18*, 2323.

[143] N. Bhattacharjee, A. Urrios, S. Kang, A. Folch, *Lab Chip* **2016**, *16*, 1720.

[144] H.-N. Barad, H. Kwon, M. Alarcón-Correa, P. Fischer, *ACS Nano* **2021**, *15*, 5861.

[145] D. Lebedev, G. Malyshev, I. Ryzhkov, A. Mozharov, K. Shugurov, V. Sharov, M. Panov, I. Tumkin, P. Afonicheva, A. Evstrapov, A. Bukatin, I. Mukhin, *Microfluid Nanofluid* **2021**, *25*, 51.

[146] L. Jiang, N. S. Korivi, in *Nanolithography*, Elsevier, **2014**, pp. 424–443.

[147] D. J. Guckenberger, T. E. de Groot, A. M. D. Wan, D. J. Beebe, E. W. K. Young, *Lab Chip* **2015**, *15*, 2364.

[148] K. Sugioka, J. Xu, D. Wu, Y. Hanada, Z. Wang, Y. Cheng, K. Midorikawa, *Lab Chip* **2014**, *14*, 3447.

[149] W. Xu, S. Jambhulkar, D. Ravichandran, Y. Zhu, M. Kakarla, Q. Nian, B. Azeredo, X. Chen, K. Jin, B. Vernon, D. G. Lott, J. L. Cornella, O. Shefi, G. Miquelard-Garnier, Y. Yang, K. Song, *Small* **2021**, *17*, 2100817.

[150] D. Ravichandran, W. Xu, S. Jambhulkar, Y. Zhu, M. Kakarla, M. Bawareth, K. Song, *ACS Appl. Mater. Interfaces* **2021**, *13*, 52274.

[151] S. Jambhulkar, W. Xu, D. Ravichandran, J. Prakash, A. N. Mada Kannan, K. Song, *Nano Lett.* **2020**, *20*, 3199.

[152] L. Lu, P. Guo, Y. Pan, *Journal of Manufacturing Science and Engineering* **2017**, *139*, 071008.

[153] T. Brezesinski, M. Groenewolt, A. Gibaud, N. Pinna, M. Antonietti, B. Smarsly, *Adv. Mater.* **2006**, *18*, 2260.

[154] P. Zhu, T. Kong, C. Zhou, L. Lei, L. Wang, *Small Methods* **2018**, *2*, 1800017.

[155] D. Rahmatabadi, A. Aminzadeh, M. Aberoumand, M. Moradi, in *Fused Deposition Modeling Based 3D Printing* (Eds.: H. K. Dave, J. P. Davim), Springer International Publishing, Cham, **2021**, pp. 131–150.

[156] H. Gonabadi, A. Yadav, S. J. Bull, *Int J Adv Manuf Technol* **2020**, *111*, 695.

[157] H. Kim, K.-H. Ryu, D. Baek, T. A. Khan, H.-J. Kim, S. Shin, J. Hyun, J. S. Ahn, S.-J. Ahn, H. J. Kim, J. Koo, *ACS Appl. Mater. Interfaces* **2020**, *12*, 23453.

[158] J. Wu, *IOP Conf. Ser.: Mater. Sci. Eng.* **2018**, *392*, 062050.

[159] X. Meng, Y. Sun, M. Yu, Z. Wang, J. Qiu, *Small Science* **2021**, *1*, 2100021.

[160] S. Abdolhosseinzadeh, J. Heier, C. (John) Zhang, *J. Phys. Energy* **2020**, *2*, 031004.

[161] H. Zargartalebi, S. H. Hejazi, A. Sanati-Nezhad, *Nat Commun* **2022**, *13*, 3085.

[162] K. Kato, F. Dang, K. Mimura, Y. Kinemuchi, H. Imai, S. Wada, M. Osada, H. Haneda, M. Kuwabara, *Advanced Powder Technology* **2014**, *25*, 1401.

[163] D. Luo, C. Yan, T. Wang, *Small* **2015**, *11*, 5984.

[164] B. Bharti, A.-L. Fameau, M. Rubinstein, O. D. Velev, *Nature Mater* **2015**, *14*, 1104.

[165] M. R. Jones, K. D. Osberg, R. J. Macfarlane, M. R. Langille, C. A. Mirkin, *Chem. Rev.* **2011**, *111*, 3736.

[166] Y. Choi, Y. Song, Y. T. Kim, S. J. Lee, K. G. Lee, S. G. Im, *ACS Appl. Mater. Interfaces* **2021**, *13*, 3098.

[167] Y. Kim, T. Kim, J. Lee, Y. S. Choi, J. Moon, S. Y. Park, T. H. Lee, H. K. Park, S. A. Lee, M. S. Kwon, H. Byun, J. Lee, M. Lee, B. H. Hong, H. W. Jang, *Adv. Mater.* **2021**, *33*, 2004827.

[168] I. Topolniak, A. M. Elert, X. Knigge, G. C. Ciftci, J. Radnik, H. Sturm, *Advanced Materials* **2022**, *34*, 2109509.

[169] P. Li, X. Dou, H. Schönherr, *Polym. Int.* **2019**, *68*, 1015.

[170] G. G. Yang, H. J. Choi, K. H. Han, J. H. Kim, C. W. Lee, E. I. Jung, H. M. Jin, S. O. Kim, *ACS Appl. Mater. Interfaces* **2022**, *14*, 12011.

[171] W. Jung, S. Jang, S. Cho, H. Jeon, H. Jung, *Adv. Mater.* **2020**, *32*, 1907101.

[172] J. A. Rogers, H. H. Lee, *Unconventional Nanopatterning Techniques and Applications*, John Wiley & Sons, Inc., Hoboken, NJ, USA, **2008**.

[173] H. Puliyalil, U. Cvelbar, *Nanomaterials* **2016**, *6*, 108.

[174] L. Zhang, Y. Liu, Z. Li, W. Wang, *Micromachines* **2018**, *9*, 162.

[175] D. Kwak, J. A. Lim, B. Kang, W. H. Lee, K. Cho, *Adv. Funct. Mater.* **2013**, *23*, 5224.

[176] B.-J. de Gans, S. Hoeppener, U. S. Schubert, *Adv. Mater.* **2006**, *18*, 910.

[177] B. Bao, J. Jiang, F. Li, P. Zhang, S. Chen, Q. Yang, S. Wang, B. Su, L. Jiang, Y. Song, *Adv. Funct. Mater.* **2015**, *25*, 3286.

[178] S. Jambhulkar, W. Xu, R. Franklin, D. Ravichandran, Y. Zhu, K. Song, *J. Mater. Chem. C* **2020**, *8*, 9495.

[179] D. Ahn, L. M. Stevens, K. Zhou, Z. A. Page, *ACS Cent. Sci.* **2020**, *6*, 1555.

[180] B. E. Kelly, I. Bhattacharya, H. Heidari, M. Shusteff, C. M. Spadaccini, H. K. Taylor, *Science* **2019**, *363*, 1075.

[181] S. Coelho, J. Baek, J. Walsh, J. Justin Gooding, K. Gaus, *Nat Commun* **2022**, *13*, 647.

[182] A. Reiser, M. Lindén, P. Rohner, A. Marchand, H. Galinski, A. S. Sologubenko, J. M. Wheeler, R. Zenobi, D. Poulikakos, R. Spolenak, *Nat Commun* **2019**, *10*, 1853.

[183] J.-U. Park, M. Hardy, S. J. Kang, K. Barton, K. Adair, D. kishore Mukhopadhyay, C. Y. Lee, M. S. Strano, A. G. Alleyne, J. G. Georgiadis, P. M. Ferreira, J. A. Rogers, *Nature Mater* **2007**, *6*, 782.

[184] W. Jung, Y.-H. Jung, P. V. Pikhitsa, J. Feng, Y. Yang, M. Kim, H.-Y. Tsai, T. Tanaka, J. Shin, K.-Y. Kim, H. Choi, J. Rho, M. Choi, *Nature* **2021**, *592*, 54.

[185] W. Su, B. S. Cook, Y. Fang, M. M. Tentzeris, *Sci Rep* **2016**, *6*, 35111.

[186] W. Xu, S. Jambhulkar, Y. Zhu, D. Ravichandran, M. Kakarla, B. Vernon, D. G. Lott, J. L. Cornella, O. Shefi, G. Miquelard-Garnier, Y. Yang, K. Song, *Composites Part B: Engineering* **2021**, *223*, 109102.

[187] W. Xu, S. Jambhulkar, D. Ravichandran, Y. Zhu, M. Kakarla, Q. Nian, B. Azeredo, X. Chen, K. Jin, B. Vernon, D. G. Lott, J. L. Cornella, O. Shefi, G. Miquelard-Garnier, Y. Yang, K. Song, *Small* **2021**, *17*, 2100817.

[188] B. Elder, R. Neupane, E. Tokita, U. Ghosh, S. Hales, Y. L. Kong, *Adv. Mater.* **2020**, *32*, 1907142.

[189] D. Ravichandran, W. Xu, M. Kakarla, S. Jambhulkar, Y. Zhu, K. Song, *Additive Manufacturing* **2021**, *47*, 102322.

[190] W. Xu, D. Ravichandran, S. Jambhulkar, Y. Zhu, K. Song, *Adv. Funct. Mater.* **2021**, *31*, 2009311.

[191] W. Xu, R. Franklin, D. Ravichandran, M. Bawareth, S. Jambhulkar, Y. Zhu, M. Kakarla, F. Ejaz, B. Kwon, M. K. Hassan, M. Al-Ejji, A. Asadi, N. Chawla, K. Song, *Adv Funct Materials* **2022**, 2204731.

[192] D. Ravichandran, W. Xu, M. Kakarla, S. Jambhulkar, Y. Zhu, K. Song, *Additive Manufacturing* **2021**, *47*, 102322.

[193] M. G. Rasul, M. Cheng, Y. Jiang, Y. Pan, R. Shahbazian-Yassar, *ACS Nanosci. Au* **2022**, *2*, 297.

[194] K. Grundke, S. Michel, M. Osterhold, *Progress in Organic Coatings* **2000**, *39*, 101.

[195] I. C. Bellettini, R. Eising, A. C. Felippe, J. B. Domingos, E. Minatti, V. G. Machado, *Química Nova* **2015**, DOI 10.5935/0100-4042.20150085.

[196] J. Penfold, I. Tucker, R. K. Thomas, D. J. F. Taylor, J. Zhang, X. L. Zhang, *Langmuir* **2007**, *23*, 3690.

[197] M. Y. Lee, J. H. Lee, J. W. Chung, S.-Y. Kwak, *Journal of Environmental Management* **2018**, *206*, 740.

[198] N. Uzal, N. Ates, S. Saki, Y. E. Bulbul, Y. Chen, *Separation and Purification Technology* **2017**, *187*, 118.

[199] T. Wang, G. Zhang, B. Zhang, S. Liu, D. Li, C. Liu, *ACS Appl. Nano Mater.* **2021**, *4*, 4153.

[200] J. Han, G. Du, W. Gao, H. Bai, *Adv. Funct. Mater.* **2019**, *29*, 1900412.

[201] *Encapsulation Technologies for Electronic Applications*, Elsevier, **2019**.

[202] B. A. Miller-Chou, J. L. Koenig, *Progress in Polymer Science* **2003**, *28*, 1223.

[203] M. Schaffner, P. A. Rühs, F. Coulter, S. Kilcher, A. R. Studart, *Sci. Adv.* **2017**, *3*, eaao6804.

[204] S. Zhao, G. Siqueira, S. Drdova, D. Norris, C. Ubert, A. Bonnin, S. Galmarini, M. Ganobjak, Z. Pan, S. Brunner, G. Nyström, J. Wang, M. M. Koebel, W. J. Malfait, *Nature* **2020**, *584*, 387.

[205] M. Cheng, A. Ramasubramanian, M. G. Rasul, Y. Jiang, Y. Yuan, T. Foroozan, R. Deivanayagam, M. Tamadoni Saray, R. Rojaee, B. Song, V. R. Yurkiv, Y. Pan, F. Mashayek, R. Shahbazian-Yassar, *Adv. Funct. Mater.* **2021**, *31*, 2006683.

[206] K. Shen, J. Ding, S. Yang, *Adv. Energy Mater.* **2018**, *8*, 1800408.

[207] O. D. Yirmibesoglu, L. E. Simonsen, R. Manson, J. Davidson, K. Healy, Y. Menguc, T. Wallin, *Commun Mater* **2021**, *2*, 82.

[208] H. Yuk, B. Lu, S. Lin, K. Qu, J. Xu, J. Luo, X. Zhao, *Nat Commun* **2020**, *11*, 1604.

[209] J.-F. Agassant, Y. Demay, *Polymers* **2022**, *14*, 1309.

[210] B. Lu, H. Zhang, A. Maazouz, K. Lamnawar, *Polymers* **2021**, *13*, 417.

[211] A. Cortés, A. Cosola, M. Sangermano, M. Campo, S. González Prolongo, C. F. Pirri, A. Jiménez-Suárez, A. Chiappone, *Adv. Funct. Mater.* **2021**, *31*, 2106774.

[212] V. Guerra, C. Wan, V. Degirmenci, J. Sloan, D. Presvytis, T. McNally, *Nanoscale* **2018**, *10*, 19469.

[213] Z. Lin, Y. Liu, S. Raghavan, K. Moon, S. K. Sitaraman, C. Wong, *ACS Appl. Mater. Interfaces* **2013**, *5*, 7633.

[214] G. Han, D. Zhang, C. Kong, B. Zhou, Y. Shi, Y. Feng, C. Liu, D.-Y. Wang, *Chemical Engineering Journal* **2022**, *437*, 135482.

[215] B. Zhong, J. Zou, L. An, C. Ji, X. Huang, W. Liu, Y. Yu, H. Wang, G. Wen, K. Zhao, X. Lin, *Composites Part A: Applied Science and Manufacturing* **2019**, *127*, 105629.

[216] M.-X. Du, Y.-F. Yuan, J.-M. Zhang, C.-Y. Liu, *Macromolecules* **2022**, *55*, 4578.

[217] T. C. Chan, H. T. Li, K. Y. Li, *J. Phys. Chem. B* **2015**, *119*, 15718.

[218] T. P. Gall, R. C. Lasky, E. J. Kramer, *Polymer* **1990**, *31*, 1491.

[219] C. F. Jasso-Gastinel, in *Modification of Polymer Properties*, Elsevier, **2017**, pp. 185–210.

[220] L. Baij, J. J. Hermans, K. Keune, P. D. Iedema, *Macromolecules* **2018**, *51*, 7134.

[221] J. R. Harter, T. S. Palmer, P. A. Greaney, in *Advances in Heat Transfer*, Elsevier, **2020**, pp. 335–488.

[222] S. M. Sohel Murshed, C. A. Nieto de Castro, *Renewable and Sustainable Energy Reviews* **2017**, *78*, 821.

[223] V. G. Pastukhov, Yu. F. Maidanik, C. V. Vershinin, M. A. Korukov, *Applied Thermal Engineering* **2003**, *23*, 1125.

APPENDIX A

SUPPORTING INFORMATION FOR CHAPTER 2

Figure 34. Contact angle measurement from the shape of the THF droplet wrt (a) glass (b) 3D printed substrate with gratings (c) resin film (contact angle measurements of substrate were performed using the Rame-hart automatic goniometer).

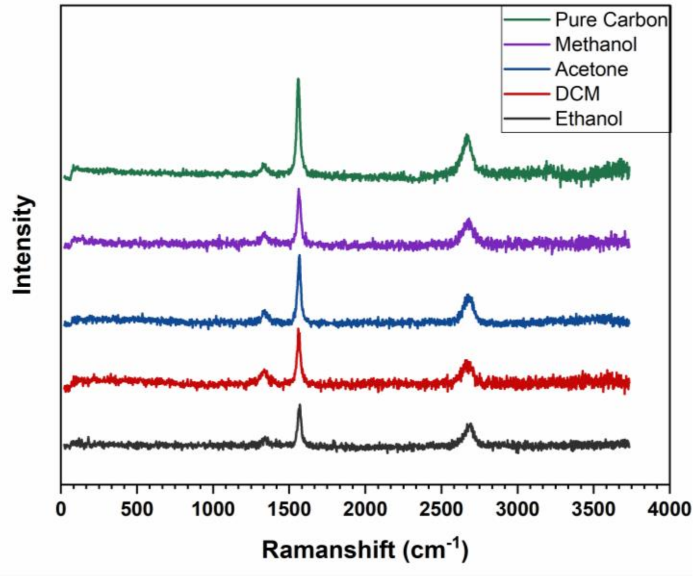

Figure 35. Raman spectra of pure CNF and CNF after immersed in VOC. For Raman measurements, confocal Raman equipment (alpha500 RA, WITec) with a laser frequency of 532 nm (second harmonic generation) was used. An area scan with an integration time of 1 s with 50 points per line and 50 lines per image were taken with a measurement time of 39 min in total. The laser beam was directly focused on the sample surface using a 20/0.4 Zeiss objective.

APPENDIX B

SUPPORTING INFORMATION FOR CHAPTER 3

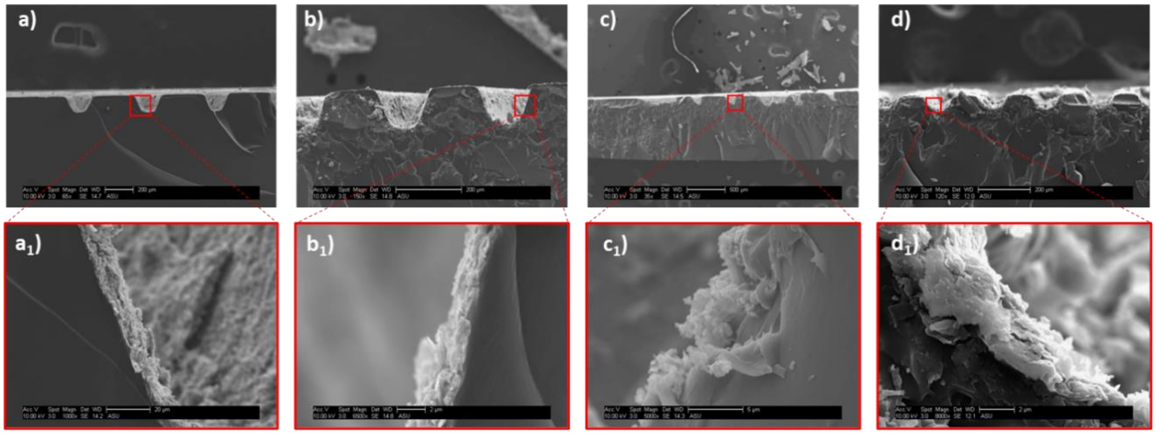

Figure 36. SEM images of the cross-section of the complex substrate after coating with 10 mg/ml <15> showing a thin film of MXene deposited at intricate channels shapes a) wavy grooves, b) antenna-shaped circles, c) cross-linked triangle channels, and d) interdigitated structure. The zoomed-in images (a_1-d_1) showing layer-by-layer deposition of MXene flakes.

APPENDIX C

SUPPORTING INFORMATION FOR CHAPTER 4

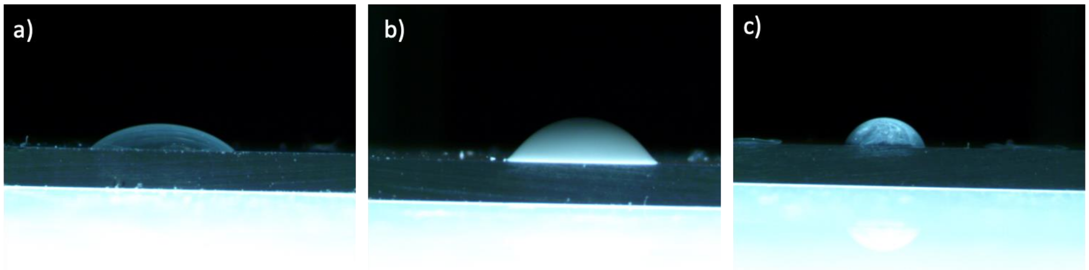

Figure 37. Contact angle measurements for printing materials of a) PEG, b) E-BN25, and c) PEI ($\theta_{PEG\text{-}glass}$= 35.89°, $\theta_{E\text{-}BN25\text{-}glass}$=44.17°, $\theta_{PEI\text{-}glass}$=63.43°) on glass substrates

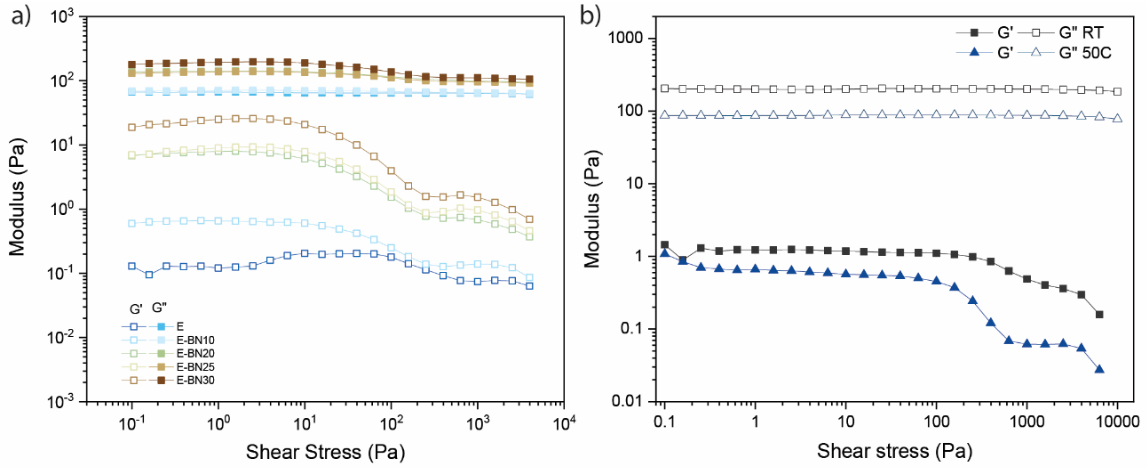

Figure 38. Storage modulus (G') and loss modulus (G'') as a function of shear stress for a) E-BN inks at a varying concentration of BNs and b) PEI at room temperature (RT) and 50°C

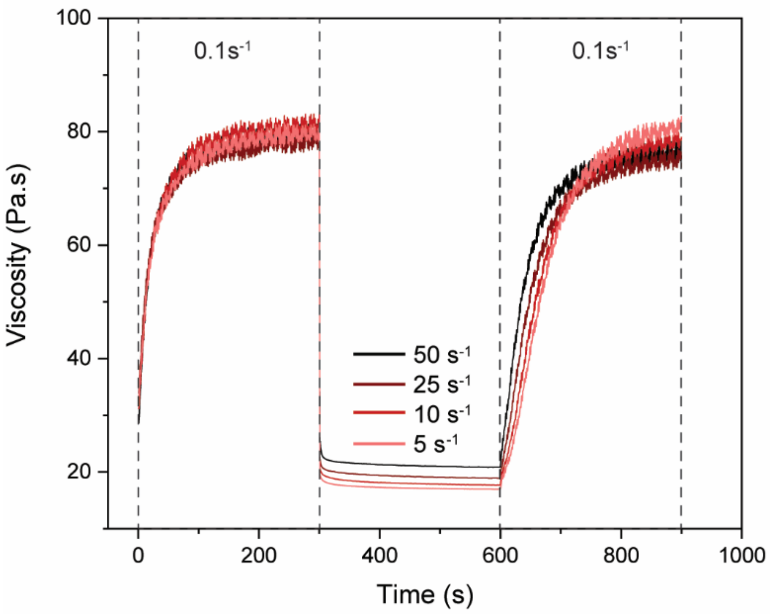

Figure 39. Thixotropic properties of E-BN25 ink, simulating the printing condition with alternating high and low shear rates

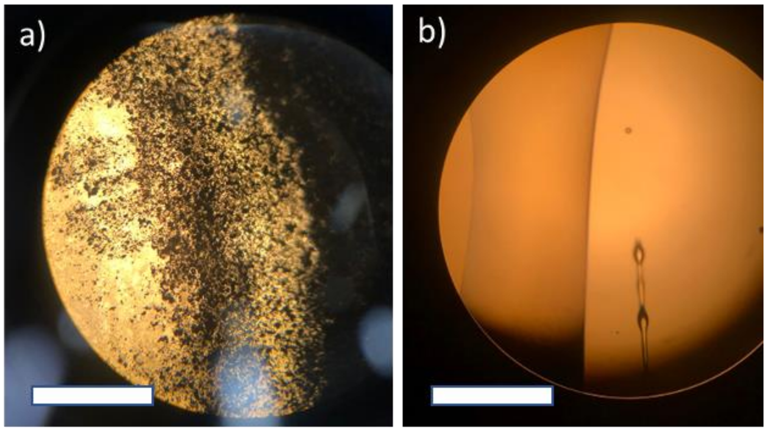

Figure 40. The optical image showing the interfacial phenomena at the polymer/polymer interface between a) E/PEG30-H (diffusion) and b) E/PEI (no diffusion) (scale bars 500 μm)

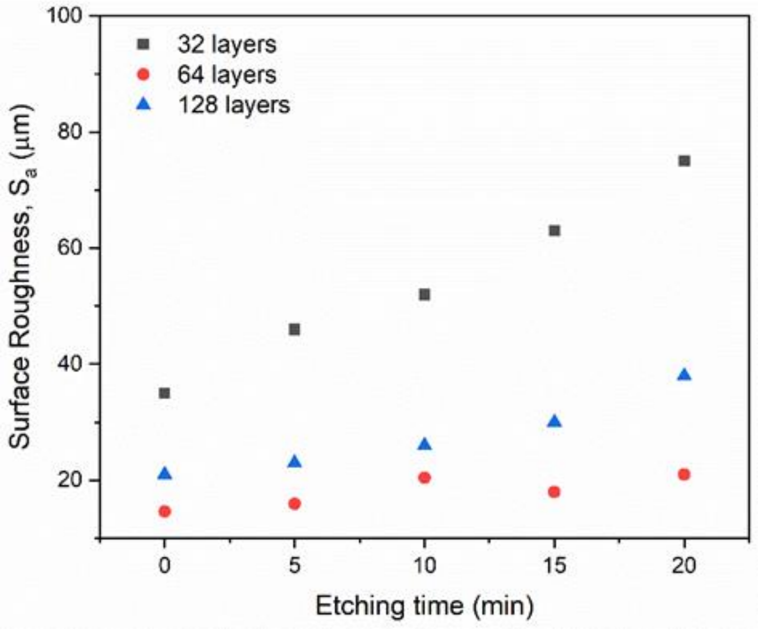

Figure 41. The average surface roughness (S_a) of the MDIW micropatterns was measured using an optical profilometer after etching in IPA (RT) as a function of etching periods (min)

APPENDIX D

SUPPORTING INFORMATION FOR CHAPTER 5

Table 4. The approximate values of capillary force (Fc) and Reynold's number (Re) of MXene ink within microchannels of different LH

LH	**F_c (N)**	**Re_{ink}**
50	$0.49*10^{-6}$	0.0078
100	$1.14*10^{-6}$	0.016
150	$1.71*10^{-6}$	0.023
180	$2.55*10^{-6}$	0.027

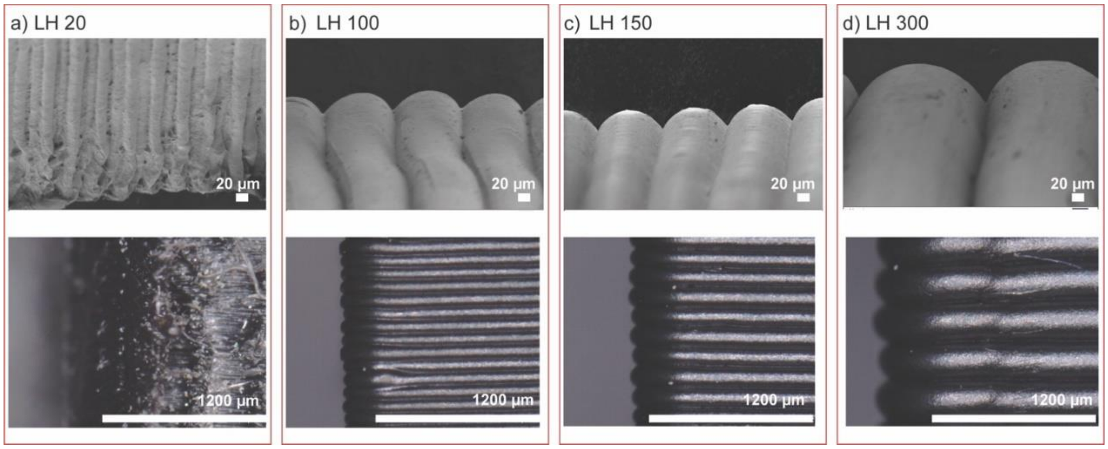

Figure 42. SEM and optical images of a cross-sectional view of 3D printed templates demonstrating stairstep topology for a) LH 20 μm, b) LH 100 μm, c) LH 150 μm, d) LH 300 μm

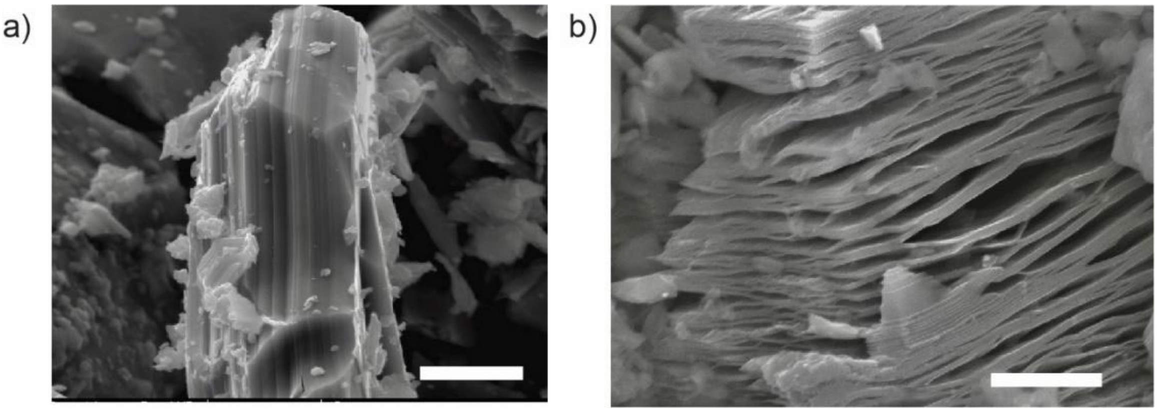

Figure 43. a) Ti_3AlC_2 MAX particle morphology with the characteristic layered structure (Scale bar 2 µm), b) MXene particles after etching show accordion structure (Scale bar 1 µm)

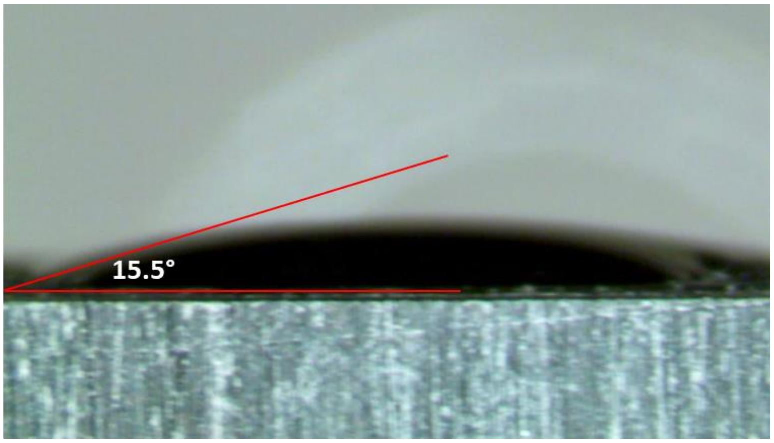

Figure 44. The measured static contact angle between ethanol and flat ABS surface

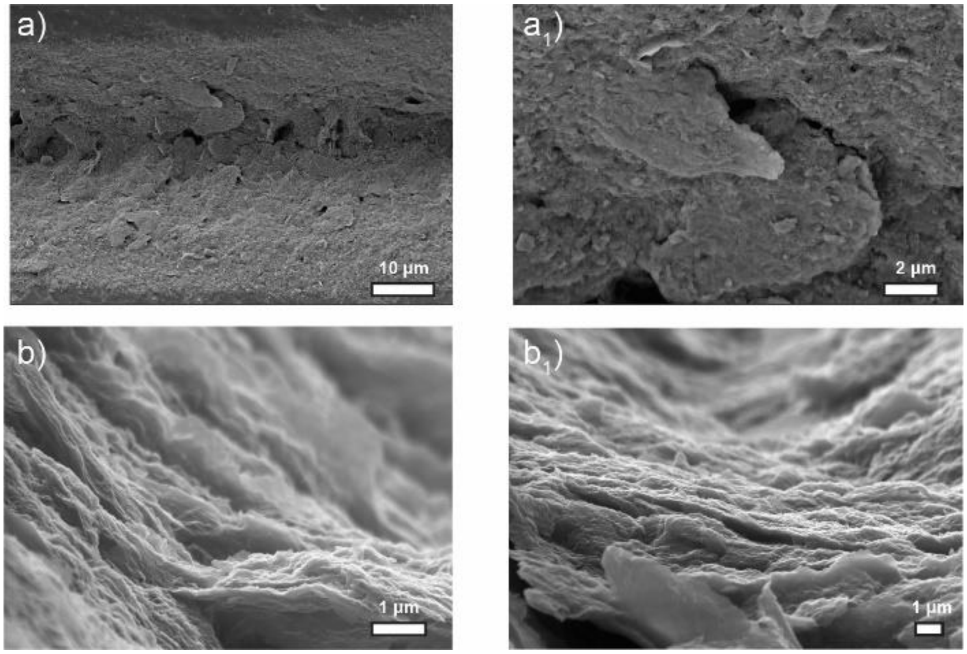

Figure 45. SEM images of the a) top view of the patterned MXene film at microchannel with continuous morphology and b) parallelly stacked MXene flakes for 5 mg/ml #5

APPENDIX E

STATEMENT OF COAUTHORS' PERMISSIONS

I, Sayli Jambhulkar, committed that all co-authors have granted their permissions for the usage of following publications in this dissertation:

Chapter 2

(1) Jambhulkar, S.; Xu, W.; Ravichandran, D.; Prakash, J.; Mada Kannan, A. N.; Song, K. Scalable Alignment and Selective Deposition of Nanoparticles for Multifunctional Sensor Applications. *Nano Lett.* 2020, *20* (5), 3199–3206. https://doi.org/10.1021/acs.nanolett.9b05245.

Chapter 3

(2) Jambhulkar, S.; Liu, S.; Vala, P.; Xu, W.; Ravichandran, D.; Zhu, Y.; Bi, K.; Nian, Q.; Chen, X.; Song, K. Aligned $Ti_3C_2T_x$ MXene for 3D Micropatterning *via* Additive Manufacturing. *ACS Nano* 2021, *15* (7), 12057–12068. https://doi.org/10.1021/acsnano.1c03388.

Chapter 4

(3) Jambhulkar, S.; Ravichadran, D.; Sundaravadivelan, B.; Song, K. A Hybrid 3D Printing for Highly-Efficient Nanoparticle Micropatterning. *J. Mater. Chem. C* 2023. https://doi.org/10.1039/D3TC00168G

Chapter 5

(4) Jambhulkar, S.; Ravichandran, D.; Thippanna, V.; Patil, D.; Song, K. A Multi-Material 3D Printing-Assisted Micropatterning. 2023. Submitted.